

Unraveling subsurface crustal dynamics: exploring electrical and seismic refraction methods from theories to existing and machine learning-based emerging prospects

Adedibu Sunny Akingboye ^{a, b}

^a Department of Earth Sciences, Adekunle Ajasin University, 001 Akungba-Akoko, Ondo State, Nigeria

^b Helmholtz Centre Potsdam – GFZ German Research Centre for Geosciences, 14473 Telegrafenberg, Potsdam, Brandenburg, Germany

ARTICLE INFO

Keywords:

Electrical resistivity tomography (ERT)
Induced polarization (IP)
Self-potential (SP) method
Seismic refraction tomography (SRT)
Machine learning
Surface–subsurface crustal modeling

ABSTRACT

This comprehensive review explores electrical and seismic refraction methods, including their emerging techniques, namely electrical resistivity tomography (ERT) and seismic refraction tomography (SRT). It discusses their crucial roles in understanding surface–subsurface crustal dynamics, outlining their principles, strengths, and limitations. Additionally, it provides insights into the induced polarization method and briefly discusses the self-potential method. The review thoroughly examines the mapping of surface–subsurface resistivity and velocity structures, crucial for comprehending Earth's surface, deep crustal, and hazard processes. Despite the numerous benefits of these techniques, challenges persist, necessitating multidisciplinary approaches due to lithology heterogeneities, geological process nuances, and geophysical data uncertainties. Hence, the emergence of machine learning and deep learning in ERT and SRT significantly enhances their accuracy in inversion modeling and geological feature identification. This integration of domain-specific knowledge with data- and image-driven approaches effectively addresses subsurface characterization challenges. Case studies utilizing real-time field electrical and seismic P-wave velocity datasets illustrate concepts, accompanied by the development of new methodological frameworks and analytical modeling. These frameworks provide systematic data modeling, facilitating velocity–resistivity relationships for enhanced geological characterization. This evidence underscores the importance of leveraging state-of-the-art techniques to obtain a broader range of parameters for subsurface structure delineation, environmental risk assessment, and informed decision-making. Ongoing research innovation is anticipated to continue improving capabilities in subsurface geophysical exploration.

1. Introduction

Exploring the intricate dynamics of surface–subsurface crustal formations has long been a foundation of geoscience research, driving the development of innovative methodologies aimed at uncovering the hidden complexities beneath the Earth's surface (Ronczka et al. 2018; Abdullah et al. 2022; Akingboye and Bery 2023a; Gao et al. 2024; Sujitapan et al. 2024; Akingboye 2024). Direct and indirect geophysical methods are significant in exploring crustal dynamics by employing physics principles to understand the arrangement, constituents, and characteristics of the subsurface (Wong 1995; Meju et al. 2003; Loke et al. 2022; Husainy et al. 2023; Akingboye 2023; Akingboye and Bery 2023b). This often requires examination and analysis of various geophysical, geological, and geochemical data, as well as inversion models. Among the thriving geophysical methods used, electrical and seismic refraction methods have emerged as pivotal tools, offering unparalleled insights into subsurface structures, properties, and processes for many subsurface investigations, such as groundwater, mineral exploration, geotechnical, geoengineering, archaeology, and agrogeophysics (agricultural practices), among others (Cheng et al. 2019; Schoole et al. 2020; Bièvre et al. 2021; Zakaria et al. 2022; Akingboye and Bery 2023a; Sujitapan et al. 2024). The comprehensive insights into understanding crustal formations and their dynamics, the theoretical foundations, methodological advancements, and emerging prospects of electrical and seismic refraction techniques are crucial, with an

overview of induced polarization (IP) and self-potential (SP) methods. The fundamental principles underlying these methods draw upon established theories in geophysics, signal processing, and rock physics to provide a nuanced understanding of the physical phenomena at play (Loke 2002; Binley and Kemna 2005; Binley 2015; Revil et al. 2022).

The emergence of improved techniques for electrical resistivity and seismic refraction methods has greatly redefined the speed and accuracy of unraveling crustal features. As a result, electrical resistivity tomography (ERT) and seismic refraction tomography (SRT) are the two improved versions of these methods and are the most commonly used (Loke 2002; Zeng et al. 2018; Loke et al. 2022). ERT is a very versatile technique in subsurface exploration, harnessing the spatial distribution of electrical resistivity to delineate geological structures and characterize subsurface properties. The theoretical framework of ERT explores the relationship between resistivity and lithology, and the influence of pore fluid conductivity, as the framework governing data acquisition, processing, and interpretation (Marquis and Hyndman 1992; Meju et al. 2003; Akingboye and Bery 2023a; Akingboye et al. 2023). The technique can be well augmented by IP by probing the polarizability of subsurface materials. By analyzing the time- and frequency-dependent behaviors of IP effects, researchers can glean valuable insights into mineralogical composition, porosity, and fluid content, thereby enhancing the resolution and accuracy of subsurface imaging (Kemna et al. 2004; Binley and Kemna 2005; Akingboye and Bery

Exploring electrical and seismic refraction methods: theories to emerging prospects

2021a). In tandem with electrical methods, SRT represents a powerful tool for subsurface exploration, capitalizing on variations in seismic wave velocity to delineate geological boundaries, subsurface structures, and air- and water-filled cavities, among others (Dahlin and Wisén 2018; Ronczka et al. 2018; Sujitapan et al. 2024). The theoretical underpinning of SRT is based on wave propagation, travel time analysis, and the interpretation of seismic velocity models. ERT offers a means to address the constraints associated with SRT models. Similarly, combining IP and/or SP (though less common) with these methods is advantageous, as IP identifies clay through high chargeability and water through low chargeability (Slater and Glaser 2003), while SP can efficiently resolve subsurface electrochemical reactions (Mao et al. 2015; Biswas and Sharma 2017; Hasan and Shang 2023).

Unraveling the characteristics of surface–subsurface crustal layers involves assessing the geological and physical attributes of the Earth's subsurface. Achieving accurate predictions tailored to specific geological features requires the use of various inversion models for resistivity and seismic refraction. These models often substitute rock attributes like porosity, mineral composition, and fracture density (Akingboye and Ogunyele 2019; Bièvre et al. 2021; Akingboye and Bery 2022a). Understanding these physical features depends on dealing with a mix of geological factors. This can be tricky when merging different geophysical datasets that cover various related and unrelated processes, accounting for complexities in modeling geological factors (Gallardo and Meju 2003, 2007). Since subsurface targets are 3-D in nature, 3-D resistivity and seismic refraction surveys and their interpretation models are the best methods to provide more accurate results for resolving complex subsurface structures (Chambers et al. 2006; Zhang et al. 2021; Hasan et al. 2023). It is, therefore, important to choose the right survey, inversion, and interpretation techniques to improve the signal-to-noise ratio and the geological conditions. Implementing this approach enhances the efficiency of project planning by reducing the time it takes to complete tasks, minimizing expenses, and optimizing total production outcomes. Furthermore, the integration of machine learning (ML) and deep learning techniques into ERT and SRT data analysis heralds a new era of automation and intelligence in subsurface imaging (Liu et al. 2020, 2021). By harnessing the computational power of artificial intelligence, researchers can streamline data processing, enhance inversion algorithms, and extract valuable insights from complex geophysical datasets.

With increasing complexity in resistivity and seismic exploration, accurately estimating geophysical responses and related geological parameters becomes more demanding. Advancements in ML and deep learning algorithms have revolutionized ERT and SRT inversion models (Yang and Ma 2019; Liu et al. 2020; Côte et al. 2020). Supervised and unsupervised ML and deep learning algorithms such as Artificial Neural Networks (ANNs), Convolutional Neural Networks (CNNs), Monte Carlo, Random Forest, Generative Adversarial Networks (GANs), and Bayesian models have become transformative tools in ERT and SRT analysis and are promising in interpreting complex geological structures

(Oware et al. 2019; Aleardi et al. 2021; Liu et al. 2023b). These advanced algorithms uncover hidden patterns in large and complex datasets, enhancing the interpretation of surface–subsurface geological features in large-scale datasets within a reasonable timeframe. They prove effective in studying various Earth surface, deep crustal, and hazard processes, including landslides, subsurface dissolution, hydrogeologic structures, and soil-rock differentiation (Guevara et al. 2017; Dimech et al. 2022; Akingboye and Bery 2023a). In addition, significant efforts have been directed toward subsurface characterization across various geological terrains, aiming to establish relationships between seismic velocity and electrical resistivity. Supervised statistical (regression) and unsupervised ML, especially K-means clustering, have been employed for joint parameter inversion of ERT and SRT models (Muñoz et al. 2010; Zeng et al. 2018; Delforge et al. 2021; Akingboye and Bery 2023a). These empirical relationships have enhanced our understanding of resistivity and velocity, offering broader applicability across various geological settings.

In this review, intriguing case studies from diverse geological settings are presented, showcasing the practical applications and efficacy of electrical and seismic refraction methods in real-world scenarios. These case studies serve as exemplars of the versatility and reliability of ERT and SRT in applications ranging from electrode array performance to the development of new interpretation modeling approaches in groundwater, environmental assessment, and engineering studies. To justify the purpose of this study and bridge the research gap in the emerging trends and prospects of velocity–resistivity relationships, a giant leap to previous research dated decades and the most recent ones were gathered and reviewed. In summary, as illustrated in Fig. 1, this review serves as a comprehensive compendium of knowledge, providing researchers, practitioners, and students with a thorough understanding of the principles, methodologies, and applications of electrical and seismic refraction methods, including their integration with ML and deep learning in inversion and interpretation modeling. By synthesizing theoretical insights, practical experience, and cutting-edge developments, this offers readers a holistic perspective on these essential techniques for surface–subsurface crustal exploration and characterization.

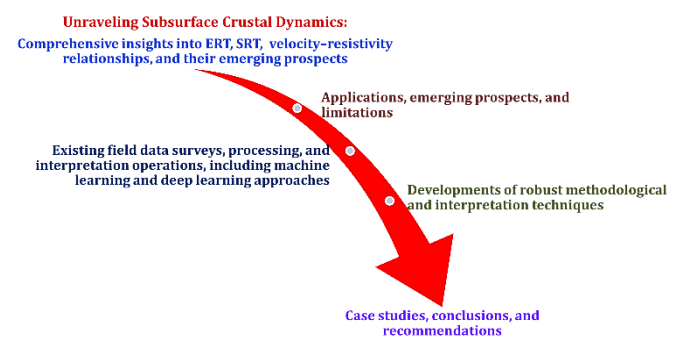


Fig. 1. Research review synopsis, outlining the detailed stages involved in the comprehensive review.

2. Insights into electrical methods in earth crustal prospecting

2.1 Electrical resistivity method

The electrical methods, including self-potential (SP), induced polarization (IP), and electrical resistivity methods, utilize either naturally occurring or artificially generated fields/currents to holistically characterize surface–subsurface lithologic units (Telford et al. 1990; Binley 2015; Akingboye and Ogunyele 2019; Hasan and Shang 2023). The electrical resistivity method (ERM) employs artificially generated current to determine the electrical resistivity (ρ) (or conductivity σ) of subsurface crustal materials. Its surveying principles involve two current electrodes for injecting electrical current into the subsurface, while the resulting potential difference (voltage) is measured between the other two electrodes known as potential electrodes (Daily et al. 2005; Akingboye et al. 2020; Akingboye and Osazuwa 2021; Abdullah et al. 2022). This measurement enables the determination of apparent resistivity (ρ_a) to ascertain the true resistivity of homogeneous or heterogeneous crustal materials (Loke et al. 2013; Liu et al. 2020; Akingboye and Bery 2022a, 2023a). Importantly, the wide range of resistivity (and conductivity) values for different lithologies, as depicted in Fig. 2, underscores ERM's effectiveness in diagnosing various geological problems. These figures show the range of resistivity values for some rocks, soils, and minerals. The ranges of values are influenced by the diverse lithologies present in various geological terrains. Assigning a specific resistivity value to a particular lithology is challenging due to variations in rock/strata characteristics such as density, water affinity, structural deformities, grain and pore sizes, and degree of weathering, among others.

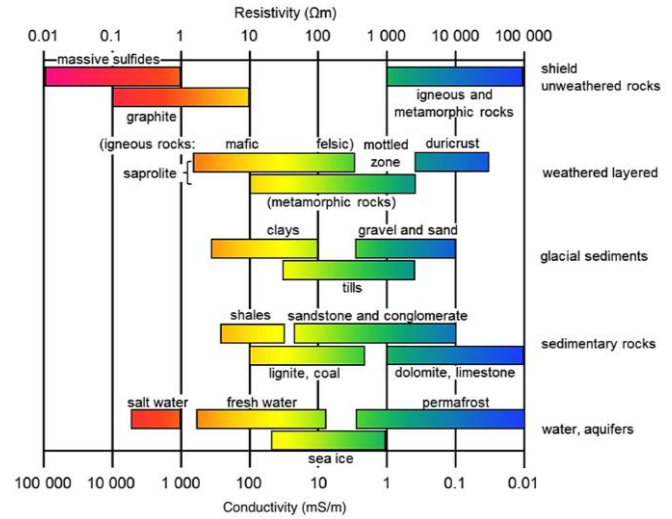


Fig. 2. A Typical resistivity (and conductivity) chart showing the range of values for geologic materials and some minerals (after Telford et al. 1990).

2.1.1 Theories and principles of electrical resistivity method

To ensure efficient performance in subsurface crustal investigations, ERM relies on a fundamental relationship governing electrical resistivity, current, and potential, rooted in Ohm's law (Telford et al. 1990; Loke et al. 2013; Binley 2015). This relationship calculates the potential difference for a point current source situated at x_c within a continuous medium, embodying a formulation of Ohm's law that, when combined with the conservation of current, yields Poisson's relation (Telford et al. 1990; Loke et al. 2013). Essentially, as illustrated in Fig. 3a, current injected from a single ground electrode on the earth's surface flows radially into the subsurface with uniform resistivity (ρ), resulting in a uniform current distribution across hemispherical shells (Telford et al. 1990; Loke 2002; Akingboye and Ogunyele 2019).

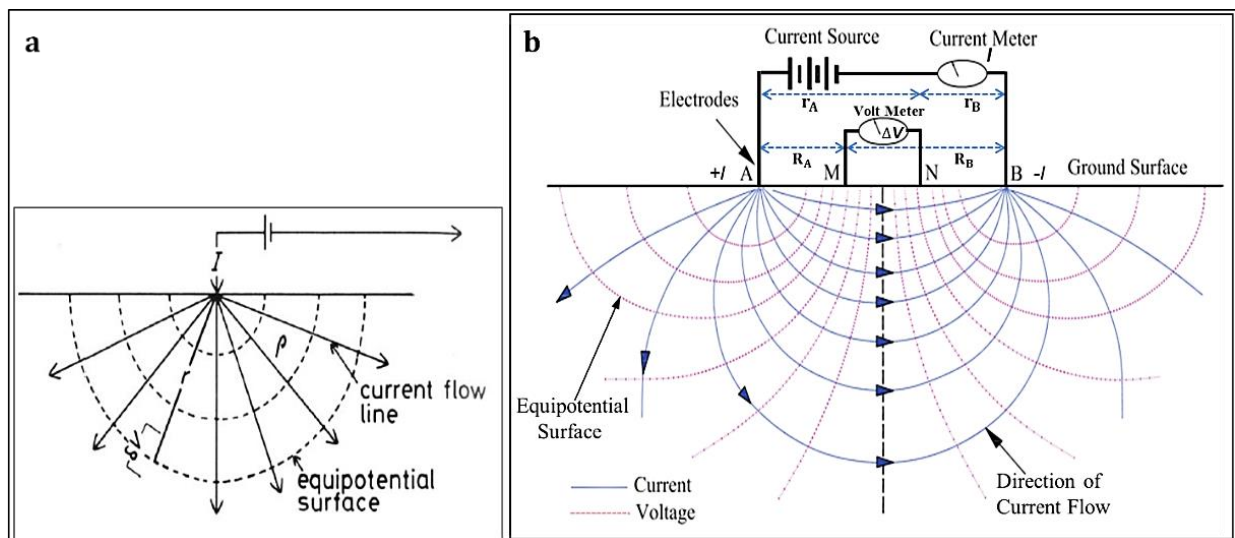


Fig. 3. (a) A schematic diagram of a single-point source electrode showing the flow of electric current in the subsurface. (b) A typical diagram of resistivity measurements using four electrodes with the generated current direction in the Earth's subsurface.

$$\nabla \cdot \left[\frac{1}{\rho(x,y,z)} \nabla \phi \right] = -\frac{\partial J}{\partial t} \quad (1)$$

Where ρ is the resistivity, ϕ is the potential, and J is the current density.

Theoretically, the relationship supporting the effective use of the four-electrode system (Fig. 3b) in resistivity imaging of surface–subsurface crustal formation is analogous to that of a single-point electrode system. Mathematical expressions indicate that the hemispherical shell, at a distance (r) from the electrode, has a surface area ($A = 2\pi r^2$), facilitating the calculation of current density (j) to give:

$$J = \frac{I}{A} = \frac{I}{2\pi r^2} \quad (2)$$

The charge density can also be given as $J = \frac{\varepsilon}{\rho}$;

Where ε is the electric field (or the gradient of a scalar potential) and is given as:

$$\varepsilon = -\nabla V \quad (3)$$

Hence, relating J with the potential gradient gives:

$$\nabla \phi = -\rho J = -\frac{\rho I}{2\pi r^2} \quad (4)$$

Integrating Eq. 4 gives the potential, as shown below:

$$V = \int \nabla \phi = -\int \frac{\rho I dr}{2\pi r^2} = \frac{\rho I}{2\pi r} \quad (5)$$

The general equation for the potential difference (ΔV) using a four-point measurement system (Fig. 3b) is based on relating the potential V_M at an internal electrode M, which is the sum of the potential contributions of V_A and V_B from the current source at A and sink at B, and that of electrode N (Kearey et al. 2002; Akingboye and Ogunyeye 2019). Therefore, the equation is given as:

$$V_M = V_A + V_B \quad (6)$$

From Eq. 5:

$$V_M = \frac{\rho I}{2\pi} \left(\frac{1}{r_A} - \frac{1}{r_B} \right) \quad (7a)$$

$$\text{Similarly, } V_N = \frac{\rho I}{2\pi} \left(\frac{1}{R_A} - \frac{1}{R_B} \right) \quad (7b)$$

Therefore, the ΔV between electrodes M and N is given as:

$$\Delta V = V_M - V_N = \frac{\rho I}{2\pi} \left\{ \left(\frac{1}{r_A} - \frac{1}{r_B} \right) - \left(\frac{1}{R_A} - \frac{1}{R_B} \right) \right\} \quad (8)$$

$$\rho = \frac{2\pi \Delta V}{I \left(\left(\frac{1}{r_A} - \frac{1}{r_B} \right) - \left(\frac{1}{R_A} - \frac{1}{R_B} \right) \right)} \quad (9)$$

k is the geometric factor for any used array, and is mathematically expressed as:

$$k = \frac{2\pi}{\left(\left(\frac{1}{r_A} - \frac{1}{r_B} \right) - \left(\frac{1}{R_A} - \frac{1}{R_B} \right) \right)} \quad (10)$$

It has also been considered in some literature as:

$$k = \frac{2\pi}{\left(\left(\frac{1}{r_1} - \frac{1}{r_2} \right) - \left(\frac{1}{r_3} - \frac{1}{r_4} \right) \right)} \quad (11)$$

Note that; $r_1 = r_A$; $r_2 = r_B$; $r_3 = R_A$; and $r_4 = R_B$

$$\text{Recall that } R = \frac{\Delta V}{I} \quad (12)$$

Therefore, the ρ_a of a crustal body can be mathematically expressed as:

$$\rho_a = kR \quad (13)$$

2.2. Electrode array performance evaluation in electrical resistivity surveys

Electrode array performance evaluation is essential in electrical resistivity surveys to assess the effectiveness of different array configurations in accurately delineating subsurface structures. This evaluation involves analyzing various factors such as data resolution, depth penetration, and sensitivity to geological features (Abdullah et al. 2018; Akingboye and Bery 2021a). The systematic arrangement of electrical imaging electrodes into various types and array configurations is crucial for land (ground and crosshole) and underwater surveys. Typically, four electrodes comprising two current and two potential electrodes are utilized for ERM imaging. The choice of electrode array configuration significantly impacts the method's noise reduction and its ability to identify lateral and vertical structures effectively. To enhance the performance of imaging electrodes, considerations such as sensitivities, resolution capacities, electrode spacing, spread length, injected current, probing depth, and noise attenuation must be carefully taken into account (Auken et al. 2015; Binley et al. 2015; Akingboye and Bery 2021b; Abdullah et al. 2022; Akingboye 2024). By systematically comparing array performance through field testing and numerical simulation, researchers can optimize survey design and data interpretation, ultimately enhancing the reliability and resolution of resistivity surveys.

Electrical imaging electrode arrays prove effective across various survey dimensions, accommodating both small- and large-scale 3- and 4-D surveys with versatility (Merritt 2014; Cheng et al. 2019; Bièvre et al. 2021; Loke et al. 2022; Zakaria et al. 2022; Akingboye and Bery 2023a). Achieving a high-resolution inverse model is feasible with small electrode spacing and short traverse distances, enhancing the shallow probing depth and facilitating easy current penetration (Akingboye and Bery 2023a). It is worth noting that not all metallic electrodes are suitable for use in these arrays due to challenges like induced cultural or self-potential noise, current relays,

low conductivity, poor signal-to-noise ratio, and inadequate structural resolution. Galvanized iron and aluminum electrodes are particularly sensitive to noise. However, under specific conditions, all electrodes can be utilized with any array type, given short survey durations (Daily et al. 2005; LaBrecque and Daily 2008). Copper electrodes excel in rapid current injection due to their high conductivity, despite being less common due to higher costs compared to other materials. On the other hand, stainless-steel electrodes, preferred for profiling and depth-sounding surveys, offer high sensitivity and relatively lower costs, albeit with lower conductivity and susceptibility to corrosion compared to copper (LaBrecque and Daily 2008; Akingboye and Bery 2021a). Both electrode types are vulnerable to subsurface cultural or self-potential noise, which can be mitigated by employing an alternating power source (Binley and Kemna 2005).

In practice, both conventional and optimized electrode arrays utilize two current and two potential electrodes to map lateral and vertical electrical variations and generate 1-, 2-, 3-, or 4-D resistivity models (Loke 2002; Abdullah et al. 2022; Loke et al. 2022; Akingboye et al. 2022). However, their configurations involve repositioning the current and potential electrodes, allowing some arrays to employ variations such as one current and one potential electrode; two currents and one potential electrode; or one current and two potential electrodes, with the remaining electrodes positioned at an infinite distance of about 20 times the normal electrode separation (Binley et al. 2015; Hojat et al. 2020; Rucker et al. 2021b; Zakaria et al. 2022). The configurations, sensitivity patterns, and performances of some commonly used arrays in ERM are shown in Fig. 4. Arrays can have multiple configurations in resistivity surveys, employed to optimize soil-rock characterization.

For instance, the Wenner array offers three configurations: Wenner-alpha (α), Wenner-beta (β), and Wenner-gamma (γ), with configurations denoted as C1P1P2C2, C2C1P1P2, and C1P1C2P2, respectively (Fig. 4a–c). Wenner arrays excel in noisy environments, enhancing vertical structure delineation, albeit with limited horizontal sensitivity for certain formations (Loke et al. 2013; Merritt 2014). In comparison, the Schlumberger array, similar to Wenner- α in configuration (C1P1P2C2), features closely spaced potential electrodes P1P2 (Fig. 4d). The Wenner–Schlumberger array (Fig. 4e), a hybrid of both the Wenner- α and the Schlumberger arrays, is moderately sensitive to both horizontal and vertical structures, which is ideal for high-resolution soil-rock models (Loke 2002; Abdullah et al. 2019, 2022). Compared to dipole-dipole, Schlumberger offers narrower model coverage with a slightly better horizontal resolution, while Wenner–Schlumberger provides a deeper probing depth and wider data coverage, albeit with a weaker signal (Loke 2002; Loke et al. 2013; Akingboye and Ogunyele 2019).

The dipole-dipole array is widely used in ERM and IP surveying for its low electromagnetic coupling effect and effective depth sounding (Loke 2002; Akingboye et al. 2022; Akingboye 2022). It comes in two configurations: the normal dipole-dipole array (Fig. 4f) and the equatorial dipole-dipole array (Fig. 4g), configured as C2C1P1P2. This array's high sensitivity to horizontal and resistivity variations between electrodes makes it suitable for vertical structural

delineation, such as igneous dykes and cavities. However, its ability to delineate horizontal structural elements like sills and sedimentary layers is somewhat limited (Abdullah et al. 2018; Zhou 2019; Rucker et al. 2021b).

The pole-dipole and pole-pole arrays are common alternatives, each with distinct advantages and limitations due to electrode positioning. The pole-dipole array (Fig. 4h), with electrodes C1P1P2 and a distant electrode C2 placed at a distance greater than 20 times the electrode spacing, offers weaker signal strength but lower sensitivity to telluric noise compared to the dipole-dipole array (Bery 2016). However, it may produce asymmetrical resistivity anomalies, requiring forward and reversed electrode arrangements for accurate surveys (Hasan and Shang 2023). Conversely, the pole-pole array (Fig. 4i), comprising electrodes C1P1 and distant C2 and P2 at an infinite distance, provides broad horizontal imaging and increased probing depth (Loke et al. 2013; Akingboye and Ogunyele 2019). However, it is more susceptible to telluric noise, often resulting in slightly subpar inversion models with structural artifacts, making it ideal for surveys with electrode spacing ≤ 10 m (Zhou and Greenhalgh 2000; Bing and Greenhalgh 2001). Loke and Barker (1996a) optimized the pole-pole array with a cross-diagonal (along x- and y-directions) surveying technique to reduce time and effort while ensuring quality data in 3-D surveys.

The multi-electrode gradient array's configuration encloses the potential electrodes (P1P2) within C1 and C2 (Fig. 4j). The current injected via separation $(s + 2)a$, and the resulting voltages are simultaneously measured through the potential electrode spacing (a). The maximum number of potential readings for injected current and the separation between potential electrodes depend on (s) (Binley 2015; Zhou et al. 2020). The azimuthal square array, featuring four electrodes arranged in a square around a central point offers three configurations: alpha (α), beta (β), and gamma (γ) square arrays (Fig. 4k–m), distinguished by interchangeable electrode setups (Habberjam 1972; Matias and Habberjam 1986; Loke et al. 2015c; Udosen and George 2018). The symmetrical expansion of the square array about its center is shown in Fig. 4n, while Fig. 4o represents the rotation of the square array about its midpoint at increments of 15° . The square array's center serves as the measurement location, with electrode spacing determined by the desired current penetration and investigation depth (Bayewu et al. 2016; Udosen and George 2018). While the depth of maximum current penetration typically equals the electrode spacing, large resistivity contrasts at the near-surface can reduce this depth (Lane et al. 1995; Udosen and George 2018). Edwards (1977) estimated the investigative depth as 0.451 times the electrode spacing. The depth value can progressively be increased by $\sqrt{2}$ (Fig. 4m), as suggested by Habberjam and Watkins (1967). To assess directional resistivity variation with azimuth, the square array is initially oriented to true north, with measurements taken at intervals of 15° (or higher) by rotating the array about its center from 0 to 180° (Fig. 4o). Udosen and George (2018) recommend the γ -square array's resistivity (or resistance) to be within $\pm 3\%$ for accurate tri-potential checking.

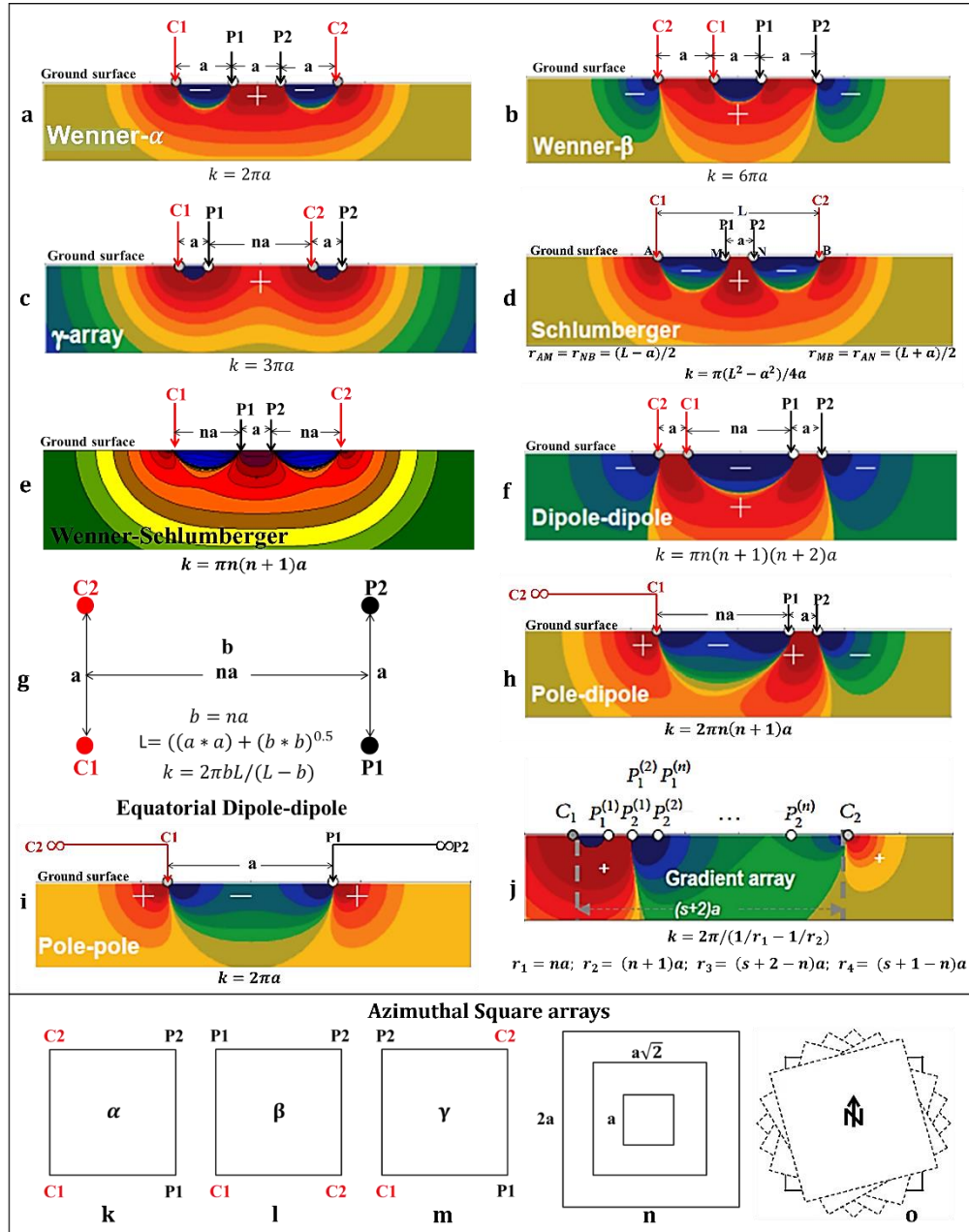


Fig. 4. Schematic diagrams of commonly used arrays in ERM with their configurations and sensitivity patterns alongside their computed geometric factors. The current electrodes are denoted as C1 and C2, while P1 and P2 represent the potential electrodes. n signifies a positive integer value for the dipole separation factor, a denotes the electrode spacing, k represents the geometric factor, and ∞ indicates a larger electrode separation approximately 20 times the normal spacing (adapted from Loke 2002; Akingboye and Ogunyele 2019).

2.3 One-dimensional electrical resistivity sounding and modeling.

The 1-D electrical resistivity imaging technique is primarily utilized for vertical electrical sounding (VES), typically employing the Schlumberger array, although the Wenner array can also be employed, with the dipole-dipole technique being less common (Singh 2005; Akintorinwa et al. 2020; Akingboye 2022; Akingboye et al. 2023). In 1-D resistivity processing, computed ρ_a values are plotted against $AB/2$ or station distance on tracing paper placed on a

bi-logarithm or log-log graph sheet for quality assurance purposes. If a curve displays anomaly peaks in contrast to surrounding stations, the processing procedure is repeated to reduce uncertainties caused by poor electrode grounding, circuit relays, or buried artifacts (Telford et al. 1990; Oladapo et al. 2004). Various software types can be utilized for the inversion of VES datasets, employing iterative curve-matching techniques to generate the model resistivity curve after a predefined number of iterations. This process allows for the quantitative interpretation of the approximate number of layers, as well as their resistivity and thickness values, achieved by smoothing

the produced curves. Typical examples of 1-D models used for interpreting subsurface scenarios are depicted in Fig. 5.

VES curve models are quantitatively interpreted based on their curve types, primarily including A-, Q-, H-, and K-types (Fig. 6), with other curve types resulting from combinations of these common curve types. While the VES method has demonstrated utility in geological applications like mapping the water table, where the 1-D

model is approximately (Oladapo et al. 2004; Akingboye et al. 2022), it is crucial to acknowledge that VES is a single-point probing method and thus cannot capture lateral changes, potentially leading to errors in interpreted layer resistivity and/or thickness over large areas. For more accurate model results, multiple comprehensive VES models along a profile must be positioned side by side for layer correlation and delineation.

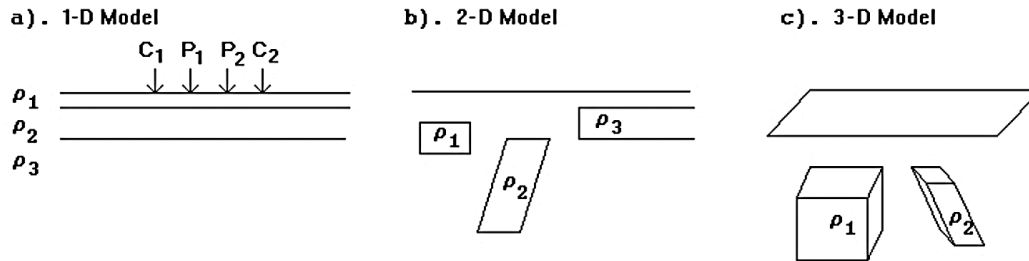


Fig. 5. Typical models used in the interpretation of resistivity measurements (after Loke 2002).

2.4 Induced polarization method

The IP method, introduced in the early 1920s by Conrad Schlumberger (Schlumberger 1920), involves a current-stimulated electrical phenomenon measured in earth materials as a delayed voltage response, known as induced polarization. This process quantifies the material's capacity to hold charges after the injecting current is stopped, referred to as chargeability (Dahlin et al. 2002; Binley 2015; Biosca et al. 2020; Lenhare and Moreira 2020). Chargeability, related to resistivity, is typically measured in msec (or mV/V) during IP surveys.

In practice, IP entails a primary (low frequency) electrical field/current that stores electrical charges reversibly in the ground. This reversible storing of electrical charges is facilitated by the porous material's polarization length scales, which correlate to grain and pore scales (Binley and Kemna 2005; Revil et al. 2022). As a result, a secondary electrical field/current is induced by the electrodiffusion of the stored charge carriers through gradients in the electrochemical potential, attributable to the primary current or electrical field (Revil et al. 2022). Earth materials rich in sulfide minerals, clay, and graphite tend to exhibit high chargeability, with factors such as mineral type, grain size, electrolyte properties in pore space, and fluid-surface interactions influencing chargeability variability within the same regions (Dahlin et al. 2002; Revil et al. 2022).

Furthermore, both IP and ERM methods are influenced by factors like lithology, pore fluid chemistry, void spaces, and soil water content (Slater et al. 2010; Akingboye and Bery 2021b; Hasan and Shang 2023). Consequently, both methods can address diverse geophysical challenges. However, the IP method exhibits particular sensitivity to changes induced by the membrane polarization effect resulting from clay in geological formations or the electrode polarization effect caused by conductive minerals, partly due to electrolytic and electronic current flow (Binley and Kemna 2005; Akingboye and Bery 2021a). In imaging, soil resistivity is governed by electrolytic and electronic current flow (Binley and Kemna 2005;

Akingboye and Bery 2021a). In imaging, soil resistivity is governed by electrical conduction within pore fluid, while IP is significantly affected by processes at the fluid-grain interface (Binley and Kemna 2005). Combining IP with ERM is advantageous, as IP identifies clay through high chargeability and water through low chargeability (Slater and Glaser 2003).

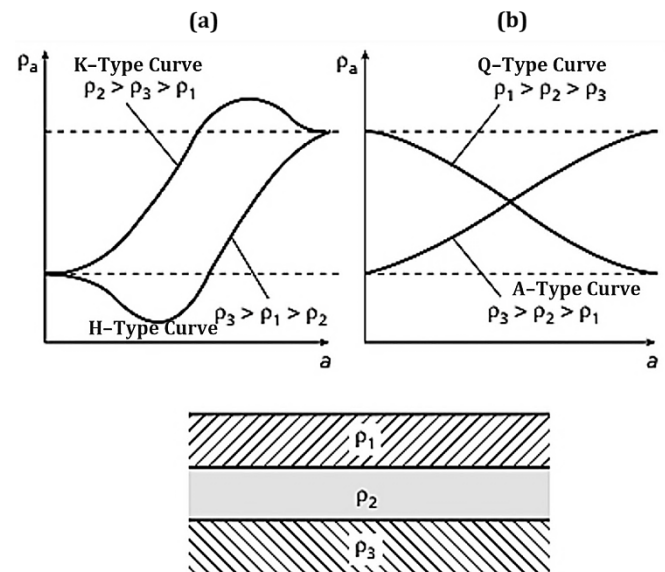


Fig. 6. Schematic model of the main VES curve types observable over a three-layer horizontal body due to the variation of apparent resistivity with electrode separation (modified after Kearey et al. 2002).

The IP imaging technique is widely employed in various subsurface investigations, resolving ambiguities encountered in ERM geological interpretations (Kemna et al. 2004; Lenhare and Moreira 2020; Rucker et al. 2021b; Revil et al. 2022). It is especially valuable when there is minimal resistivity contrast between the target and host or when multiple resistivity models are plausible (Slater and

Lesmes 2002; Binley and Kemna 2005; Jones 2007). Mineral prospecting, particularly for disseminated and massive sulfides, is a primary application of IP due to the common chargeability of these ore minerals (Martínez et al. 2019; Revil et al. 2022; Adrian et al. 2022). Hydrogeological applications also benefit from IP surveys (Slater et al. 2010; Akingboye and Bery 2021b), mapping saltwater intrusions, particularly in aquifers with clayey layers (Kumar et al. 2021). In engineering site investigations, IP assists in distinguishing clay-rich soil from water and/or sand (Arifin et al. 2020). There is a growing interest in utilizing chargeability to identify and delineate subsurface pollutants (Maurya et al. 2018; Rey et al. 2020). Additionally, IP has garnered attention in oil and gas exploration (Cardarelli and Di Filippo 2009; Biosca et al. 2020).

During IP surveys, a four-electrode set-up is employed on the ground surface or in cross boreholes, utilizing equipment similar to ERM but with a current approximately ten times that of a resistivity spread (Kearey et al. 2002). Although theoretically any conventional electrode array can be used, dipole-dipole, pole-dipole, and Schlumberger layouts are common (Binley and Kemna 2005; Revil et al. 2022). Electrode spacings during IP field surveys vary widely, ranging from 0.5 m in engineering studies to 300 m in reconnaissance surveys (Kearey et al. 2002; Rucker et al. 2021a). Noise from telluric currents and barren rocks, or from measuring equipment, can affect IP surveys, necessitating careful consideration during data collection (Kearey et al. 2002). Both time-domain and frequency-domain measurement modes are possible in IP field survey measurements (Binley and Kemna 2005; Günther and Martin 2016; Revil et al. 2022). Time-domain IP records voltage decay, as shown in Fig. 7, with time after ceasing the injecting current, reflecting the complex relationship between electrical charge polarization and conduction within the pore fluid and along grain boundaries (Binley and Kemna 2005). On the other hand, frequency-domain IP measures a phase-shifted voltage relative to an injected alternating current and employs the percent frequency effect (PFE) as a key metric (Binley and Kemna 2005; Günther and Martin 2016).

As defined by Seigel (1959), the mathematical theory supporting

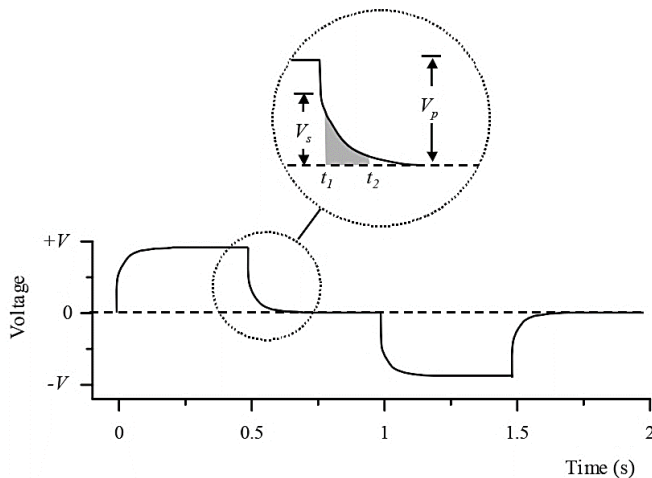


Fig. 7. Typical measurement of time-domain induced polarization (after Binley and Kemna 2005).

the apparent chargeability (m_a) measurement of IP is expressed in Eq. 14.

$$m_a = \frac{V_p}{V_s} \quad (14)$$

The primary voltage is denoted as V_p while V_s is the secondary voltage. It is important to note that measuring the V_s in the field is quite difficult; hence an integral measure of m_a , as illustrated in Fig. 7 and mathematically represented in Eq. 15, is used.

$$m_a = \frac{1}{t_2 - t_1} \frac{1}{V_p} \int_{t_1}^{t_2} V(t) dt \quad (15)$$

Undoubtedly, there are numerous ways to measure IP. The chosen time window (t_1 to t_2) employed will affect the measured m_a , as the PFE impacts the selected injection frequencies and impedance phase angle. Moreover, factors like grain-surface polarization and pore-fluid conductivity affect these parameters. IP follows imaging procedures similar to ERM but typically employs non-polarizing electrodes, such as copper-copper sulfate electrodes (Telford et al. 1990). Recent studies highlight stainless steel or copper electrodes, commonly used in ERM surveys, as most suitable for IP imaging (Dahlin et al. 2002; Slater et al. 2010; Akingboye and Bery 2021a). According to Binley and Kemna (2005), cables for IP surveys should be short and isolated from those connected to potential electrodes to mitigate electromagnetic coupling effects. Injected currents in IP measurements are typically higher than those in ERM, especially when using the dipole-dipole array. However, IP shares similar limitations with ERM, including potential strong IP effects from water-filled shear zones and sediments containing graphite, which can have significant economic implications (Li and Oldenburg 2000; Slater et al. 2010; Lenhare and Moreira 2020).

IP measurement modes commonly made are the PFE and the metal factor (MF) (Kearey et al. 2002). PFE and MF are mathematically defined as:

$$PFE = \frac{(\rho_{0.1} - \rho_{10})}{\rho_{10}} \quad (16)$$

$$MF = 2\pi \times 10^5 \frac{(\rho_{0.1} - \rho_{10})}{\rho_{0.1}\rho_{10}} \quad (17)$$

Where $\rho_{0.1}$ and ρ_{10} are the apparent resistivities at measuring frequencies of 0.1 and 10 Hz.

Quantitatively interpreting IP models proves more intricate compared to ERM (Olayinka 1992; Revil et al. 2022). Thus, IP responses are often analyzed using indirect interpretation modeling for simpler features like spheres, ellipsoids, dykes, vertical contacts, and horizontal layers. Additionally, laboratory modeling or simulation serves as an indirect interpretation method for observed IP anomalies (Akingboye and Bery 2021a). However, historically, much of IP interpretation has been qualitative, focusing on determining the location, lateral extent, dip, and depth of anomalous bodies (Hasan et al. 2021; Hasan and Shang 2023). Recently, interpretations have increasingly utilized various modeling approaches such as supervised and unsupervised machine learning as

well as more refined conventional arrays and 3-D modeling (Lenhare and Moreira 2020; Rucker et al. 2021b; Martorana et al. 2023). Recently, Bala et al. (2024) recognized the importance of resistivity–chargeability relationships through a supervised statistical approach, applying them in the sedimentary–basement (granitic) terrain of Langkawi, Malaysia. This offers significant potential for promptly and accurately addressing environmental issues specific to the study area. Leveraging this innovative relationship, geoscientists, engineers, and environmental practitioners can make informed decisions and efficiently manage environmental challenges, particularly during the pre-development stage.

2.5 Self-potential method

Though this study does not delve into SP, it is crucial to briefly touch upon its arrays and procedures for clarity in distinguishing among electrical survey arrays. Unlike IP and ERM, SP employs a distinct methodology. SP, based on measuring natural potential differences due to subsurface electrochemical reactions, utilizes specialized non-polarizable electrodes connected to a high-impedance millivoltmeter (Kearey et al. 2002; Jackson 2015). These electrodes, termed "porous pot" electrodes, contain either copper-copper sulfate (Cu–CuSO₄) or silver-silver chloride (Ag–AgCl) solution, the former for land surveys and the latter for marine/water surveys (Telford et al. 1990; Biswas and Sharma 2017; Hasan and Shang 2023). SP involves passive measurement of electric potential on the ground surface and in boreholes, often being more cost-effective and quicker to implement with simple equipment (Mao et al. 2015). Despite its potential for capturing changes in groundwater flow, chemistry, and temperature, SP's interpretation complexity and limited probing depth (approximately 30 m) relegate it to a lesser role in exploration compared to other electrical techniques (Kearey et al. 2002; Jackson 2015; Mao et al. 2015).

3. Electrical resistivity tomography

ERT, a noninvasive geoelectrical survey technique, emerged over a few decades for imaging subsurface features using resistivity measurements at the earth's surface, in boreholes, underwater, or on stream/river surfaces (Slater et al. 2000; Daily et al. 2005; Dahlin and Loke 2018; Perri et al. 2020; Akingboye and Bery 2023a). Continuous research aims to enhance ERT accuracy and efficiency, with advancements in survey techniques, inversion algorithms (Wilkinson et al. 2014; Loke et al. 2015b, 2022; Abdullah et al. 2019, 2022), and multi-physics coupling with other geophysical methods, integrating borehole or seismic data (Holmes et al. 2022; Zakaria et al. 2022; Hasan et al. 2023). Integration with machine learning, artificial intelligence, and statistical modeling holds promise for enhancing data interpretation and subsurface imaging (Aleardi et al. 2021; Liu et al. 2023b, a; Akingboye and Bery 2023a). Time-lapse ERT monitoring, termed TLERT, allows dynamic subsurface changes observation in 3- or 4-D ERT setups (Karaoulis et al. 2014; Palis et al. 2017; Arosio et al. 2017; Loke et al. 2022).

ERT operates on similar principles as ERM, employing four electrodes to minimize contact resistance and noise (Loke et al. 2013; Binley 2015; Akingboye 2022). Like conventional ERM, ERT injects

electrical current into the subsurface via current electrodes and measures potential differences with potential electrodes at constant traverse separations (Loke et al. 2013; Binley 2015; Husainy et al. 2023; Akingboye and Bery 2023b; Akingboye 2024). Increased electrode spacing enables deeper penetration, and apparent resistivity measured constructs a composite resistivity image, comprising pseudosections and inverse model resistivity sections, depicting soil-rock conditions from surface to subsurface (Dahlin and Loke 2018; Akingboye et al. 2020; Abdullah et al. 2022; Zakaria et al. 2022; Szalai et al. 2022; Raji et al. 2023; Akingboye 2024). The generated inverse resistivity model reveals variations in true resistivity responses, delineating subsurface units, interfaces, structures, and discrete bodies.

The technique offers numerous advantages over conventional ERM methods, including reduced operational costs and laborious manual electrode switching (Loke et al. 2014a, 2022; Delgado-Gonzalez et al. 2023). Its cost-effective data acquisition, high speed, and broad applicability to geological and environmental problems make it preferable for both small- and large-scale near-surface geological investigations (Gourdol et al. 2018; Bai et al. 2022; Dimech et al. 2022; Hasan et al. 2023). Additionally, its noninvasive nature minimizes subsurface disturbance, preserves structures, and provides high-resolution images for detailed investigations (Raji et al. 2023). These benefits are particularly advantageous for geophysicists, engineers, geologists, hydrogeologists, etc., enhancing the quality and resolution of subsurface geological models.

Despite its advantages, geological interpretation with ERT faces challenges due to lithological variation, pore fluid chemistry, and soil water (Daily et al. 2005; Loke et al. 2013; Akingboye 2024). Imaging resolution is limited by electrode spacing, inverse problem ambiguity, and subsurface heterogeneity (Daily et al. 2005; Binley 2015). Integrating ERT with IP and/or SP models can mitigate these limitations (Kumar et al. 2020; Hasan and Shang 2023). Closer electrode positioning, smaller spacing, and additional data from geotechnical surveys can help constrain inversion models (Wilkinson et al. 2006; Binley 2015; Akingboye and Bery 2021a, 2022a; Hasan et al. 2023). Integration with borehole logs is crucial for resolving ambiguities and differentiating features from artifacts (Doetsch et al. 2010; Akingboye 2024).

The applicability of ERT involves resolving complex hidden underground structures (Storz et al. 2000; Abdullah et al. 2022) as well as studying the spatiotemporal evolution of groundwater flow relative to landslide (or slope failure) (Palis et al. 2017; Bièvre et al. 2021; Zakaria et al. 2022). It is an effective tool in environmental studies to delineate contaminant plumes, monitor groundwater flow, and assess subsurface pollution (Mao et al. 2015; Helene et al. 2020; Akingboye et al. 2022; Hasan and Shang 2023). In agroeophysics, it is effective for evaluating soil properties, delineating water-nutrient exchange zones, and mapping plant-root zones (Aizebeokhai 2014; Cheng et al. 2019; Cordero-Vázquez et al. 2021). Archaeologists use it to locate buried structures and archaeological remains (Nero et al. 2016; Zangrando 2018; Raji et al. 2023). Mineral exploration also benefits from this (Gupta et al. 2019; Martínez et al. 2019; Sendrós et al. 2020).

3.1 ERT: field survey design and data acquisition techniques

ERT surveys can be conducted in 2-, 3-, and 4-D configurations, allowing for versatile applications on the surface of the earth, within crossholes, or underwater (also known as marine ERT), depending on the specific parameters of interest in the subsurface (Merritt et al. 2014; Abdullah et al. 2018; Loke et al. 2022; Akingboye and Bery 2023a). The distinction of 4-D ERT lies in its ability to monitor resistivity changes over time, distinguishing it from other survey types (Merritt 2014; Kuras et al. 2016; Loke et al. 2022). The equipment and methodologies for conducting ERT surveys are the same as those employed for ERM surveys, utilizing multi-electrode arrays and advanced data loggers (Fig. 8a) for efficient simultaneous data acquisition for both conventional and modified arrays, as depicted in Fig. 3 (Crook et al. 2008; Abdullah et al. 2018, 2022). Modern advancements, (e.g., ABEM Terrameter LS 2), integrate the Terrameter and Switching Unit into a single device, streamlining measurements and improving electrode automation.

2-D ERT land surveys are typically conducted using two or four sets of multicore cable reels (Fig. 8a–b), with evenly spaced take-outs connected to grounded electrodes. The electrodes not only inject currents and measure potential differences but also counteract electrode polarization, which can introduce noise during measurements (Daily et al. 2005; Zhou 2019). The initial profile length in measurement surveys is determined by the length of multicore cables. If the survey area exceeds this length, a roll-along technique can be employed, as shown in Fig. 8c, allowing for continuous data collection in both directions. The electrical measurements sequence (Fig. 8d), array type, and current injection levels are controlled by the resistivity meter, with a switching unit managing the injection and measurement electrodes. The resistivity data are gathered at various depths by measuring resistivity at multiples of the electrode spacing (a), typically up to 16 times or more (referred to as n levels) (Dahlin 1996; Loke 2002; Loke et al. 2013).

In 3-D surveys, pole-pole, pole-dipole, and dipole-dipole arrays are preferred for their improved resolution at the survey grid edges. However, optimized arrays have emerged as highly efficient in

improving survey outcomes (Wilkinson et al. 2006; Loke et al. 2010a; Tejero - Andrade et al. 2015; Abdullah et al. 2018, 2019, 2022). Field layouts typically adopt a square or rectangular grid pattern with uniform electrode spacing along both x and y directions (Fig. 8c), tailored to the geometry of the target body (Loke 2002). Based on reports of Loke (2002), 3-D resistivity measurements employ various methods: 1) measurements along potential directions with electrodes in a rectangular grid; 2) measurements along all grid lines, sometimes with limited angular data; 3) measurements in two directions along grid lines using a multi-electrode system with limited nodes; and 4) measurements along parallel 2-D survey lines, later inverted and merged, necessitating equal distances between these lines. Optimal coverage requires angular data, typically from categories one or two, rather than three or four, which may lack it. However, 4-D ERT surveys (or time-lapse ERT) now provide more desired information on complex terrains and spatiotemporal water/moisture changes by measuring resistivity variations over days, weeks, months, or years (Bergmann et al. 2012; Karaoulis et al. 2014; Bièvre et al. 2021; Loke et al. 2022).

3.2 Optimized electrode arrays in ERT surveys

In recent years, significant advancements in automatic procedures have aimed to optimize electrode configurations, particularly for 3-D surveys, leading to the development of new optimized arrays (Wilkinson et al. 2006; Loke et al. 2015a; Szalai et al. 2020; Abdullah et al. 2022). While comprehensive studies comparing optimized arrays to conventional ones are limited due to the novelty of the field, various optimized arrays, such as the L and Corner arrays, Compare R, and perimeter arrays with the noise-weighted optimized array, have been substantially demonstrated in recent works to be efficient in resistivity measurements, particularly in 3-D surveys (Wilkinson et al. 2006; Loke et al. 2010a; Abdullah et al. 2018, 2019, 2022). For instance, Wilkinson et al. (2006) introduced the Compare R array technique for automatically generating optimized arrays to maximize subsurface model resolution in 2-D resistivity surveys. Loke et al. (2010b) confirmed the effectiveness of the Compare R array, particularly in comparison

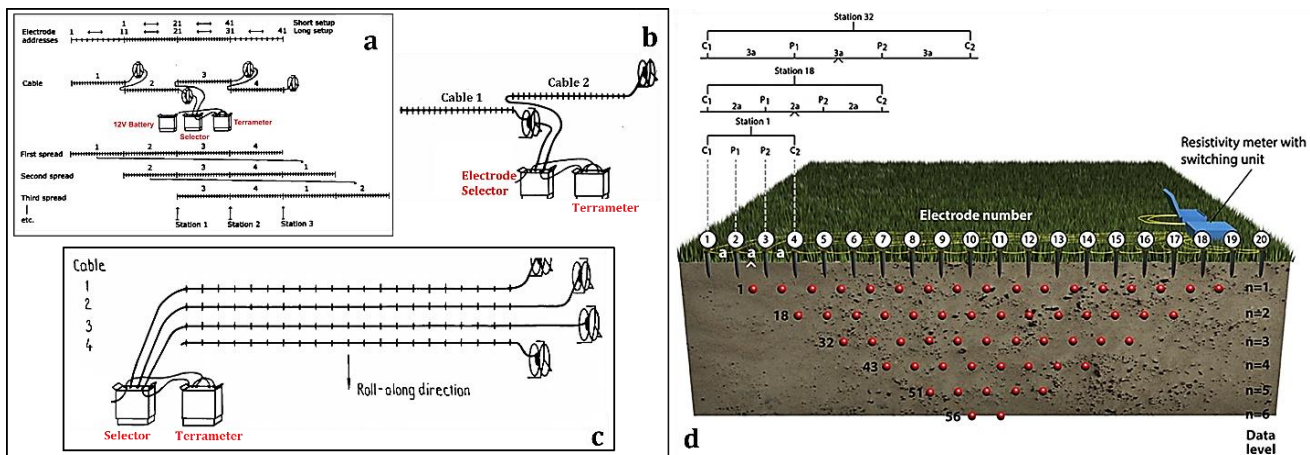


Fig. 8. Schematic diagrams for a 2-D typical system layout (a) using four and (b) two multicore cable reels. (c) A typical 3-D ERT survey layout showing a roll-along direction. (d) Schematic image of multi-electrode measurement sequence for a 2-D survey (after Loke et al. 2013).

to other techniques directly comparing model resolution matrices. To further enhance the resolution capabilities of optimized arrays, efforts have been made to reduce computation time and mitigate electrode polarization noise. Loke et al. (2010a, 2010b) employed parallel programming techniques and optimized computer code, significantly reducing calculation time. Additionally, Wilkinson et al. (2012) addressed electrode polarization noise and utilized data error estimates to improve array performance. Ongoing research, such as the evaluation of modified Compare R optimized arrays by Abdullah et al. (2018), continues to refine and assess the effectiveness of optimized arrays compared to conventional ones.

Optimized arrays play a crucial role in 3-D resistivity surveys, particularly in densely urbanized areas with complex geology, enabling the distinct resolution of both surficial and subsurface structures. Several array systems, including the "L" array and "L and Corner" arrays, have been utilized for such surveys (Chavez-Hernandez et al. 2011; Argote-Espino et al. 2013). The "L" array, initially proposed by Baker et al. (2001), deploys electrodes along orthogonal lines. Additionally, Argote-Espino et al. (2013) and Chávez et al. (2014) introduced the "horse-shoe geometry," which combines the "L," equatorial-dipole, and minimum-coupling (MC) array to resolve subsoil conditions beneath archaeological structures. In studies by Chavez-Hernandez et al. (2011), Argote-Espino et al. (2013), and Tejero-Andrade et al. (2015) confined "L" and "Corner" arrays along the perimeter of engineering structures were employed to determine subsurface resistivity distributions causing structural defects. However, these methods, often based on heuristic rules, may not be suitable for perimeters with smooth shapes, like circles, as they are typically developed for perimeters with sharp edges, such as rectangles. To address this limitation, Loke et al. (2015c) modified the "Compare R" technique (Loke et al. 2014b) to automatically generate electrode arrays optimized for surveys conducted along the perimeter of a confined area. This innovation leverages the latest improvements to enhance the resolution of surveys conducted in such environments.

For instance, Abdullah et al. (2019a) conducted a study within the Universiti Sains Malaysia (USM) aimed at enhancing the resolution of 3-D resistivity surveys along the perimeter of a confined area by utilizing optimized perimeter arrays developed by Loke et al. (2015b). They introduced a less noisy modified version called noise-weighted optimized perimeter arrays. Possible arrays for 2-D lines using perimeter surveys were generated in Fig. 9a–b, forming closed loops to create a sequence of optimized perimeter arrays (Fig. 9c–f). Comparing with standard "L and Corner" arrays proposed by Tejero-Andrade et al. (2015), the study utilized synthetic models and field survey datasets. To mitigate decreasing resolution towards the center and depth due to increased electrode distance, the authors adjusted array algorithms to assign greater weights to cells within the survey loop, following Loke et al. (2015b) weighting procedure, resulting in high-resolution models. The real-time field model results generated, including standard "L and Corner", optimized perimeter, and the noise-weighted optimized perimeter arrays, as shown in Fig. 10a–c, respectively, showed comparable subsurface lithological conditions at varied depths. However, the resulting 3-D models from the

optimized perimeter and the noise-weighted optimized perimeter arrays (Fig. 10b–c) outperformed the "L and Corner" array (Fig. 10a) in capturing the anomalies of interest as the depth of investigation increased. This advancement marks a significant step forward for researchers interested in 3-D surface–subsurface characterization around the perimeters of detected anomalies, especially in engineering and environmental geophysical studies.

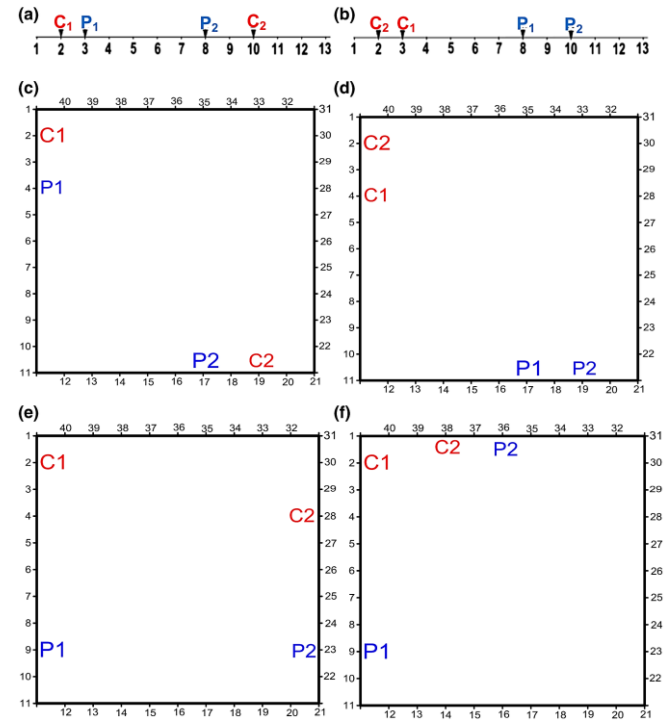


Fig. 9. Typical array configuration of (a) alpha and (b) beta types for a 2-D survey traverse. (c) alpha and (d) beta arrays with electrodes on perpendicular segments of a square loop; (e) alpha array with electrodes on opposing segments; (f) alpha array with electrodes on the first and fourth segments (adapted from Abdullah et al. 2019a)

3.3 Crosshole (borehole-based) electrical surveys

Crosshole electrical surveys address the limitation of surface electrical imaging by enhancing subsurface imaging resolution through various quadrupole combinations of current and potential electrodes placed within boreholes or between boreholes and the surface (Slater et al. 2000; Kemna et al. 2004; Loke et al. 2013; Yang et al. 2021), Fig. 11a. Crosshole electrical imaging can be employed for ERM and IP, particularly ERT. To achieve optimal resolution, the separation between boreholes should not exceed approximately 0.75 times the length of the borehole array (Daily et al. 2005). Borehole layouts, whether regular or irregular, are chosen based on the specific site conditions and investigative requirements. However, accurate positioning of borehole electrodes presents challenges, necessitating consideration of random and systematic electrode offsets and borehole deviations (Slater et al. 2000; Wilkinson et al. 2006; Yang et al. 2021).

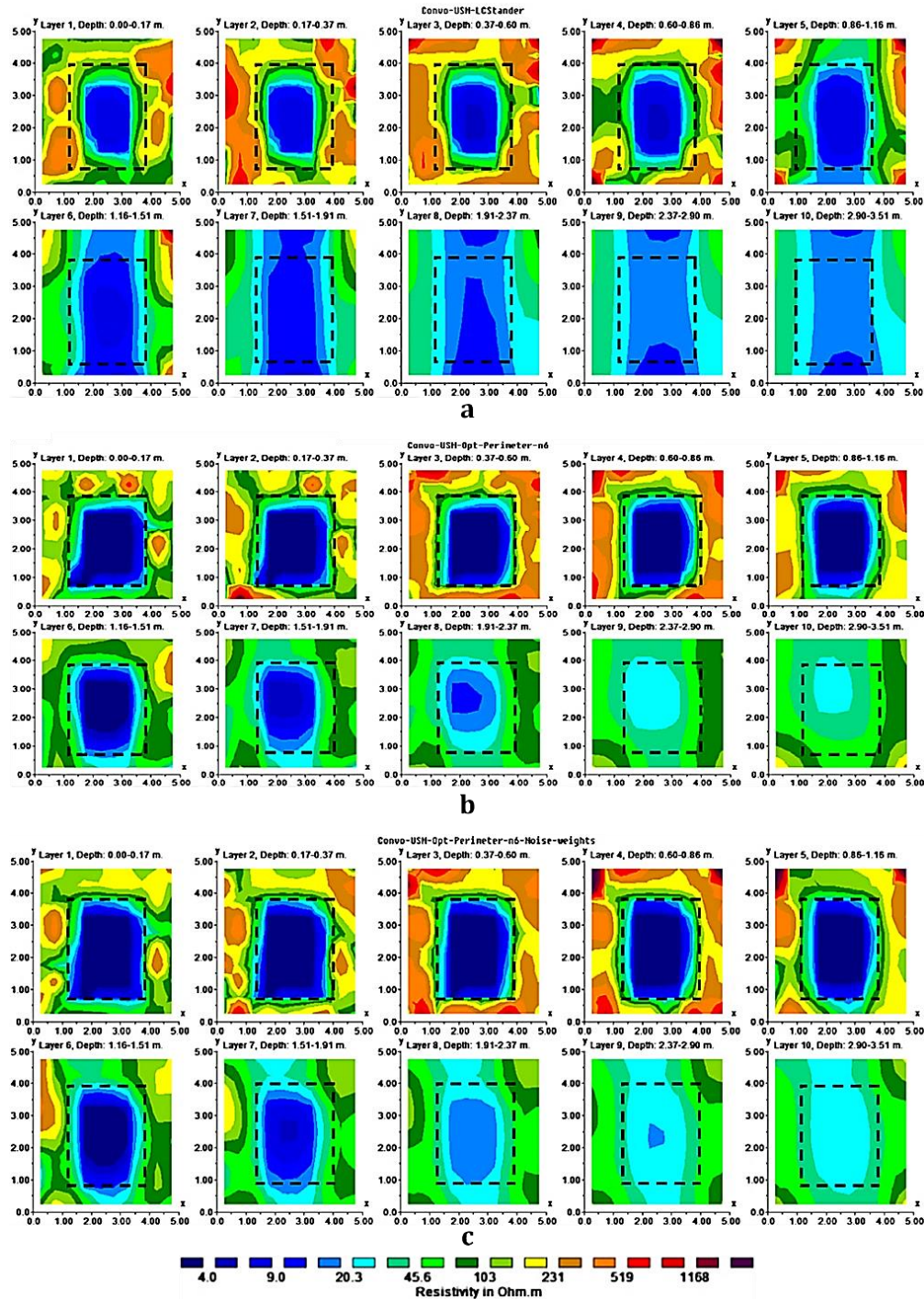


Fig. 10. Resistivity models for (a) standard "L and Corner", (b) optimized perimeter, and (c) the noise-weighted optimized perimeter arrays, for real-time field survey within the Universiti Sains Malaysia (adapted from Abdullah et al. 2019a).

Recent advancements involve integrating ERT data with apparent chargeability data from induced polarization techniques or borehole logs to precisely delineate lithological boundaries, particularly distinguishing clay from water-saturated soils (Slater and Lesmes 2002; Kemna et al. 2004). These are considered as best direct and indirect geophysical methods to effectively characterize pore fluid chemistry, void spaces, soil water content, and other subsurface

properties (Kemna et al. 2004; Binley and Kemna 2005). Moreover, the integration of advanced technologies, methodologies, and algorithms holds great promise for further advancing the capabilities of crosshole ERT in subsurface imaging and characterization (Doetsch et al. 2012). These developments include the use of advanced borehole logging technologies, such as fiber-optic distributed acoustic sensing (DAS) and electromagnetic methods,

with crosshole ERT to precisely position electrodes and monitor subsurface conditions in real-time (Bergmann et al. 2016; Folch et al. 2020).

Furthermore, ongoing efforts aim to integrate crosshole ERT with complementary geophysical and geotechnical methods, such as seismic tomography, ground-penetrating radar, and cone penetration testing, to provide a comprehensive understanding of subsurface structures and properties. This multi-method approach enables synergistic data interpretation, allowing for more accurate characterization of complex geological formations, hydrological processes, and environmental conditions (Li and Oldenburg 2000;

Slater and Lesmes 2002; Dimech et al. 2022). Most especially, crosshole ERT is very useful for time-lapse ERT (TLERT) for monitoring subsurface's groundwater and/or moisture level changes, monitoring of tracer concentrations, etc (Dimech et al. 2022). A typical survey model depicting the measurement procedure for surface and crosshole electrode arrangements for tracer monitoring is shown in Fig. 11b. To enhance the surface response of anomalous bodies, Yang et al. (2021) proposed a 3-D inversion technique utilizing damped least-squares, finite difference simulations, and the incomplete Cholesky conjugate gradient method to enhance surface responses of anomalous bodies.

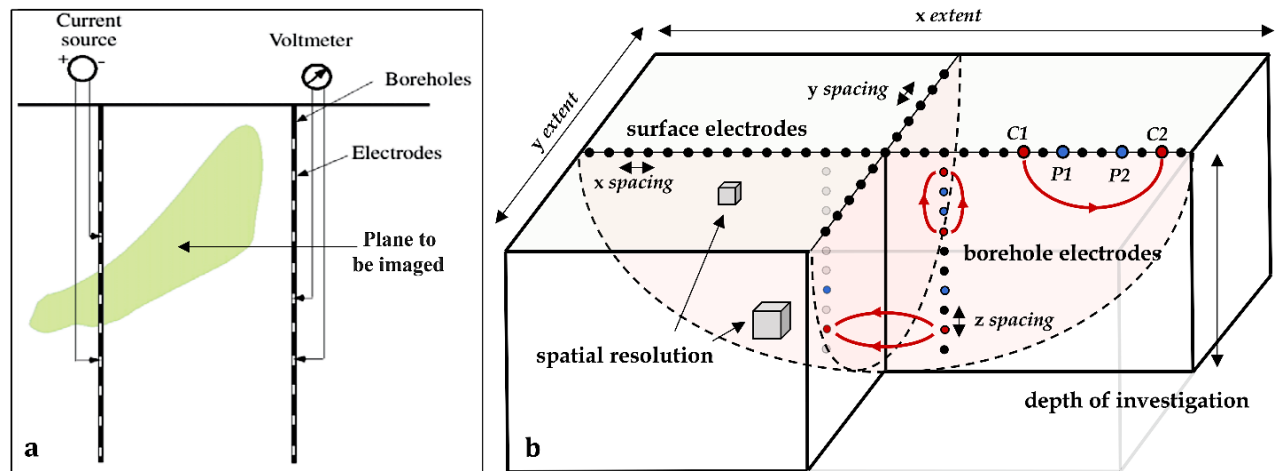


Fig. 11. (a) Schematic of crosshole electrical resistivity survey measurement layout (modified after Daily et al. 2005). (b) Schematic crosshole spatiotemporal parameters of TLERT survey approach (adapted from Dimech et al. 2022).

3.4 Surface- and sea-bottom-towed marine-based ERT surveys

Marine resistivity is an indispensable noninvasive tool in geotechnical, geo-environmental, and coastal/marine studies, providing vital insights into water sub-bottom geology, sedimentary structures, and hydrological processes (Snyder et al. 2002; Day-Lewis et al. 2006; Passaro 2010; Orlando 2013). Moreover, it contributes significantly to the understanding of suitable areas for engineering foundations, coastal erosion, coastal habitat mapping, and groundwater discharge (Snyder et al. 2002; Passaro 2010; Ronczka et al. 2017; Dahlin and Loke 2018; Benevides et al. 2024). Over the years, researchers have developed and utilized mobile ERT imaging systems for both land and underwater surveys (Goto et al. 2008; Passaro 2010; Hermans and Paepen 2020), as shown in Fig. 12. Each mode presents unique advantages and challenges, influencing the exploration of underwater lithologies and their compositions.

Continuous resistivity profiling (CRP) serves as the standard technique in underwater ERT imaging, employing floating electrode arrays towed along the water surface (Snyder et al. 2002; Day-Lewis et al. 2006), as depicted in Fig. 12a. Dipole-dipole arrays are commonly utilized due to their favorable geometry, data-acquisition speed, and compatibility with multichannel-resistivity meters (Day-Lewis et al. 2006). Additionally, dipole-dipole and multiple gradient

arrays prove particularly effective for detecting fracture zones in highly resistive bedrock, offering enhanced depth penetration and sensitivity to vertical resistivity boundaries (Loke et al. 2013). Importantly, floating electrodes are recommended for water columns <25% of total investigation depth, offering ease of deployment and increased productivity (Akingboye and Ogunyele 2019).

The interpretation of data collected using floating electrodes is straightforward, treating the water layer as a layer of unknown or fixed resistivity, as illustrated in Fig. 12b. This mode is particularly suitable for mapping resistivity changes in the water layer, such as variations in water conductivity or freshwater-saltwater interfaces (Passaro 2010; Ronczka et al. 2017; Wang et al. 2018). However, in saline water, resolution may be limited as the thickness of the water layer increases, leading to reduced current penetration. To address the limitations associated with floating electrodes, the sea (water)-bottom electrode mode (Fig. 12c) is employed (Loke et al. 2013). In this mode, electrodes are positioned directly on the waterbed, offering improved depth of investigation and resolution. However, specialized marine cables capable of withstanding increased stress and reduced survey speeds are required (Day-Lewis et al. 2006; Orlando 2013). Processing marine ERT data requires meticulous parameter consideration due to weak current distribution, deep target layers, inversion time, and resistivity contrast between water and bedrock (Loke et al. 2013; Orlando 2013).

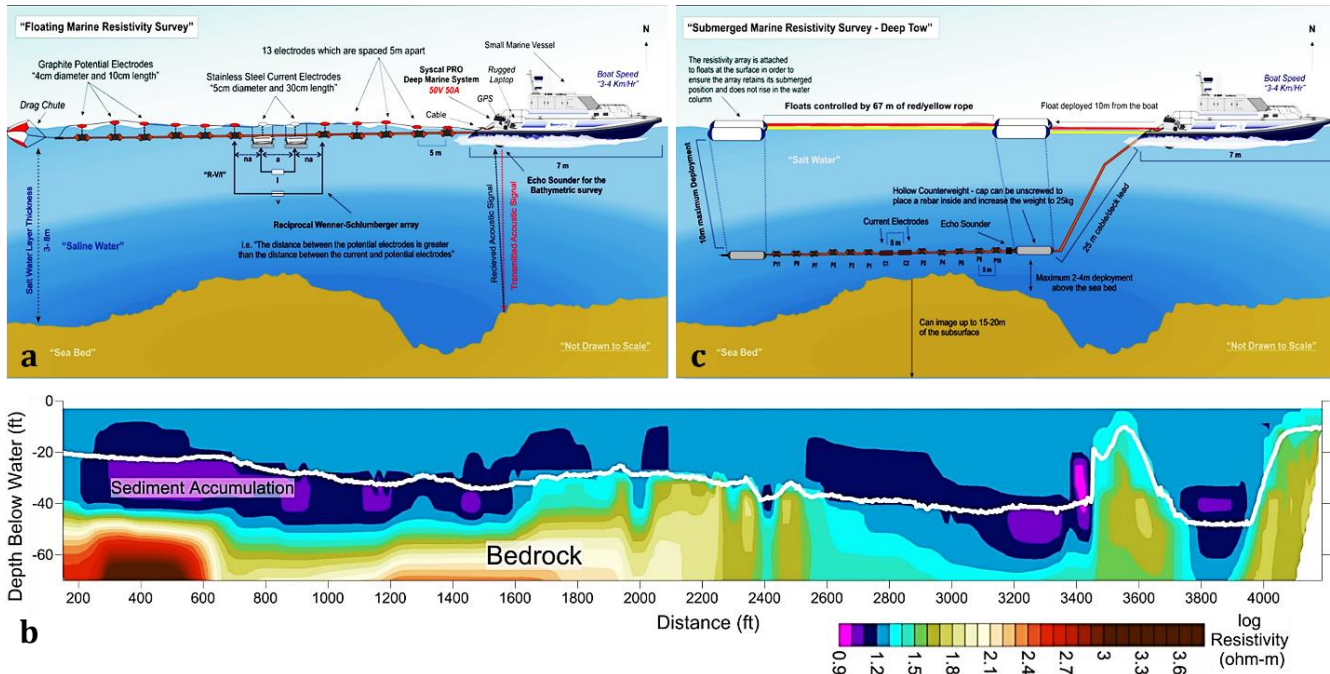


Fig. 12. Schematic diagrams of (a) the floating and (b) the submerged mobile underwater ERT survey system (adapted from Geomatrix Earth Science Ltd 2015). (c) A typical resistivity model section of Patagonia Lake, Arizona, derived from a CRP marine survey conducted using a floating-type marine resistivity system (adapted from HGI 2021).

4. Insights into seismic methods in surface–subsurface crustal prospecting

Seismic waves, originating from sources like earthquakes or explosions, propagate as elastic strain energy bundles. These waves, known as pulses, are fundamental to seismic surveys, spanning a wide frequency range (Kearey et al. 2002; Quigley 2006; Sujitapan et al. 2024; Akingboye 2024). Two primary types of seismic surveys exist, namely: reflection and refraction surveys. A typical example of a simple two-layered earth model is shown in Fig. 13. In reflection surveys, seismic waves' travel times are measured as they reflect off interfaces between subsurface layers of varying acoustic impedances, producing travel time curves (Fig. 13a) indicative of subsurface structures. Conversely, refraction surveys measure travel times of refracted waves (Fig. 13a–b) at geological boundaries, relying on differences in acoustic impedance (Moorkamp et al. 2013; Akingboye and Ognyuele 2019).

The reflection method is commonly used for deep crustal investigations, including mapping hydrocarbon-rich zones, and carbon sequestration areas, and understanding crustal dynamics in engineering projects, particularly in deep waters. Conversely, refraction is vital for near-surface crustal studies, ranging from shallow depths to hundreds of meters, with applications in hydrogeology, environmental assessments, and geoenvironmental engineering. Additionally, refraction models can correct seismic reflection models' structures. Data processing is crucial in seismic surveying to remove unwanted signals like direct waves and noise to enhance accuracy and interpretation. Recent advancements, such as integrated processing algorithms and advanced instrumentation like three-component seismometers, have revolutionized seismic surveying,

enabling higher resolution and improved imaging capabilities (Li et al. 2020; Yang et al. 2020; Arosio et al. 2023).

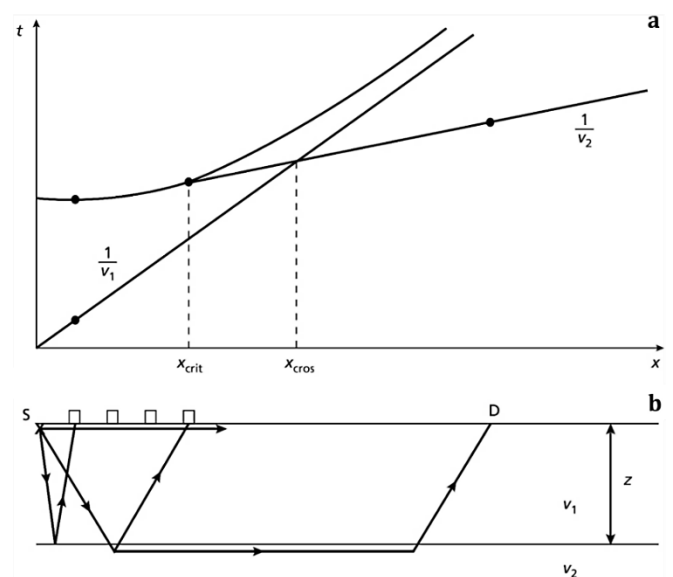


Fig. 13. (a) Schematic representation of a basic two-layered travel time curves model. (b) Illustration of a typical seismic acquisition setup depicting direct, reflected, and refracted seismic waves from a source (S) to a surface geophone detector (D) (adapted after Kearey et al., 2002). z , V_1 , V_2 , X_{crit} , and X_{cross} , denote depth of the layer, velocity of the first layer, velocity of the second layer, critical distance, and crossover distance, respectively. t is the intercept time. $1/V_1$ and $1/V_2$ are the gradients of the first and second layers, respectively.

The propagation velocities of seismic pulses are dictated by the elastic moduli and densities of the materials they traverse, typically falling into two categories: body and surface waves. Body waves, including compressional (P-waves) and shear waves (S-waves), propagate through the internal volume of solid elastic bodies. P-waves travel using compressional and dilatational uniaxial strains along the direction of wave travel, arriving at detectors before S-waves due to their higher velocities. S-waves, on the other hand, travel perpendicular to the wave direction through pure shear strain. Surface waves, such as Rayleigh and Love waves, travel along the boundary of an elastic solid. Generally, mantle rocks are denser and stronger than crustal rocks, resulting in faster travel times for both P-

and S-waves through the mantle compared to the crust (Telford et al. 1990; Earle 2019), as shown in Fig. 14. Seismic-wave velocities are influenced by the degree of compression within the rock, which increases significantly with depth. Also, the phase state of the rock affects seismic waves; any degree of melting slows their propagation. When the material is completely liquid, P-waves experience a dramatic decrease in speed, and S-waves are entirely halted (Earle 2019). This paper will primarily focus on seismic refraction velocity, specifically highlighting recent advancements in the SRT method for measuring, processing, and interpreting P-wave seismic refraction velocity (denoted as V_p).

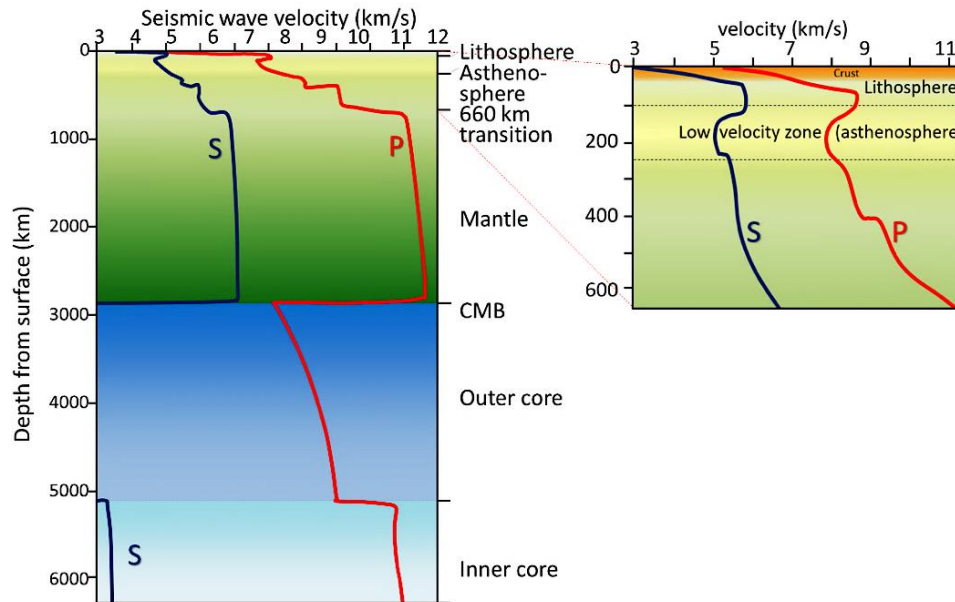


Fig. 14. Image of seismic velocity variations of P-wave (red) and S-wave (blue) deep within the earth and the projected magnification image of the upper 660 km depth (adapted from Earle 2019).

The mode of propagation of a P-wave in isotropic and homogeneous substances is always longitudinal. Therefore, V_p in a homogeneous isotropic medium is given as:

$$V_p = \sqrt{\frac{K + \frac{4}{3}\mu}{d}} = \sqrt{\frac{\lambda + 2\mu}{d}} \quad (18)$$

Where K represents the bulk modulus, which is the modulus of incompressibility; μ is the shear modulus (i.e., the rigidity modulus); d denotes the bulk density of the material through which the wave propagates, and λ is Lamé's constant. The bulk density d exhibits the least variation, controlled by parameters K and μ . The P-wave elastic modulus (M_p) of the propagating waves can be estimated as:

$$V_p = \frac{M_p}{d} \quad (19)$$

The velocity of the accompanying S-wave (V_s), is given as:

$$V_s = \sqrt{\frac{\mu}{d}} \quad (20)$$

Eqs. 18 and 20 suggest that V_p is faster in the same medium than V_s . Hence, the ratio of both waves as given in Eq. 21, is referred to as Poisson's ratio (φ) for the medium, illustrating the elastic (or deformation) properties of the propagated medium.

$$\frac{V_p}{V_s} = \sqrt{\frac{2(1-\varphi)}{1-2\varphi}} \quad (21)$$

4.1 Seismic refraction tomography

In recent years, seismic reflection tomography (SRT) has seen significant advancements aided by powerful computer-assisted technologies, transforming earthquake location determination and seismic body wave travel time analysis. Similar to conventional seismic refraction methods, SRT utilizes seismic energy from external energy sources (Jianliang et al. 2022; Akingboye 2023; Sujitapan et al. 2024). However, SRT benefits from advanced survey

loggers and geophones, such as the ABEM Terraloc Mk 8. Many researchers, so far, have developed various rock classification methods, including seismic velocity-based methods, graphical methods, and grading methods, to characterize lithologies based on their strengths (Hoek and Brown 1997; Barton 2006; Caterpillar Incorporation 2010; Akingboye and Bery 2022a; Akingboye 2023), e.g., Fig. 15. These methods draw from laboratory measurements as well as direct and indirect field measurements (Meju et al. 2003;

Gallardo and Meju 2007; Zeng et al. 2018; Akingboye and Bery 2023a). They often entail correlating measured seismic velocities with lithological properties, such as rippability, rock mass strength, or ratings, facilitating real-time data evaluation. To gain a comprehensive understanding of the range of velocity values associated with some common crustal materials and minerals, considering their wide-ranging velocities, as well as resistivity values, Table 1 provides pertinent information on these parameters.

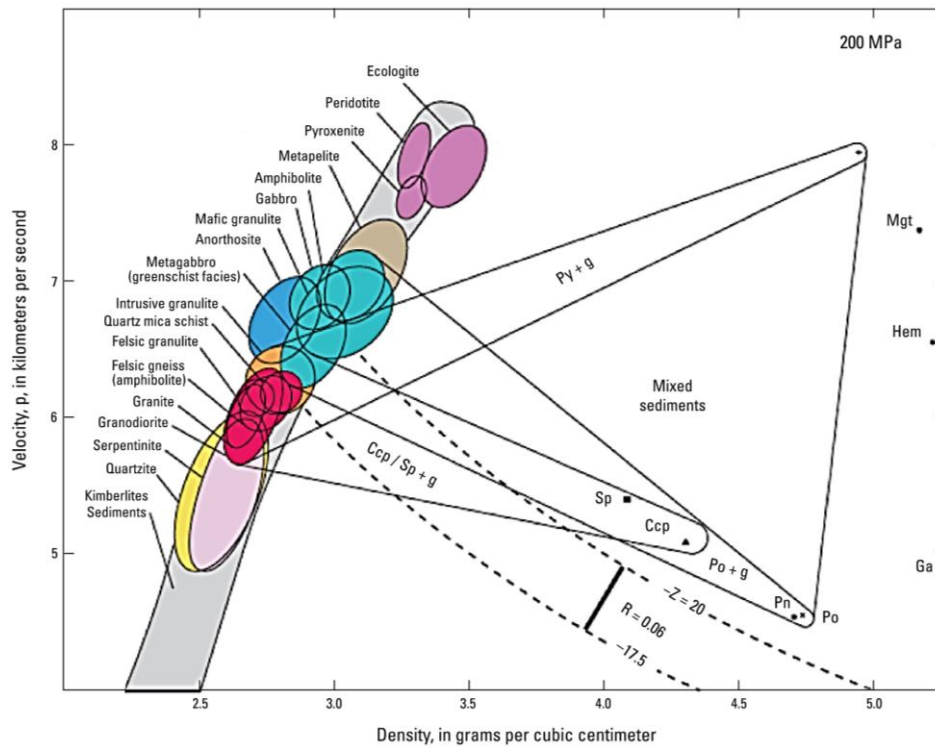


Fig. 15. Image of velocity (V_p) vs density values of various rock types and ore minerals. Lines of constant acoustic impedance (Z) are overlain within the field. Pyrite (Py), pentlandite (Pn), pyrrhotite (Po), chalcopyrite (Ccp), sphalerite (Sp), hematite (Hem), and magnetite (Mgt), with other fields for host rock-ore mixtures. Galena (Ga), with a velocity of 3.7 km/s and a density of 7.5 g/cm³, is off the scale. A reflection coefficient (R) of 0.06 is indicated to produce a strong reflection in contrasting lithologies (adapted from Morgan 2012).

Table 1. Typical electrical P- and S-wave velocity and resistivity values for some selected rocks and other materials.

Common Materials	P-wave velocity (m/s)	S-wave velocity (m/s)	Resistivity (Ωm)
Air	343	N/A	Infinity
Water	1400 – 1600	N/A	1430 – 1680
Ice	3400 – 3800	1700 – 1900	600 – 10 ⁷
Oil	1200 – 1250	N/A	>200
Clay	915 – 2750	1 – 300	1 – 150
Sand	200 – 2200	100 – 880	10 – 800
Coal	2200 – 2700	1000 – 1400	10 – 800
Gravel	500 – 1500	750 – 2250	600 – 10 ⁴
Conglomerate	10 – 800	----	2000 – 10 ⁴
Limestone	3500 – 6000	2000 – 3300	50 – 6000
Shales	1100 – 4500	200 – 800	20 – 2000
Sandstone	1400 – 4300	800 – 1800	10 – 5000
Dolomite	3500 – 6500	1900 – 3600	50 – 6000
Granite	4500 – 6000	2500 – 3300	300 (weathered) – 10 ⁶
Basalt	5000 – 6400	2400 – 2800	200 (weathered) – 10 ⁶
Gneiss	4400 – 5200	2700 – 3200	1000 – 3 × 10 ⁶

Researchers have also employed diverse analytical approaches, including qualitative and quantitative, statistical, machine learning, and deep learning techniques, to enhance these classification methods for better resolution of surface processes and hazards (Colombo et al. 2008a; Yang and Ma 2019; Li et al. 2020; Akingboye and Bery 2023a, b; Akingboye 2023). SRT data can predict lithology, pore fluids, and rock structures, making it valuable in groundwater exploration, mineral exploration, engineering site investigation, mining, and archaeology, across various spatial scales (Zakaria et al. 2021, 2022; Akingboye and Bery 2022b; Sujitapan et al. 2024; Akingboye 2024). It can resolve velocity gradients and lateral velocity variations within the subsurface. Challenges persist in accurately delineating lithologic units using SRT, including masked layers, hidden layers, and water infills. Overcoming these limitations may involve incorporating additional rock properties and refining filtering processes. Moreover, integrating SRT models with complementary methods such as borehole logs, rock quality

designation (RQD), and ERT, among others, holds promise for enhancing the reliability and completeness of subsurface geological information (Akingboye and Bery 2023a, b; Husainy et al. 2023).

4.2 SRT field survey operations and data acquisition techniques

SRT data acquisition techniques have evolved over the years, with advancements in instrumentation, data processing algorithms, and survey design strategies. Modern SRT surveys often incorporate advanced seismic sources and receivers, such as wireless systems, multichannel recorders, and three-component sensors, to improve data quality and efficiency (White 1989; Virieux and Operto 2009; Ronczka et al. 2018; Akingboye 2024). The acquisition of SRT data involves several key techniques aimed at maximizing data quality and coverage while minimizing costs and environmental impact. One crucial aspect is the selection and deployment of seismic sources and receivers, a typical example of this is the ABEM Terraloc Mk 8, as shown in Fig. 16a. Common sources include sledgehammers, explosive charges, and vibrators, each offering different advantages in terms of energy output, penetration depth, and safety considerations (Fang et al. 2020; Akingboye and Bery 2023a; Karşlı et al. 2024). Receivers, typically geophones (or hydrophones for marine surveys), are strategically placed along the survey line to record the arrival times of seismic waves.

Survey design plays a crucial role in optimizing data acquisition. Various geometries, such as common offset and common midpoint, can be employed to ensure adequate coverage and resolution (Quigley 2006; Akingboye and Ogunyele 2019). Additionally, the spacing between source and receiver points must be carefully chosen to balance resolution with survey cost and logistics. During data acquisition, seismic waves generated by the source propagate through the subsurface and are recorded by the receivers. The travel times of the seismic waves are measured accurately, typically using a seismograph or a data acquisition system connected to the receivers (Fig. 16b). Some essential measuring configuration settings to consider during surveys include the sampling interval, sampling number, and recording time. Additionally, it is crucial to check cables and geophones to ensure they are in the correct order and determine their sensitivities (Akingboye 2023). SRT surveys can be conducted on land (Sujitapan et al. 2024), in crossholes (boreholes) (Wong 1995), and in marine or river environments (Schlindwein et al. 2003), with typical schematic acquisition and layout diagrams shown in Fig. 16a–d.

Advancements in instrumentation and computing have led to the development of novel techniques for SRT data acquisition. Distributed acoustic sensing (DAS) using fiber-optic cables allows for continuous monitoring of seismic wave propagation along kilometers of cable length, enabling high-resolution imaging of subsurface structures with minimal surface disturbance (Virieux and Operto 2009; Fang et al. 2020). Additionally, the integration of SRT with other geophysical methods such as ERT, borehole logs, and ground-penetrating radar offers complementary information, enhancing the overall understanding of subsurface properties

(Martinho and Dionisio 2014; Husainy et al. 2023; Akingboye and Bery 2023b).

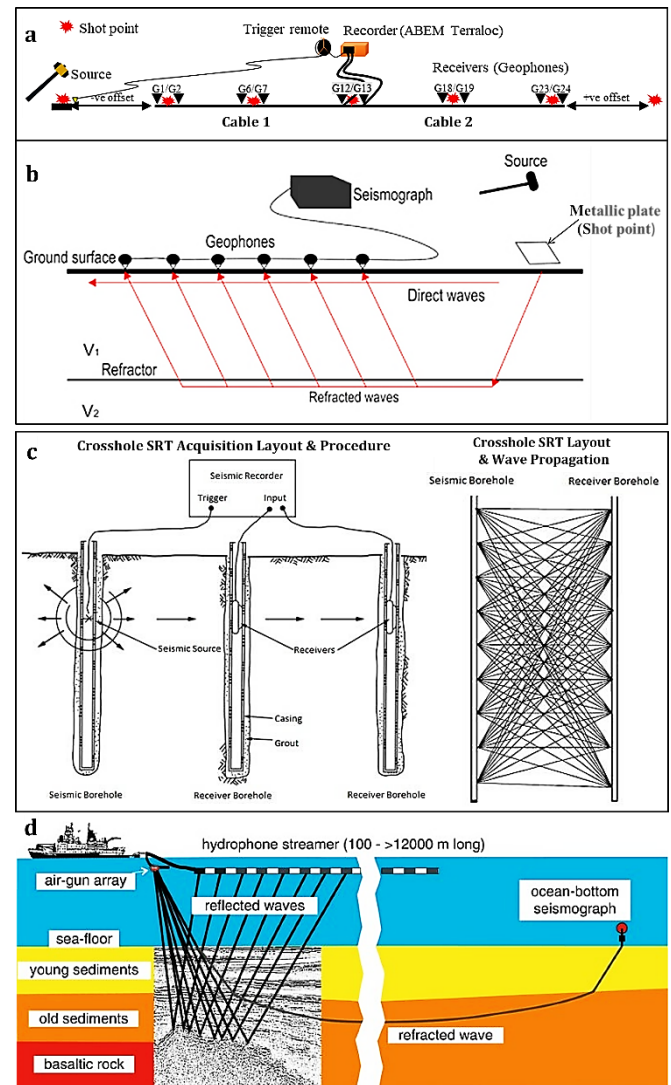


Fig. 16. (a) A typical layout for SRT data acquisition on land and (b) the progression of seismic waves for a two-layered subsurface model in an SRT ground survey. (c) Crosshole SRT survey type and (d) marine SRT survey procedures and acquisition layouts (adapted from Grootes 2016).

5. Electrical resistivity and seismic refraction tomographic data inversion and interpretation

5.1 Data processing, reduction, and inversion for ERT

ERT data processing and inversion techniques play pivotal roles in transforming raw field measurements into meaningful subsurface models. Initially, data processing involves preprocessing steps such as noise removal, quality control, and calibration to enhance the reliability of the collected data (Loke 2002; Abdullah et al. 2019; Loke et al. 2022). Subsequently, inversion algorithms are applied to reconstruct the subsurface resistivity distribution from the processed data. There are different inversion software (e.g., RES2DINV) and

they use various inversion methods, ranging from traditional approaches like smoothness-constrained or least-squares inversion to more advanced techniques such as Occam inversion, Tikhonov regularization, and Bayesian inversion (DeGroot-Hedlin and Constable 1990; Loke 2002; Bouchedda et al. 2017; Loke et al. 2022). These methods aim to find the most probable resistivity model that fits the observed data while satisfying constraints such as smoothness, geological consistency, and physical realism. An inversion program is a computational tool designed to automatically generate 2-D resistivity models of the subsurface. It processes datasets from resistivity imaging surveys, accommodating both conventional and non-conventional arrays, including uniform or non-uniform electrode spacing. This program is also versatile and capable of handling data from underwater and crosshole surveys (Dahlin 1996; Karaoulis et al. 2014; Abdullah et al. 2019).

During inversion, the inversion program employs either standard least-squares or robust least-squares approaches to minimize data misfits. Standard least-squares inversion iteratively adjusts model parameters to reduce the discrepancy between observed and predicted data. However, it may be sensitive to outliers and noise, resulting in inaccurate results. Robust least-squares inversion addresses this by incorporating robust statistical measures that reduce the influence of outliers and noise in the data (Loke 2002). It achieves this by assigning lower weights to data points with larger residuals, ensuring a more reliable and stable inversion outcome, especially in the presence of noisy measurements or anomalous data. Both methods have their advantages and limitations. While standard least-squares inversion is computationally efficient and straightforward to implement, it may produce biased results in the presence of outliers. Robust least-squares inversion, although more robust to outliers, may require more computational resources and careful parameter tuning (Loke 2002; Akingboye et al. 2022). In practice, the choice between standard and robust least-squares inversion depends on the specific characteristics of the ERT dataset, such as noise levels, data quality, and the presence of outliers. The distinction between standard and robust least-squares inversions lies in their data misfit functions, with the former and latter incorporating convergence limits represented by RMS error and absolute error, respectively.

Furthermore, during inversion, the mathematical inverse problem aims to determine the subsurface resistivity distribution from apparent resistivity measurements, generating an inverted model that best matches the field data through a predefined number of iterations for convergence. The subsurface is discretized into numerous rectangular cells during the inversion, with the resistivities of these cells determined by the inversion algorithm (Loke 2002). However, the resulting resistivities may not always accurately represent the true subsurface conditions due to simplifications and assumptions inherent in the cell-based inversion approach. The linearized smoothness-constrained least-squares optimization method handling this is described by DeGroot-Hedlin and Constable (1990) and Dahlin and Loke (2018), relating model parameters (r) to data misfit (g) as outlined in Eq. 22.

$$[J_i^T R_d J_i + \lambda_i W^T R_m W] \Delta r_i = J_i^T R_d g_i - \lambda_i W^T R_m W r_{i-1} \quad (22)$$

J is the Jacobian matrix, representing apparent resistivity measurements relative to model resistivity values; W is the roughness filter; and λ signifies the damping factor. The data misfit vector, g , reflects the variance between measured and calculated resistivity values. Δr_i denotes the necessary change in model parameters for iterations aimed at minimizing data misfits. r_{i-1} is the resistivity model from the previous iteration, with R_d and R_m representing the weighting matrices used in the L_2 -norm standard or robust inversion methods.

According to Cheng et al. (2019) and Akingboye and Bery (2021a), accurately assessing the root mean square error (RMSE) is crucial for quantitatively evaluating the soil-rock model. While synthetic models typically lack measurement errors, real field models are prone to such errors, which can significantly impact computed resistivity models. The RMSE, indicating the spatial variability of resistivity values, is computed as the disparity between measured and calculated resistivity values, following Eq. 23 (Loke 2002).

$$RMSE = \sqrt{\frac{1}{n^2} \sum_{i=1}^n \left(\frac{\rho_{mi} - \rho_{ci}}{\rho_{ci}} \right)^2} \quad (23)$$

Where n is the number of measurement points, ρ_{mi} and ρ_{ci} are the measured and calculated resistivity and i^{th} data point.

Recent advancements in ERT data processing include the integration of machine learning and artificial intelligence techniques, which offer the potential to improve inversion accuracy and efficiency. Deep learning algorithms, such as convolutional neural networks (CNNs), Monte Carlo, generative adversarial networks (GANs), etc., have shown promising results in automating the inversion process and handling complex geological structures (Liu et al. 2020; Aleardi et al. 2021; Hiskiawan et al. 2023). Moreover, the development of parallel and distributed computing architectures has accelerated the computation speed of inversion algorithms, enabling the processing of large-scale ERT datasets in a reasonable timeframe. Additionally, the incorporation of advanced regularization techniques and prior information derived from complementary geophysical methods or geological knowledge has enhanced the robustness and stability of inversion results (Liu et al. 2020; Abdullah et al. 2022). Despite these advancements, challenges persist, including the accurate modeling of complex geological structures, handling non-uniqueness and uncertainty in inversion solutions, and efficiently integrating multi-scale and multi-physics data. Addressing these issues requires interdisciplinary collaboration between geophysicists, mathematicians, computer scientists, and domain experts to develop novel solutions and push the boundaries of ERT data processing and inversion techniques (Loke et al. 2022).

5.2 Data processing, reduction, and inversion for SRT

SRT data processing entails several essential steps to derive meaningful subsurface insights from raw seismic data. Initially, the raw data undergo preprocessing, including filtering, noise removal, and time–distance corrections, to optimize signal quality (Quigley 2006; Akingboye 2024). Subsequently, traveltime tomography algorithms are utilized to transform the arrival time data into a

velocity model of the subsurface. Common inversion methods encompass first-arrival traveltimes tomography, waveform tomography, and full-waveform inversion, each offering distinct trade-offs between computational complexity and model resolution (Virieux and Operto 2009; Yang and Ma 2019; Fang et al. 2020; Akingboye and Bery 2023a). Filtering techniques are employed to enhance the signal-to-noise ratio and suppress unwanted noise components. After preprocessing, arrival time picking is conducted to identify first-arrival seismic waves, crucial for velocity analysis.

Inversions, central to SRT data processing, aim to reconstruct subsurface velocity models from observed arrival times. Various inversion algorithms, including tomographic methods and iterative solvers, iteratively optimize model parameters (Côte et al. 2020). While conventional seismic refraction relies on generalized geometry to segment subsurface models into continuous layers of constant velocity, SRT adopts a grid-based approach, dividing the model into numerous small grid cells or nodes for improved representation of subsurface materials (Akingboye and Ogunyele 2019). Through iterative ray tracing and comparison of field data with calculated travel times, the subsurface velocity model is refined grid-by-grid until convergence is attained (Salleh et al. 2021; Akingboye 2023). Regularization techniques are frequently employed to mitigate the ill-posed nature of the inverse problem and ensure the stability and uniqueness of solutions. The final stage involves generating the subsurface velocity models and visualizations. Various software packages facilitate this task, enabling geoscientists to interpret data in 2- or 3-D and generate cross-sectional profiles of the subsurface. Currently, 4-D SRT modeling interpretation are evolving as an efficient approach for monitoring subsurface conditions, akin to TLERT (Côte et al. 2020; Rosa et al. 2020).

Case studies across diverse geological settings showcase the efficacy of SRT data processing and inversions in characterizing subsurface structures, detecting geological anomalies, and delineating hydrocarbon reservoirs (Ronczka et al. 2018; Côte et al. 2020; Rosa et al. 2020; Adeola et al. 2022; Sujitapan et al. 2024; Akingboye 2024). Recent advancements in computational techniques, including parallel computing, machine learning, and deep learning algorithms, have accelerated the processing speed and improved the accuracy of SRT inversions (Yang and Ma 2019; Côte et al. 2020; Liu et al. 2021). These methods offer the potential to enhance the speed and robustness of SRT inversions, enabling more accurate subsurface imaging in diverse geological settings. Challenges persist in SRT data processing, such as handling noisy data, addressing non-uniqueness in inverse solutions, and incorporating prior geological information into the inversion process. Future research directions may focus on developing advanced inversion algorithms capable of handling large-scale datasets, integrating multi-physics data for improved subsurface imaging, and enhancing uncertainty quantification methods to provide reliable estimates of model uncertainties.

5.3 Interpretation: machine learning and deep learning prospects in ERT and SRT

With increasing complexity in resistivity and seismic exploration, accurately estimating geophysical responses and related geological parameters becomes more demanding. Various methods have emerged to improve lithological model interpretation. In recent years, advancements in machine learning (ML) and deep learning algorithms have revolutionized ERT and SRT inversion models (Yang and Ma 2019; Oware et al. 2019; Liu et al. 2020; Côte et al. 2020). ML, including supervised and unsupervised learning, and deep learning algorithms have become transformative tools in ERT and SRT analysis. Algorithms such as Artificial Neural Networks (ANNs), Convolutional Neural Networks (CNNs), Monte Carlo, Random Forest, Generative Adversarial Networks (GANs), and Bayesian models have shown promise in interpreting complex geological structures (Oware et al. 2019; Li et al. 2020; Liu et al. 2020; Aleardi et al. 2021; Hiskiawan et al. 2023). They process seismic traveltimes data, infer subsurface velocity structures, identify seismic phases, and delineate geological interfaces. These advanced algorithms uncover hidden patterns in large and complex datasets, enhancing the interpretation of surface–subsurface geological features in large-scale ERT datasets within a reasonable timeframe. They prove effective in studying various Earth surface processes and hazards, including landslide triggers, subsurface dissolution, groundwater migration paths, and soil and rock differentiation (Côte et al. 2020; Dimech et al. 2022; Xixi et al. 2023; Akingboye and Bery 2023a; Sujitapan et al. 2024). Through ML and deep learning, researchers gain deeper insights into the Earth's subsurface, facilitating better understanding and management of geological resources and hazards.

Unsupervised machine learning clustering algorithms, including K-means, hierarchical density-based, and fuzzy-based clustering, offer promising avenues for identifying structural patterns within geological formations, thus aiding in the interpretation of ERT and SRT data (Di Giuseppe et al. 2014; Bernardinetti and Bruno 2019; Delforge et al. 2021). These algorithms segment subsurface data into distinct clusters, facilitating the identification of lithological boundaries and geological features. Supervised machine learning algorithms, such as statistical regressions, establish quantitative relationships between resistivity and velocity values with geological parameters, enabling the estimation of subsurface properties like lithology, porosity, and fluid content (Gallardo and Meju 2007; Zeng et al. 2018; Akingboye and Bery 2023a). Additionally, supervised neural networks can predict subsurface resistivity and velocity profiles, capturing complex variations attributed to the subsurface and facilitating the characterization of geological units, fault zones, and stratigraphic boundaries (Latrach et al. 2023).

Recent research has explored the integration of deep learning techniques into ERT and SRT data processing. For instance, Liu et al. (2020) employed deep learning, utilizing CNNs based on U-Net architecture, on synthetic and real-time field datasets to develop ERSInvNet for qualitative and quantitative mapping of resistivity-related geological structures. The models, trained end-to-end, demonstrated real-time inference during testing and incorporated

depth weighting functions and smooth constraints into the loss function to improve inversion accuracy for deep regions and suppress false anomalies. Similarly, Liu et al. (2021) proposed a full waveform inversion approach for velocity (Vp) model inversion via deep learning, aiming to construct a realistic structural model for mapping dense layers, faults, and salt bodies. This concept of seismic full waveform inversion was first proposed by Lailly and Bednar (1983) and Tarantola (1984), utilizing the generalized least-squares criterion to provide a comprehensive framework for seismic velocity inversion. Moreover, Li et al. (2020) introduced a novel deep neural networks (DNNs) architecture, SeisInvNets, to address the challenge of transforming time-series data into spatial images in the field of seismic exploration. SeisInvNets reconstructs the velocity model directly from seismic data iteratively, tackling the ill-posed inversion problem caused by poor nonlinear mapping and strong non-uniqueness. Evaluations on synthesized data demonstrate consistent improvements over baselines, highlighting promising performance across various evaluation metrics. However, generalizing deep-learning-based inversion methods to real data remains challenging, and incorporating physics-based constraints may offer a potential solution to enhance their applicability and robustness.

Furthermore, in recent years, significant efforts have been directed toward subsurface characterization across various geological terrains, aiming to establish relationships between seismic velocity and electrical resistivity. Supervised statistical methods have been employed for joint parameter inversion of velocity–resistivity models (Opfer 2003; Colombo et al. 2008b, a; Muñoz et al. 2010). The experiment conducted by Weatherby and Faust (1935), which highlighted the increase in velocity values with geological age and depths, sparked interest in establishing correlation links between velocity and resistivity. Given the scarcity of continuous velocity logs and the prevalence of short-normal logs at that time, geoscientists began seeking additional information from borehole logs. Acheson (1963) provided an empirical relation correlating velocity to depth using a set of lithology-dependent constants, which was further modified by Delaplanche et al. (1963) for improved flexibility. Expanding on this approach, Kim (1964) established a scale function relation connecting pseudo-transit times with transit time in solid and apparent resistivity (ρ_a). Rudman et al. (1975) finally demonstrated that conventional resistivity logs could be utilized to generate pseudo-velocity logs, also known as seismic velocity or transit time logs. These empirical relationships have enhanced our understanding of resistivity and velocity, offering broader applicability across various geological settings. In this context, Table 2 presents recent emerging techniques for resistivity and Vp interpretation based on statistical optimization. The table outlines the terrains (soil or rock) where studies were conducted, the methodological approaches used, and the accuracy assessments performed to validate their results, providing valuable insights into the advancement of subsurface characterization techniques.

Despite the benefits offered by supervised and unsupervised ML, including deep learning algorithms, both ERT and SRT still encounter challenges in accurately predicting subsurface characteristics and integrating domain-specific knowledge, particularly in the fields of physics and engineering (Liu et al. 2020, 2021; Akingboye and Bery

2023a). Notably, one of the primary hurdles in geosciences pertains to the characterization of subsurface lithology, given its intricate and diverse compositions (Gallardo and Meju 2011). However, ongoing research endeavors are dedicated to overcoming these challenges by developing hybrid ML models that amalgamate domain knowledge with data- and image-driven approaches, thereby facilitating more precise and reliable interpretations of the subsurface.

Given the comprehensive reviews provided above, there is a clear necessity to develop a systematic methodological framework for efficiently modeling ERT and SRT data, spanning from data acquisition to establishing robust relationships between resistivity and Vp. Such a framework would enable rapid and detailed estimation of subsurface properties like lithology, porosity, and fluid content based on the statistical relationships. Hence, a proposed framework, outlined in Fig. 17, builds upon the methodologies employed by Akingboye and Bery (2023a). Fig. 17a presents the overarching methodology for establishing velocity–resistivity relationships. This figure is segregated into Figs. 17b and 18, where Fig. 17b focuses on simultaneous data inversions, while Fig. 18 details the procedures for interface modeling of resistivity and Vp models via unsupervised and supervised ML techniques (K-means clustering and regression modeling). Additionally, Fig. 18 includes the accuracy assessment of the resulting empirical relation and the derived predictive model. The utilization of statistical validation parameters, such as histograms, R^2 values, normal P-P plots, scatter plots, Durbin-Watson statistics, p-values, and others, marks a significant advancement for this approach. Despite the site-specific nature of empirical relationships, this approach offers a cost-effective and rapid solution, bridging data acquisition gaps across diverse geological terrains. The proposed methodological frameworks find practical applications in the presented case studies.

5.4 Interpretation: cross-plot method for resistivity and velocity modeling

Another known approach for interpretive modeling of velocities and resistivity datasets is cross-plot analysis. Cross-plot analysis is a well-established approach for interpretive modeling of velocity and resistivity datasets, widely employed in various fields of geosciences, such as the oil and gas industry (Anyiam et al. 2018) and engineering studies, particularly in landslide assessment (Zakaria et al. 2021; Sujitapan et al. 2024). This method involves plotting resistivity against P-wave velocity (Vp) or S-wave velocity (Vs), Fig. 19, to delineate soil types and the vulnerability of the subsurface lithological condition based on the plots' quadrants (Hayashi and Konishi 2010). An intrusive sampling of data from boreholes is often used to calibrate and validate geophysical data for cross-plotting, enhancing accuracy in landslide assessment and the development of mitigation strategies. For instance, in Fig. 19a, the cross-plot of resistivity and Vp in the Q1 section identifies lithological materials prone to sliding, especially in landslide-prone areas. Hayashi and Konishi (2010) demonstrated the effectiveness of cross-plot analysis in levee assessment. They posited that loose and sandy levees pose greater risks than tight and clayey levees, e.g., Fig. 19b. Building upon this work, Sujitapan et al. (2024) employed a cross-plot analysis

Exploring electrical and seismic refraction methods: theories to emerging prospects

method to enhance the resolution of subsurface structures using combined resistivity and Vp datasets, particularly for landslide detection in Thungsong district, Nakhon Si Thammarat, Thailand. Their 2-D cross-plot model revealed detailed images of subsurface

conditions, highlighting areas with low Vp and low resistivity as potential sliding materials. Similarly, [Zakaria et al. \(2021\)](#) utilized cross-plot modeling of Vp and resistivity data in Ulu Yam, eastern Kuala Lumpur, Malaysia, to study landslide activities.

Table 2. Summary of selected recent analytical modeling and interpretation techniques (including ML) used for Vp and resistivity (DC, ERT, or magnetotelluric datasets) analysis.

Sample (or terrain)	Methodology	Proposed statistical/ empirical relationships	Accuracy assessment	References
Mountsorrel granodiorite terrain (characterized by a buried hillside of highly fractured granodiorite rock mass successively overlain by a heterogeneous mudstone and glacial drift)	Conjugate gradient inversion and statistics (regression)	$\text{Log}_{10} \rho = 3.88 \text{Log}_{10} Vp - 11$ (for consolidated rocks at >3 m depth) $\text{Log}_{10} \rho = -3.88 \text{Log}_{10} Vp + 13$ (unconsolidated soil/drift deposits) $\text{Log}_{10} \rho_a = 3.88 \text{Log}_{10} Vp + 3.88 \text{Log}_{10} 11$ (solid grains with Vp less than pore fluid)	Porosity was considered a relevant factor based on the 3 rd relation	(Meju et al. 2003)
	Cross gradient function based on Lagrange multiplier	-----	----	(Gallardo and Meju 2003)
	Joint inversion formulation using forward and derivative approaches	-----	RMSE (data misfit) with convergence <2%	(Gallardo 2004 ; Gallardo and Meju 2007)
Sub-basalt (Ghawar field, Saudi Arabia)	Simultaneous joint inversion and statistics	$\text{Log} \rho = 0.000441244(Vp) - 3.33559$	3-D generalized cross-gradient function	(Colombo et al. 2008b)
	Cross-plot regression function	$\rho = aV_p^{0.25}$ (the derived relation agrees with the provided Gardner's relation but with a slight coefficient change)	Confirmation of Gardner's relation	(Colombo and Kehe 2010)
	Joint wavefield inversion and Cross-plot regression function	$\rho = (3 \times 10^{-17})V_p^{5.0613}$	$R^2 = 0.9127$	(Colombo et al. 2020)
Groß Schönebeck Geothermal Field in Berlin, Germany	Gaussian probability density function	$f(x) = \sum_j^n \frac{a_j}{2\pi[\sum_j]^{1/2}} \exp -\frac{1}{2}[(x - \varphi_j)^T \sum_j^{-1} (x - \varphi_j)]$	Utilized the codes provided by Becken and Burkhardt (2004)	(Muñoz et al. 2010)
Swelling mudstone (Yanji Basin, NE China)	Regression statistics	$\rho = 133.07 - 0.074Vp$ (wetting–drying cycles) $\rho = 13.525 + 0.023Vp$ (freezing–thawing cycles) $\rho = 27.912 + 0.012Vp$ (wetting–drying–freezing–thawing cycles)	$R^2 = 0.816$ $R^2 = 0.752$ $R^2 = 0.641$	(Zeng et al. 2018)
Granitic terrain (Penang Island, Malaysia)	Complex collocated geotomographic and supervised statistical modeling	$Vp = 0.4865(\rho) + 168.764$ (Generalized relation) $Vp_{RS} = 0.1927(\rho_{RS}) + 363.32$ (residual soil unit) $Vp_{W/WF} = 0.4713(\rho_{W/WF}) + 249.28$ (weathered/fractured unit) $Vp_{I/FB} = 0.2506(\rho_{I/FB}) + 1193.9$ (integral/fresh granitic bedrock)	$R^2 = 0.8517$ $R^2 = 0.99$ $R^2 = 0.98$ $R^2 = 0.99$ Other statistical charts	(Akingboye and Bery 2023a)
Sedimentary terrain (Kabota-Tawau area of Sabah, Malaysia)	Interpolating P-wave velocity and resistivity models and machine learning (K-means clustering and supervised statistical modeling)	$\rho = 0.053(Vp) - 20.31$ (Generalized Vp and resistivity relation for surface–subsurface lithological prediction and modeling)	$R^2 = 0.868$ Different statistical and cluster density plots	(Dick et al. 2024)

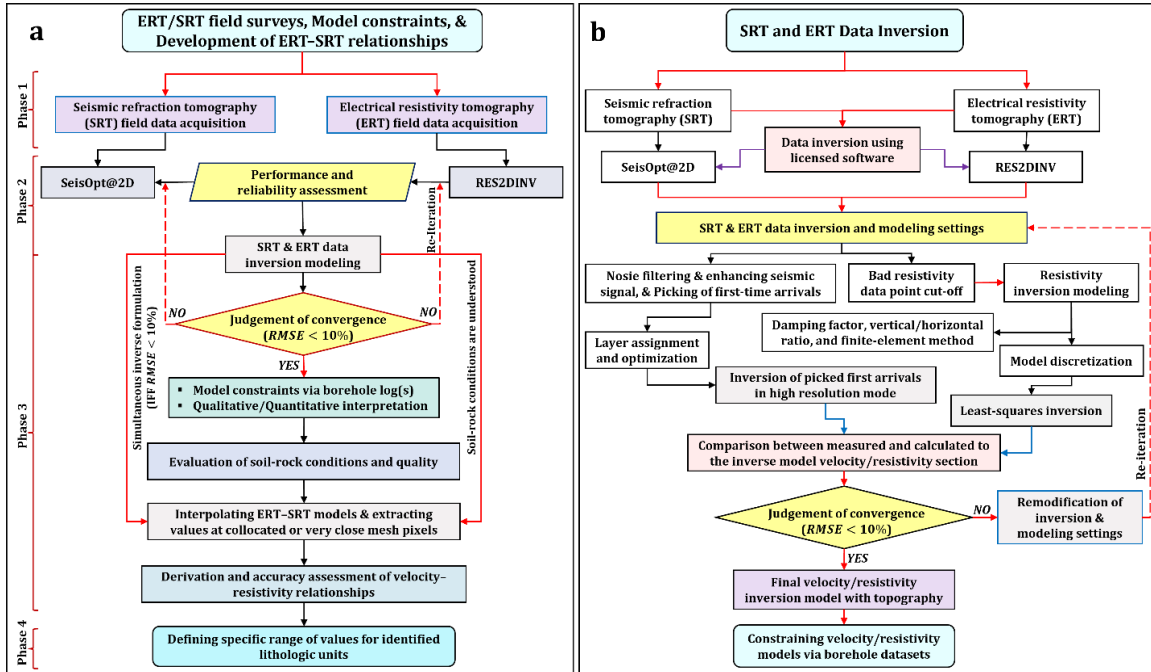


Fig. 17. (a) Proposed methodological framework for acquisition to supervised statistical modeling of ERT-SRT datasets. (b) Simultaneous processing and inversion of ERT and SRT datasets.

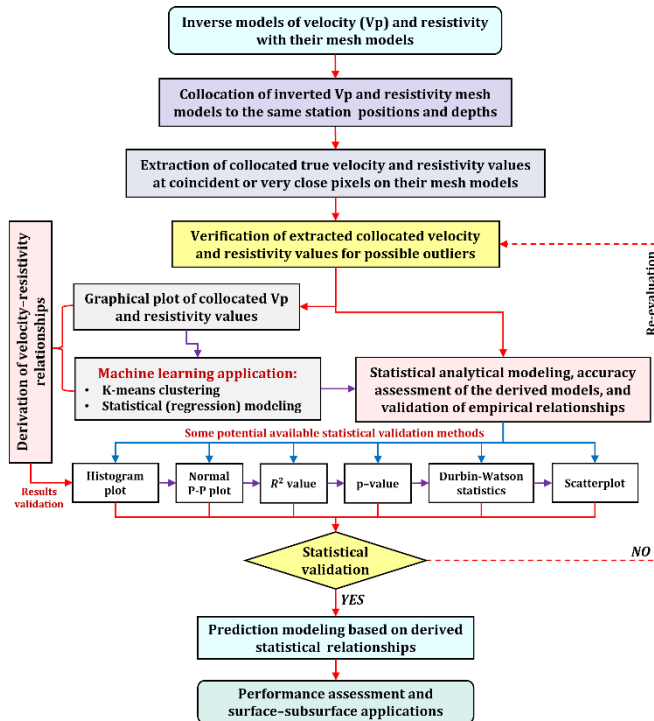


Fig. 18. Proposed framework architecture for supervised statistical modeling (including K-means clustering) of interfaced resistivity and velocity datasets.

6. Case studies

The data acquisition and inversion methods employed for both ERT and SRT datasets in the case studies are the same as those previously outlined. For ERT, field data was gathered using ABEM

SAS Terrameter 4000 and ES 64-10C instruments. Subsequently, resistivity datasets, along with topographical information, were processed and inverted using RES2DINV software. Both standard and robust least-squares inversion techniques were utilized based on data noise levels. The finite-element method with L_2 -norm constraint parameters was employed to minimize discrepancies between measured and calculated apparent resistivity values. A damping factor of 0.05, with a minimum value of 0.01, was applied to enhance the models' resolution, with RMS or absolute errors of the inverse models converging below 10% within 5 to 7 iterations. However, for noisy datasets, the RMSE statistics cut-off approach was adopted.

On the other hand, SRT data collection utilized ABEM Terraloc Mk 8 equipment, complemented by a 12-pound hammer, a striker metal plate, and a 24-channel geophone setup at 14 Hz. Specific instrument settings included a sampling interval of 100, a sample number of 2048, and a record time of 204.8 ms. Multiple shots, ranging from 5 to 7, were executed at shot points to ensure high-resolution models with increased depth penetration. Furthermore, a greater number of shots were deployed at offsets, varying between 10 m and 12 m, to achieve deeper probing depths. Each SRT line recorded a minimum of 360 seismic traces from 7 to 15 shot points, depending on the traverse length. Following field measurements, data processing involved managing observed, recorded, and source files, along with distances of shot points relative to station elevations. Weak signals were amplified through auto-gain control, and first arrivals were picked using FirstPix. Subsequently, SeisOpt@2D software (Optim Incorporation 2006), based on nonlinear optimization techniques, was employed to process and invert first arrival travel times in high-resolution mode. This involved utilizing the refraction inversion and optimization technique (RIOT), which

employs a fast finite-difference method to solve the eikonal equation for forward modeling and Vp dataset inversion. The resulting ERT

and SRT inversion models were constrained by lithologic units and their depths obtained from borehole logs.

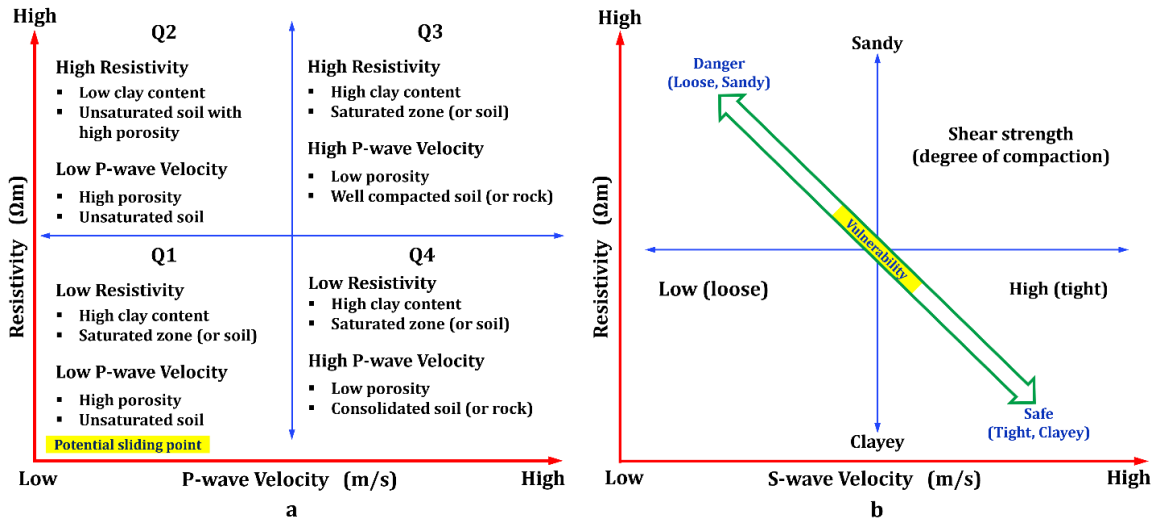


Fig. 19. Schematic cross-plots of resistivity against (a) P-wave velocity (Vp) and (b) S-wave velocity (Vs) for interpretation of soil-rock conditions (modified after Hayashi and Konishi 2010). The potential vulnerability of a levee channel is also shown by the Vs plot.

6.1 Electrodes’ performance in surface–subsurface characterization

The study sites (Fig. 20) are situated on Penang Island, Malaysia, located in the Malacca Strait, northwest of Peninsular Malaysia, and are characterized by the Gula, Beruas, and Simpang Formations (Hassan 1990; Ong 1993), Fig. 20a. Penang Island predominantly consists of igneous rock, primarily granite, similar to other Malaysian granitoids. Two Granitic Plutons: the North Penang Pluton (NPP) and

the South Penang Pluton (SPP), underlie the island, classified based on the percentage of alkali to total feldspar content (Ong 1993). NPP comprises the Tanjung Bungah, Paya Terubong, Batu Ferringhi groups, and the Muka Head microgranite, with ages ranging from the Early Permian to the Late Carboniferous period. Conversely, the SPP is distinguished by the presence of the Sungai Ara and Batu Maung granites (Ong 1993; Ahmad et al. 2006). The detailed geology of the area has been thoroughly discussed in many literatures.

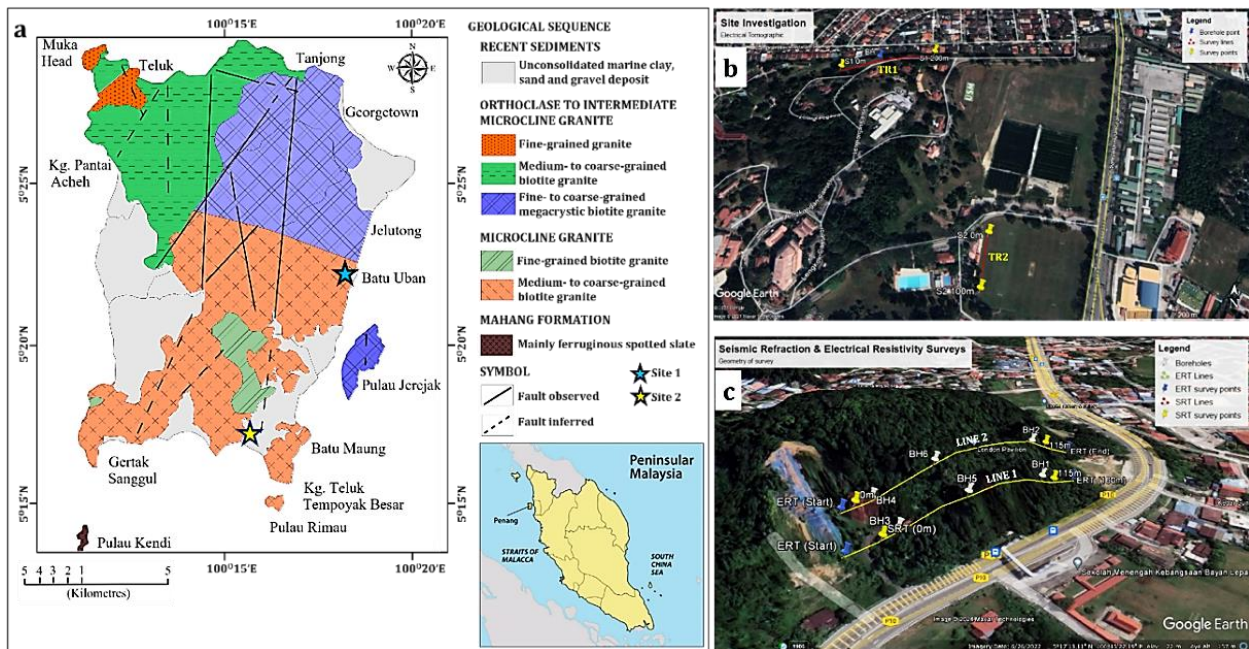


Fig. 20. (a) Penang Island’s geological map (modified after Ong 1993), showing case study Sites 1 and 2. Aerial geophysical data acquisition maps of (b) Site 1 (at USM) and (c) Site 2 at Batu Maung area of Penang Island, Malaysia.

Exploring electrical and seismic refraction methods: theories to emerging prospects

To evaluate the performance of copper and stainless-steel electrodes and compare their results and subsurface model resolutions, two sections within Universiti Sains Malaysia (USM), designated as Site 1, were investigated (Fig. 20b). Traverse TR1 spanned 200 m in length with 5 m electrode spacing, while TR2 measured 100 m long with a spacing of 2.5 m (Fig. 20b). Both sites utilized the same number of electrodes, with a total of 41 copper and stainless-steel electrodes deployed simultaneously. The Wenner-Schlumberger array was employed for conducting ERT surveys at both Sites 1 and 2.

After filtering errors associated with cultural/self-potential noise, the results indicated that the resistivity and chargeability models for stainless-steel electrode type with 5 m spacing had higher RMSEs, 7.2% and 3.5% (TR1; Fig. 21a–b), respectively, compared to those generated for the copper electrode type resistivity and chargeability models with 7.0% and 1.4% for similar spacing (Fig. 21c–d). This is indicative of the higher conductivity of copper compared to stainless-steel electrodes (LaBrecque and Daily 2008; Akingboye and Bery 2021a). This property is reflected in their model resolutions with depths. The stainless-steel and copper electrode-type resistivity models showed similar lithological features at the uppermost section, with depths below 6 m. However, they exhibited varying responses with deeper depths. Fig. 21c offers more reliable geological conditions than its counterpart in Fig. 21a, especially at the central section with weathered granitic bedrock (as indicated by Fig. 21e)

between the 80 m and 110 m station positions. This section was clearly depicted on the copper chargeability model (Fig. 21d) to be characterized by low to high chargeability, which was seen to have completely low chargeability (<3 msec) in Fig. 21b. Both resistivity and chargeability models for these two electrode types accurately mapped the sandy silt between station distances of 110 m and 160 m, with very high chargeability of >10 msec. However, Fig. 21d indicates a possible deep-weathered/fractured section at the 125 m station point with water saturation or sand due to the very low chargeability.

The results of the resistivity and chargeability models for the stainless-steel and copper electrode types along TR2, with 2.5 m spacing (Fig. 22a–d), had almost comparable RMSEs, except for the copper electrode type chargeability model with a lower RMSE of 0.18% (Fig. 22d). Their subsurface model resolutions are completely similar, but a pocket of moderate chargeability of 2–3 msec is recorded between 70 m and 80 m (Fig. 22b). Based on the observed results at this site, it indicates that the shallow probing depth and a short profile enhance faster electric current injection and increase electrode sensitivity, allowing high model resolution and geologic structural mapping (Binley and Kemna 2005; Akingboye and Bery 2021b). These results have demonstrated the reliability of stainless-steel and copper electrodes in subsurface imaging, particularly in tropical granitic terrain.

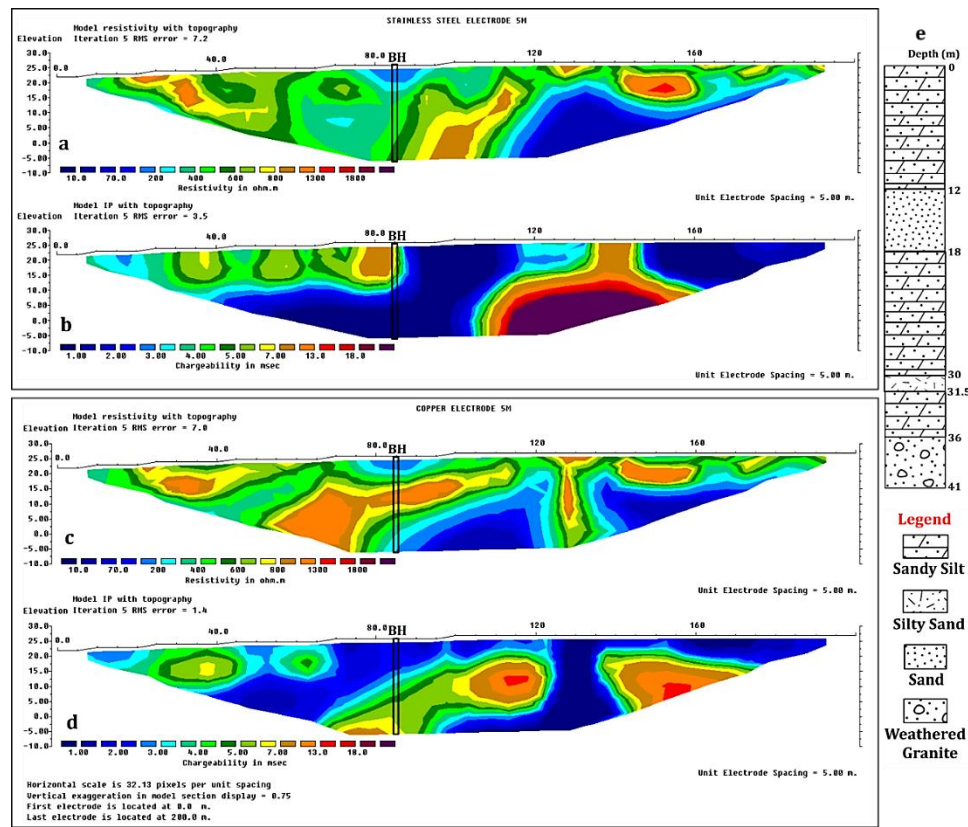


Fig. 21. ERT and IP inversion models of TR1 generated for (a–b) stainless-steel electrode and (c–d) copper electrode types, with 5 m electrode spacing. (e) Borehole lithological log at TR1.

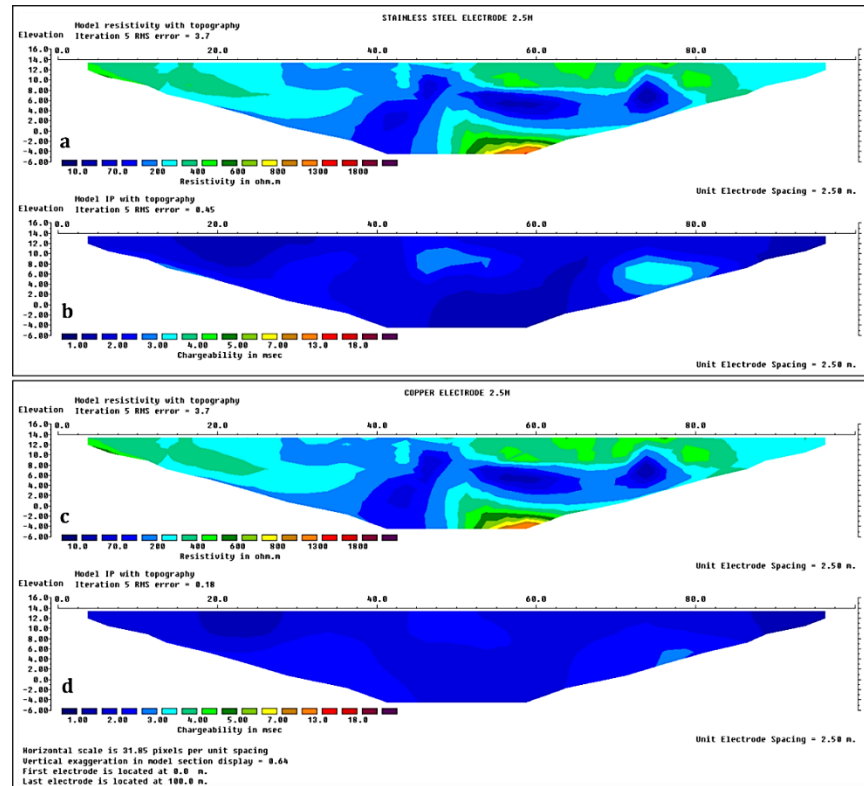


Fig. 22. ERT and IP inversion models of TR2 generated for (a–b) stainless-steel electrode and (c–d) copper electrode types, with 2.5 m electrode spacing.

6.2 Modeling surface–subsurface conditions: a case study of Southern Penang Island, Malaysia

This site, situated in Batu Maung within the study area of Penang Island, Malaysia, is designated as Site 2. Here, this study delves into the subsurface lithological differentiation of the southern part of this tropical granite terrain using machine learning (ML), employing both unsupervised (K-means clustering) and supervised statistical modeling of interfaced velocity–resistivity datasets. To assess the distributions of V_p and resistivity across surface–subsurface lithologic units, two geophysical lines were established in roughly SW–NE directions (Fig. 20c), with each SRT line covering a distance of 115 m and 5 m spacing. Conversely, the ERT utilized a 4.0 m electrode spacing for a traverse length of 160 m each. Additionally, six boreholes (BH1–BH6) were drilled to provide constraints on the subsurface lithologic units, aiding in achieving a detailed interpretation. Subsequently, the resulting field datasets underwent processing using the aforementioned inversion procedures.

Based on the generated inversion models and borehole logs (Fig. 23a–e), three distinct lithologic units were inferred: clayey to sandy topsoil, weathered/fractured unit, and the integral/fresh bedrock. Subsequently, mesh models for the SRT and ERT lines were generated from their inversion models (Fig. 23a–d) and interfaced to achieve collocation of the same station distances and depths, as depicted in Fig. 24a–b. From these interfaced mesh models, 110 datasets were considered to have very close to perfect collocation and were extracted and analyzed employing the enumerated ML techniques. The collocation of the interfaced velocity–resistivity

models was based on the weighted zoning of their values with depths. It's worth noting that while Akingboye and Bery (2023a) had adequately used supervised statistical modeling for the same data, the K-means clustering algorithm serves as an additional improvement for models' correlation and the clustering of datasets representative of lithologic units. K-means clustering, originating from signal processing, is a technique of vector quantization. It works by iteratively assigning data points to the nearest cluster centroid and updating the centroids based on the mean of the assigned data points. This process continues until the centroids stabilize or a maximum number of iterations is reached (Delforge et al. 2021). K-means clustering is a widely used method for uncovering patterns in data, but its effectiveness depends on choosing the right number of clusters and initialization method for optimal performance (Di Giuseppe et al. 2014; Sinaga and Yang 2020).

The derived K-means clustering model for the analyzed collocated datasets is shown in Fig. 25a, depicting four clusters (A–D) with their centroids. This model aligns perfectly with the statistical (regression) model in Fig. 25b, effectively capturing the four clusters. These clusters accurately represent the surface–subsurface lithologies and their corresponding ranges of V_p and resistivity values, offering insights into the lithological conditions of a typical granitic terrain in the tropics. This suggests that both ML approaches are effective tools for lithological modeling, reducing interpretation ambiguities and unrealistic conclusions. Moreover, the generated empirical relation, accurately verified using p-value and R^2 value ($\approx 85.2\%$), proves to be efficient for predicting V_p values over a large area, thus minimizing survey costs.

Exploring electrical and seismic refraction methods: theories to emerging prospects

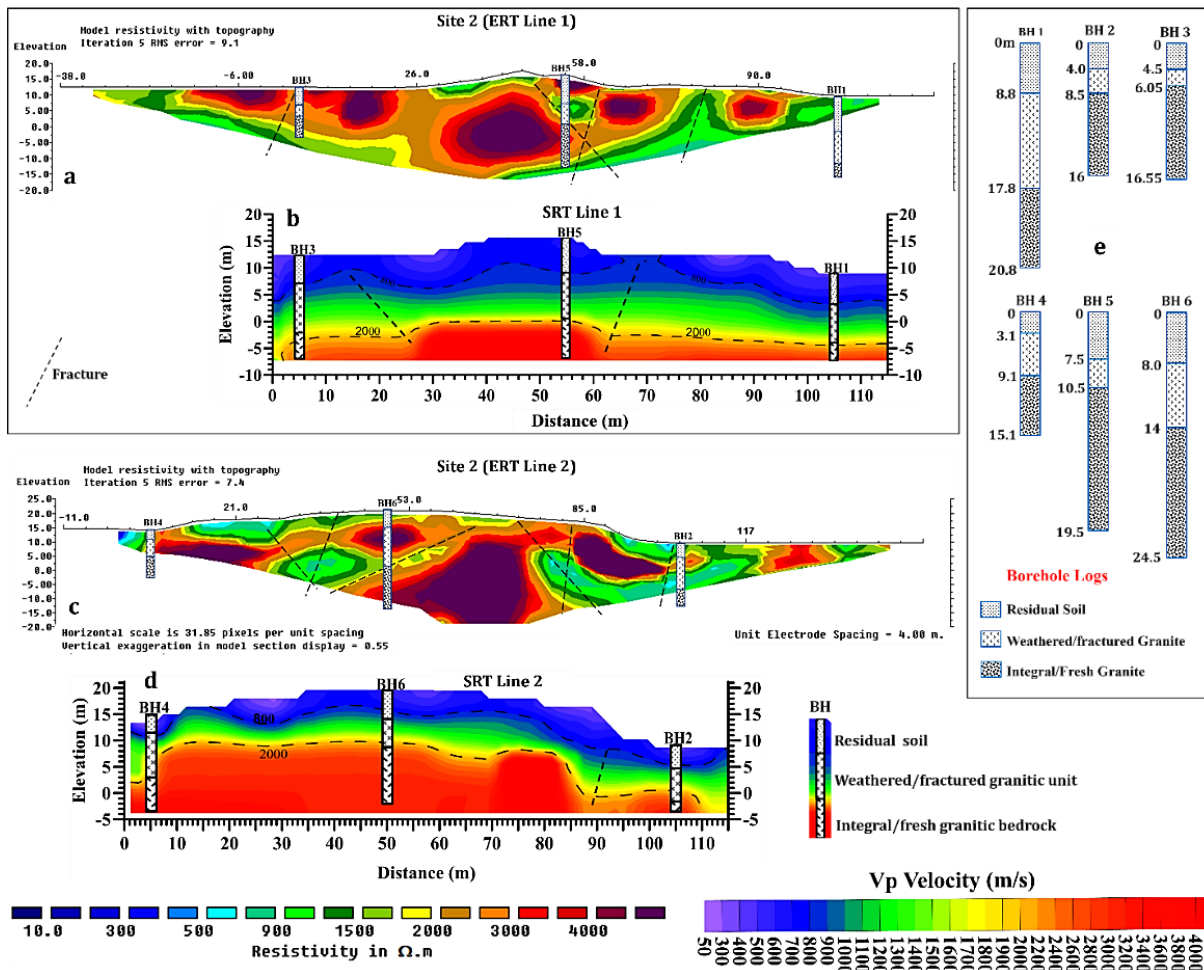


Fig. 23. 2-D ERT and SRT inversion models of (a–b) Line 1, (c–d) Line 2, and (e) the borehole lithological logs of BH1–BH6 at the Batu Maung area of Penang Island, Malaysia.

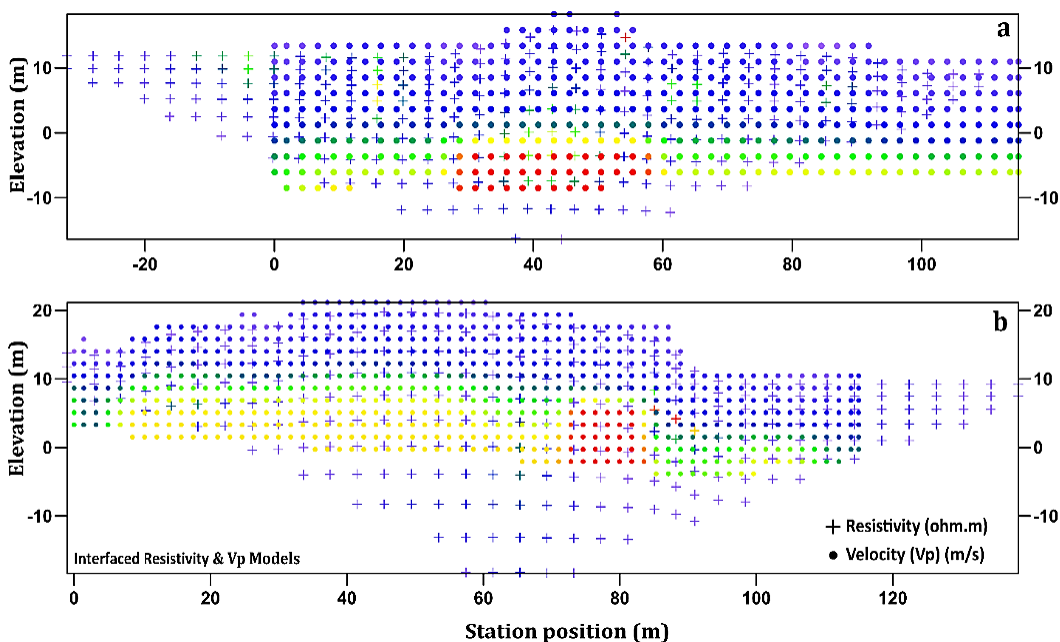


Fig. 24. Interfaced Vp and resistivity mesh models of section Lines 1 and 2 for Site 2 in the study area.

Exploring electrical and seismic refraction methods: theories to emerging prospects

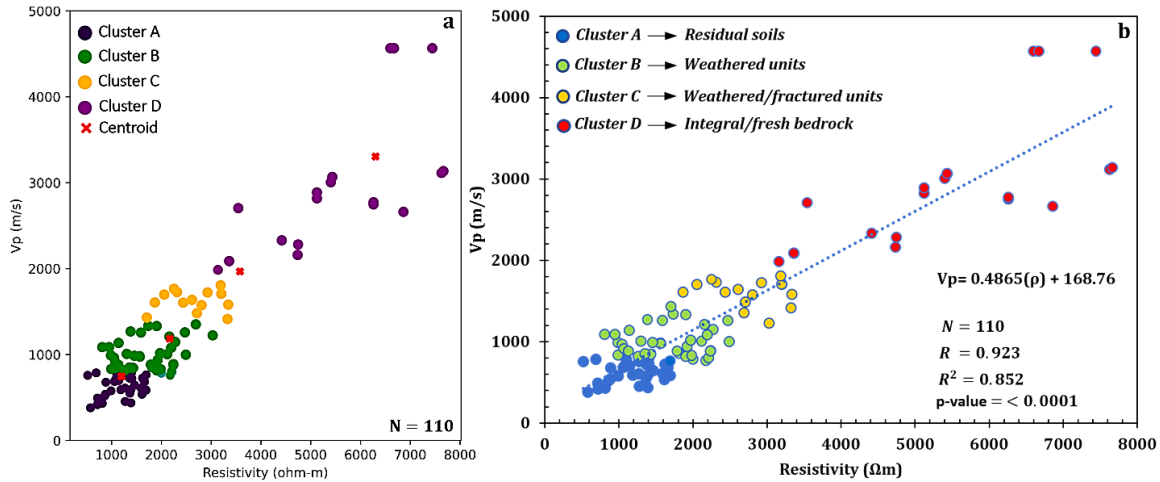


Fig. 25. (a) K-means clustering and (b) statistical (regression) models for the collocated velocity–resistivity datasets in the study area.

6.3 A case of a typical crystalline basement terrain of SW Nigeria

The case study location is situated within the Araromi area in Akungba-Akoko, Ondo State, southwestern Nigeria (Fig. 26a–d). The climate in this region is characterized by the Nigerian rainforest

belt, featuring distinct wet and dry seasons. Geologically, the site falls within the Nigerian Southwestern Precambrian Basement Complex, which is part of the reactivated Pan-African mobile belt situated east of the West African Craton and northwest of the Congo-Gabon Craton (Kröner et al. 2001; Obaje 2009; Okpoli and Akingboye 2019; Ogunyele et al. 2020a; Faruwa et al. 2021), as shown in Fig. 26a.

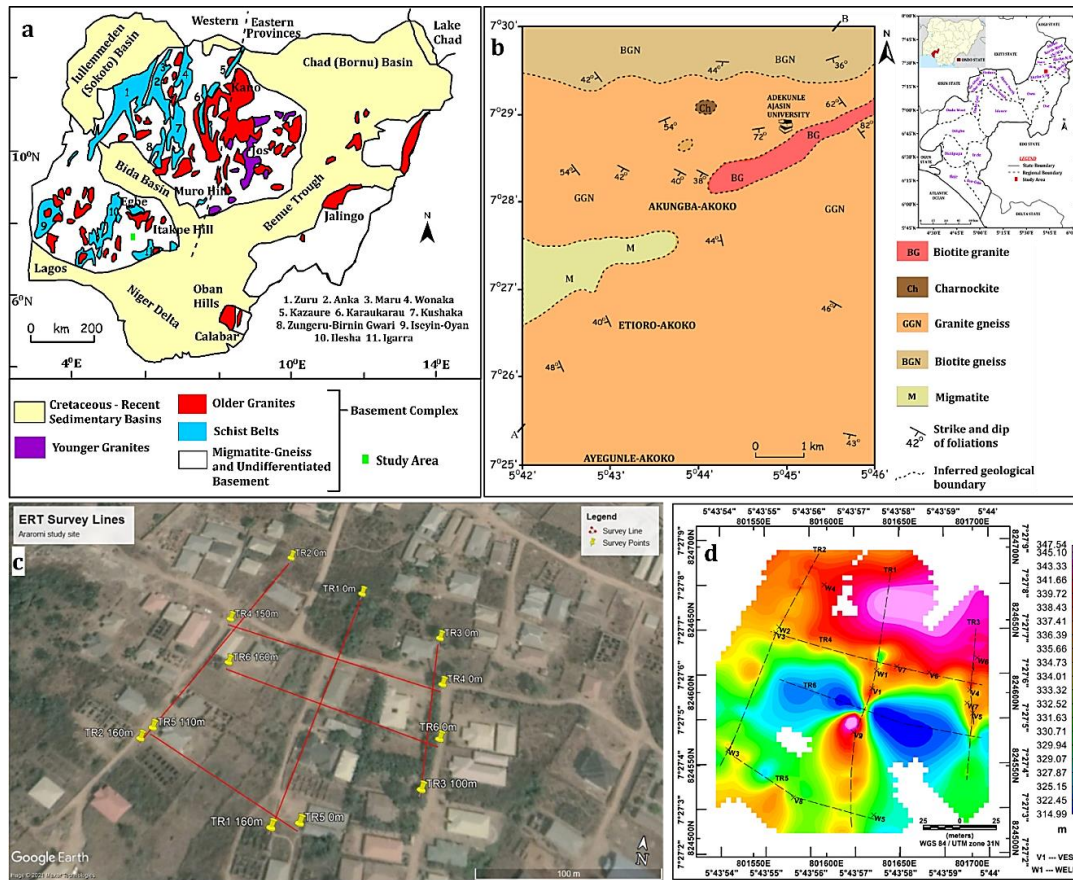


Fig. 26. (a) Nigerian regional geological map showing the study area within the Southwestern Basement Complex (modified after Woakes et al. 1987). (c) Geological map of Akungba-Akoko and its environs in Ondo State, SW Nigeria (after Ogunyele et al. 2020; Akingboye and Osazuwa 2021). (c) Aerial data acquisition and (d) elevation maps of the study showing all six ERT lines, eight VES survey points, and existing hand-dug well locations.

Akungba-Akoko is underlain by the Migmatite-Gneiss Complex (MGC) rocks, which are intruded by the Pan-African Granitoids (Ogunyele et al. 2020b; Akingboye et al. 2021), Fig. 26b. The MGC rocks in the area comprise migmatite, granite gneiss, and biotite gneiss, along with granitoids consisting mainly of charnockites and granites. Granite gneisses are the predominant rock type in the investigated area, with intrusions such as quartz veins, pegmatites, aplite, basic dykes, and sills (Ogunyele et al. 2020b; Akingboye et al. 2021). This area, like the case studies from Penang Island, is situated in the tropics but exhibits a variety of crystalline rocks, including granite. Consequently, the investigated localities in these two different countries will provide insights into the nature of surface–subsurface lithological differentiations, as well as the weathering, fracturing, and subsurface conditions experienced by the rocks.

To comprehensively assess subsurface geological conditions and dynamics in the area, six traverses (TRs) were conducted (Fig. 26c–d), employing both dipole-dipole resistivity profiling and Schlumberger electric resistivity sounding (VES). TRs 1–3 and TRs 4–6 were strategically established with 5 m spacing in a groundwater deficit location, attributed to the complex subsurface geology. TRs 1, 2, and 6 were each 160 m long, TR3 was 100 m, TR4 was 145 m long, and TR5 had a profile length of 110 m. The irregular traverse lengths were due to structural building obstructions. VES measurements were conducted at designated conductive or relatively conductive station points, serving as constraints for ERT models in

the absence of boreholes and imaging deep-weathered bodies and penetrative fractures. ERT field datasets were interpreted using the discussed inversion procedures. However, VES datasets were iteratively inverted using IPI2win software to generate model resistivity curves with layer information, thicknesses, and corresponding depths.

The interpreted inversion models for the six traverses in Araromi, Akungba-Akoko, like typical ERT models, reveal four distinct subsurface layers: topsoil, weathered layer, weathered/fractured bedrock, and fresh gneissic bedrock, with varied resistivity values of <10 to $600 \Omega\text{m}$, 600 to $<1000 \Omega\text{m}$, $>1200 \Omega\text{m}$, and $>1200 \Omega\text{m}$, respectively (Fig. 27a–f). The conductivity responses beneath all survey traverses depict the variability and extent of subsurface weathered materials and water- and sand-filled zones. These conductive and deep-weathered/fractured zones were delineated by the eight VES model results (VES points 1–8) listed in Table 3. Topsoil thickness ranges from 1.16 m to 3.8 m, while weathering of the bedrock profiles commences from shallow depths to about 10.3 m, influencing fractured zones and giving rise to subsurface apertures of varying sizes. The weathered/fractured bedrock extends to over 39 m in some sections along the surveyed VES 7 (Fig. 27d; Table 3) and beyond 52 m (Table 3). These deep sections, as indicated in Table 3 and on the ERT, are suggested as potential zones for sustainable groundwater development in the area.

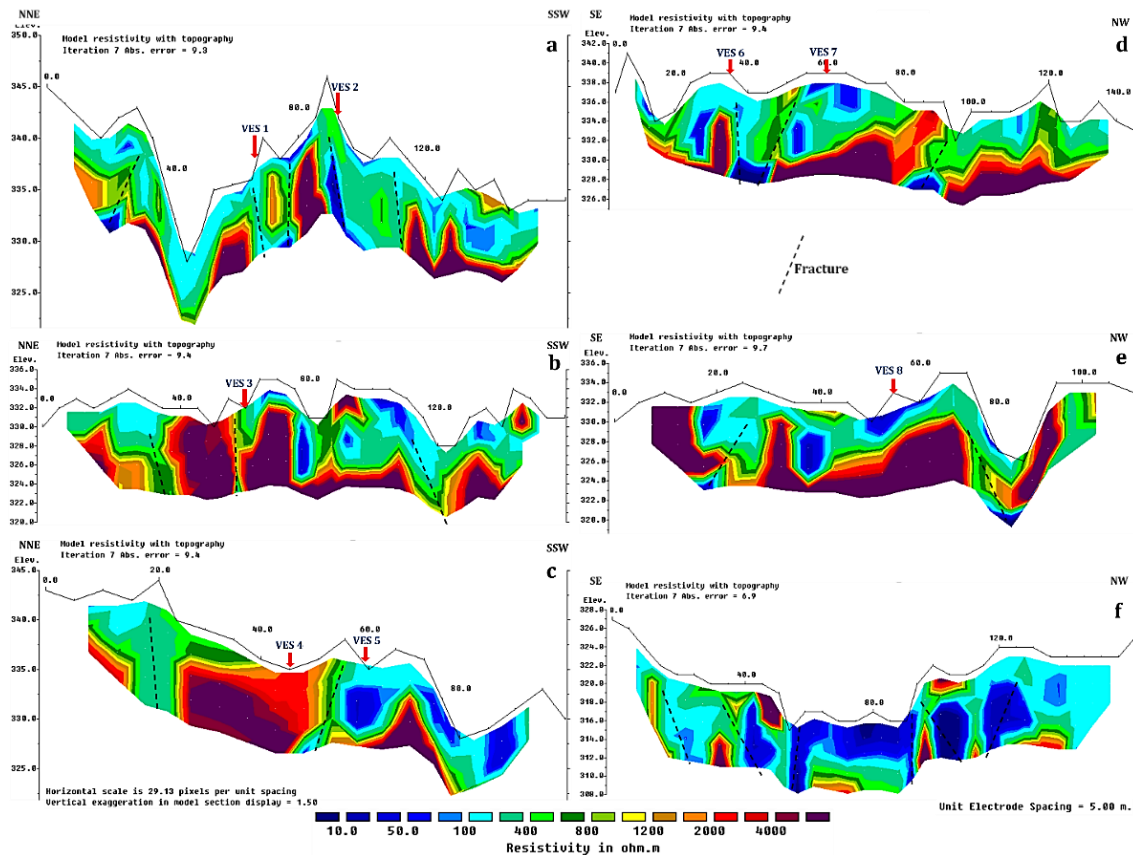


Fig. 27. ERT inversion models of (a) Traverse 1, (b) Traverse 2, (c) Traverse 3, (d) Traverse 4, (e) Traverse 5, and (f) Traverse 6. Red arrows show the VES point locations along the traverses

Table 3. Iteratively generated VES curve type results with their inferred lithological interpretation.

ERT traverse	VES point	Station (m)	Curve type	Resistivity (Ωm)	Thickness, h (m)	Depth, H (m)	Lithological inferred interpretation	
1	VES1	67.5	KQ	19.4	1.16	1.16	Topsoil (clay-rich)	
				7847	7.45	8.61	Fresh gneissic bedrock slab	
				415	43.60	52.20	Deep weathered trough/fractured bedrock (water-saturated column)	
				143	----			
	VES2	95	HA	110	1.51	1.51	Topsoil	
				29.2	3.13	4.64	Water-saturated weathered trough	
				699	50.10	54.80	Fractured bedrock slab	
				912	----		Partially weathered trough.	
2	VES3	60	A	106	1.27	1.27	Topsoil	
				415	4.40	5.67	Sandy weathered trough	
				2736	----		Fresh gneissic bedrock	
3	VES4	45	A	158	3.50	3.50	Topsoil	
				1218	12.7	16.20	Gradually increasing resistive fresh bedrock slab	
				5207	----			
	VES5	58	A	137	2.59	2.59	Topsoil	
				521	7.71	10.30	Sandy weathered trough	
				1288	----		Fresh bedrock slab	
4	VES6	35	A	57.5	1.68	1.68	Topsoil	
				546	4.92	6.60	Sandy weathered trough	
				7451	----		Fresh bedrock slab	
		VES7	60	AK	53.42	1.30	1.30	Topsoil
					267.6	4.50	5.80	Saturated sandy weathered trough
					2476	33.15	38.95	Fresh bedrock slab
			838.1	----		Fractured bedrock column		
5	VES8	55	H	567	1.35	1.35	Topsoil	
				138	5.17	6.52	Sandy clay weathered trough	
				3872	----		Fresh bedrock slab	

Notably, Fig. 27a–f reveals evidence of intense deformation in the bedrock, attributable to prevalent intense metamorphism in the area, resulting in rugose subsurface bedrock surfaces and varying sizes of localized open-to-surface weathering and fracturing. The models mirror comparable features to those mapped beneath Penang Island, although Penang's models depict deeper weathering profiles at Site 1 compared to Site 2 and the models of the Araromi area. This disparity arises from the granitic bedrock of Penang Island being subjected to intense chemical weathering due to the region's yearly high rainfall and heat (Bery and Saad 2012; Zakaria et al. 2022).

7. Conclusions

This comprehensive review delves deeply into the intricacies of electrical and seismic refraction methods, including their emergent techniques—ERT and SRT, shedding light on their pivotal roles in uncovering surface–subsurface crustal dynamics. Additionally, the review provides insights into the induced polarization method and briefly touches on the self-polarization method. From the principles governing their operation to the intricacies of data acquisition, processing, and interpretation, as well as emerging prospects, this review offers prospective insights into the heart of geophysical exploration. Case studies using real-time field resistivity and V_p datasets further illustrate these concepts.

ERT is a powerful tool capable of imaging vivid pictures of surface–subsurface resistivity distributions, offering invaluable insights into geological formations, hydrological processes, and environmental assessments. Similarly, SRT stands tall in its ability to

unveil the velocity structures hidden beneath the Earth's surface, shedding light on seismic hazards, engineering challenges, and hydrocarbon reservoirs. The principles, data acquisition techniques, processing methodologies, and interpretation strategies for both ERT and SRT were discussed, highlighting their strengths and limitations. Interestingly, this study is not just about these geophysical tools—it is about the arrays of innovation and discovery that surround them. In recent years, the invention of machine learning (ML) in geophysics has birthed a new era of possibilities, refining our understanding of electrical and seismic velocity methods in subsurface characterization like never before.

The advancement of ML algorithms, particularly deep learning techniques, has revolutionized the interpretation of ERT and SRT data, enabling more accurate and efficient subsurface imaging. Supervised and unsupervised ML approaches show promise in identifying geological features, establishing velocity–resistivity relationships, and improving inversion accuracy. Cross-plot analysis emerges as another valuable tool for interpreting velocity and resistivity datasets, aiding in geological characterization and hazard assessments. Moreover, the review emphasizes the importance of integrating domain-specific knowledge with data-driven approaches to overcome challenges in subsurface characterization. Hybrid ML algorithm models also have great potential in enhancing the reliability and accuracy of subsurface interpretations. The proposed methodological frameworks provide systematic approaches for modeling ERT and SRT data, facilitating the establishment of

velocity–resistivity relationships and the characterization of geological formations.

However, challenges persist. The intricacies of lithology, the subtleties of geological processes, and the inherent uncertainties in geophysical data necessitate a multidisciplinary approach. By leveraging cutting-edge techniques and integrating multidisciplinary approaches, these methods offer valuable tools for understanding subsurface structures, assessing environmental risks, and informing decision-making processes in various industries. Notably, these mentioned approaches were also adequately demonstrated by the efficacies of the results derived for studied sites. Nevertheless, continued research and innovation in ERT and SRT will further enhance their capabilities, driving advancements in subsurface imaging and geological exploration.

Acknowledgments

The author expresses gratitude to Dr. Andy A. Bery for his assistance throughout the collection of field data, as well as financial support contributed towards the use of data from Penang Island, Malaysia. Funds and state-of-the-art equipment provided by the Tertiary Education Trust Fund of Nigeria, Adekunle Ajasin University, Universiti Sains Malaysia (School of Physics), and Helmholtz Centre Potsdam – GFZ German Research Centre for Geosciences through HiDA Fellowship are greatly appreciated.

Funding

This research is supported by funding from the Tertiary Education Trust Fund of Nigeria through Adekunle Ajasin University, Universiti Sains Malaysia through Dr. Andy A. Bery, and the PhD short-stay research grant from the Helmholtz Information and Data Science Academy (HiDA).

Data Availability

All data generated or analyzed during this study are included in this published article. The author can make other supporting analyzed data available upon reasonable request.

Declaration of Competing Interest

The authors declare no known competing financial interests or personal relationships that could have appeared to influence the work reported in this paper.

References

- Abdullah FM, Loke MH, Nawawi M, et al (2022) Utilizing NWCR optimized arrays for 2D ERT survey to identify subsurface structures at Penang Island, Malaysia. *J Appl Geophys* 196:104518. <https://doi.org/10.1016/j.jappgeo.2021.104518>
- Abdullah FM, Loke MH, Nawawi M, Abdullah K (2018) Assessing the reliability and performance of optimized and conventional resistivity arrays for shallow subsurface investigations. *J Appl Geophys* 155:237–245. <https://doi.org/10.1016/j.jappgeo.2018.06.018>
- Abdullah FM, Loke MH, Nawawi M, Abdullah K (2019) Improving the Resolution of 3-D Resistivity Surveys Along the Perimeter of a Confined Area Using Optimized Arrays. *Pure Appl Geophys* 176:1701–1715. <https://doi.org/10.1007/s00024-018-2061-0>
- Acheson CH (1963) Time-depth and velocity-depth relations in western Canada. *GEOPHYSICS* 28:894–909. <https://doi.org/10.1190/1.1439292>
- Adeola AO, Akingboye AS, Ore OT, et al (2022) Crude oil exploration in Africa: socio-economic implications, environmental impacts, and mitigation strategies. *Environ Syst Decis* 42:26–50. <https://doi.org/10.1007/s10669-021-09827-x>
- Adrian J, Tezkan B, Candansayar ME (2022) Exploration of a Copper Ore Deposit in Elbistan/Turkey Using 2D Inversion of the Time-Domain Induced Polarization Data by Using Unstructured Mesh. *Pure Appl Geophys* 179:2255–2272. <https://doi.org/10.1007/s00024-022-03071-3>
- Ahmad F, Yahaya AS, Farooqi MA (2006) Characterization and Geotechnical Properties of Penang Residual Soils with Emphasis on Landslides. *Am J Environ Sci* 2:121–128. <https://doi.org/10.3844/ajessp.2006.121.128>
- Aizebeokhai AP (2014) Assessment of soil salinity using electrical resistivity imaging and induced polarization methods. *African J Agric Res* 9:3369–3378. <https://doi.org/10.5897/AJAR2013.8008>
- Akingboye AS (2024) Geophysical research on the interplays between soil–rock variability and hydrogeological structures: a case study. *Q J Eng Geol Hydrogeol* 57:. <https://doi.org/10.1144/qjegh2023-100>
- Akingboye AS (2023) RQD modeling using statistical-assisted SRT with compensated ERT methods: Correlations between borehole-based and SRT-based RMQ models. *Phys Chem Earth, Parts A/B/C* 131:103421. <https://doi.org/10.1016/j.pce.2023.103421>
- Akingboye AS (2022) Geohydraulic characteristics and groundwater vulnerability assessment of tropically weathered and fractured gneissic aquifers using combined georesistivity and geostatistical methods. *J Niger Soc Phys Sci* 4:497. <https://doi.org/10.46481/jnsps.2022.497>
- Akingboye AS, Bery AA (2023a) Development of novel velocity–resistivity relationships for granitic terrains based on complex collocated geotomographic modeling and supervised statistical analysis. *Acta Geophys* 71:2675–2698. <https://doi.org/10.1007/s11600-023-01049-w>
- Akingboye AS, Bery AA (2023b) Rock mass quality evaluation via statistically optimized geophysical datasets. *Bull Eng Geol Environ* 82:376. <https://doi.org/10.1007/s10064-023-03380-4>
- Akingboye AS, Bery AA (2021a) Performance evaluation of copper and stainless-steel electrodes in electrical tomographic imaging. *J Phys Sci* 32:13–29. <https://doi.org/10.21315/jps2021.32.3.2>
- Akingboye AS, Bery AA (2022a) Characteristics and rippability conditions of near-surface lithologic units (Penang Island, Malaysia) derived from multimethod geotomographic models and geostatistics. *J Appl Geophys* 204:104723. <https://doi.org/10.1016/j.jappgeo.2022.104723>
- Akingboye AS, Bery AA (2021b) Evaluation of lithostratigraphic units and groundwater potential using the resolution capacities of two different electrical tomographic electrodes at dual-spacing. *Contrib to Geophys Geod* 51:295–320. <https://doi.org/10.31577/congeo.2021.51.4.1>
- Akingboye AS, Bery AA (2022b) Development of Novel Velocity-Resistivity Geostatistical Relationships for Tropical Granitic Environments. In: 83rd EAGE Annual Conference & Exhibition. European Association of Geoscientists & Engineers, Madrid, Spain, pp 1–5
- Akingboye AS, Bery AA, Kayode JS, et al (2023) Groundwater-yielding capacity, water–rock interaction, and vulnerability assessment of typical gneissic hydrogeologic units using geoelectrohydraulic method. *Acta Geophys* 71:697–721. <https://doi.org/10.1007/s11600-022-00930-4>
- Akingboye AS, Bery AA, Kayode JS, et al (2022) Near-Surface Crustal Architecture and Geohydrodynamics of the Crystalline Basement Terrain of Araromi, Akungba-Akoko, SW Nigeria, Derived from Multi-Geophysical Methods. *Nat Resour Res* 31:215–236. <https://doi.org/10.1007/s11053-021-10000-z>
- Akingboye AS, Ogunyele AC (2019) Insight into seismic refraction and electrical resistivity tomography techniques in subsurface investigations. *Rud Geol Naft Zb* 34:93–111. <https://doi.org/10.17794/rgn.2019.1.9>
- Akingboye AS, Ogunyele AC, Jimoh AT, et al (2021) Radioactivity, radiogenic heat production and environmental radiation risk of the Basement Complex rocks of Akungba-Akoko, southwestern Nigeria: insights from in situ gamma-ray spectrometry. *Environ Earth Sci* 80:. <https://doi.org/10.1007/s12665-021-09516-7>
- Akingboye AS, Osazuwa IB (2021) Subsurface geological, hydrogeophysical and engineering characterisation of Etioro-Akoko, southwestern Nigeria, using electrical resistivity tomography. *NRIAG J Astron Geophys* 10:43–57. <https://doi.org/10.1080/20909977.2020.1868659>
- Akingboye AS, Osazuwa IB, Mohammed MZ (2020) Electrical resistivity

- tomography for geoenvironmental investigation of subsurface defects: A case study of Etioro-Akoko highway, Ondo State, Southwestern Nigeria. *Stud Quat* 37:101–107. <https://doi.org/10.24425/sq.2020.133754>
- Akintorinwa OJ, Atitebi MO, Akinlalu AA (2020) Hydrogeophysical and aquifer vulnerability zonation of a typical basement complex terrain: A case study of Odode Idanre southwestern Nigeria. *Heliyon* 6:e04549. <https://doi.org/10.1016/j.heliyon.2020.e04549>
- Aleardi M, Vinciguerra A, Hojat A (2021) A convolutional neural network approach to electrical resistivity tomography. *J Appl Geophys* 193:104434. <https://doi.org/10.1016/j.jappgeo.2021.104434>
- Anyiam OA, Mode AW, Okara ES (2018) The use of cross-plots in lithology delineation and petrophysical evaluation of some wells in the western Coastal Swamp, Niger Delta. *J Pet Explor Prod Technol* 8:61–71. <https://doi.org/10.1007/s13202-017-0364-9>
- Argote-Espino D, Tejero-Andrade A, Cifuentes-Nava G, et al (2013) 3D electrical prospecting in the archaeological site of El Pahñu, Hidalgo State, Central Mexico. *J Archaeol Sci* 40:1213–1223. <https://doi.org/10.1016/j.jas.2012.08.034>
- Arifin MH, Mohd Nazer NS, Jalal AQ (2020) Identification of the main mechanism of shallow landslides in Bukit Fraser, Pahang. *Bull Geol Soc Malaysia* 69:79–88. <https://doi.org/10.7186/bgsm69202007>
- Arosio D, Aguzzoli A, Zanzi L, et al (2023) Lab and Field Tests of a Low-Cost 3-Component Seismometer for Shallow Passive Seismic Applications. *Earth Sp Sci* 10:1–12. <https://doi.org/10.1029/2023EA002934>
- Arosio D, Munda S, Tresoldi G, et al (2017) A customized resistivity system for monitoring saturation and seepage in earthen levees: installation and validation. *Open Geosci* 9:457–467. <https://doi.org/10.1515/geo-2017-0035>
- Auken E, Christiansen AV, Kirkegaard C, et al (2015) An overview of a highly versatile forward and stable inverse algorithm for airborne, ground-based, and borehole electromagnetic and electric data. *Explor. Geophys.* 46:223–235
- Bai D, Lu G, Zhu Z, et al (2022) Using Electrical Resistivity Tomography to Monitor the Evolution of Landslides' Safety Factors under Rainfall: A Feasibility Study Based on Numerical Simulation. *Remote Sens* 14. <https://doi.org/10.3390/rs14153592>
- Baker HA, Djeddi M, Boudjadja AG, Benhamam K (2001) A Different Approach in Delineating Near Surface Buried Structures. In: 63rd EAGE Conference & Exhibition. European Association of Geoscientists & Engineers, pp 1–4
- Bala GA, Bery AA, Gnapragasan J, Akingboye AS (2024) Development of novel resistivity-chargeability statistical relationships for subsurface characterization at Langkawi, Kedah. *Environ Sci Pollut Res.* <https://doi.org/10.1007/s11356-024-32867-0>
- Barton N (2006) *Rock Quality, Seismic Velocity, Attenuation and Anisotropy*. CRC Press
- Bayewu OO, Oloruntola MO, Mosuro GO, et al (2016) Application of cross-square array and resistivity anisotropy for fracture detection in crystalline bedrock. *Arab J Geosci* 9:1–16. <https://doi.org/10.1007/s12517-016-2305-1>
- Becken M, Burkhardt H (2004) An ellipticity criterion in magnetotelluric tensor analysis. *Geophys J Int* 159:69–82. <https://doi.org/10.1111/j.1365-246X.2004.02376.x>
- Benevides AS, Meju MA, Fontes SL, et al (2024) Deep Structure of the Santos Basin, Offshore Brazil From 3D Inversion of magnetotelluric Data. *J Geophys Res Solid Earth* 129. <https://doi.org/10.1029/2023JB027329>
- Bergmann P, Diersch M, Götz J, et al (2016) Review on geophysical monitoring of CO₂ injection at Ketzin, Germany. *J Pet Sci Eng* 139:112–136. <https://doi.org/10.1016/j.petrol.2015.12.007>
- Bergmann P, Schmidt-Hattenberger C, Kiessling D, et al (2012) Surface-downhole electrical resistivity tomography applied to monitoring of CO₂ storage at Ketzin, Germany. *Geophysics* 77. <https://doi.org/10.1190/geo2011-0515.1>
- Bernardinetti S, Bruno PPG (2019) The Hydrothermal System of Solfatara Crater (Campi Flegrei, Italy) Inferred From Machine Learning Algorithms. *Front Earth Sci* 7:1–18. <https://doi.org/10.3389/feart.2019.00286>
- Bery AA (2016) Resolution Enhancement in Model Resistivity using the Data Levels Amalgamation Technique for Groundwater Exploration
- Bery AA, Saad R (2012) Tropical Clayey Sand Soil's Behaviour Analysis and Its Empirical Correlations via Geophysics Electrical Resistivity Method and Engineering Soil Characterizations. *Int J Geosci* 03:111–116. <https://doi.org/10.4236/ijg.2012.31013>
- Bièvre G, Jongmans D, Lebourg T, Carrière S (2021) Electrical resistivity monitoring of an earthslide with electrodes located outside the unstable zone (Pont-Bourquin landslide, Swiss Alps). *Near Surf Geophys* 19:225–239. <https://doi.org/10.1002/nsg.12145>
- Bing Z, Greenhalgh SA (2001) Finite element three-dimensional direct current resistivity modelling: Accuracy and efficiency considerations. *Geophys J Int* 145:679–688. <https://doi.org/10.1046/j.0956-540X.2001.01412.x>
- Binley A (2015) *Tools and Techniques: Electrical Methods*. In: *Treatise on Geophysics*. Elsevier, pp 233–259
- Binley A, Hubbard SS, Huisman JA, et al (2015) The emergence of hydrogeophysics for improved understanding of subsurface processes over multiple scales. *Water Resour Res* 51:3837–3866. <https://doi.org/10.1002/2015wr017016>
- Binley A, Kemna A (2005) *DC Resistivity and Induced Polarization Methods*. In: *Hydrogeophysics*. Springer Netherlands, Dordrecht, pp 129–156
- Biosca B, Arévalo-Lomas L, Barrio-Parra F, Díaz-Curiel J (2020) Application and limitations of time domain-induced polarization tomography for the detection of hydrocarbon pollutants in soils with electro-metallic components: a case study. *Environ Monit Assess* 192. <https://doi.org/10.1007/s10661-020-8073-0>
- Biswas A, Sharma SP (2017) Geophysical surveys for identifying source and pathways of subsurface water inflow at the Bangur chromite mine, Odisha, India. *Nat Hazards* 88:947–964. <https://doi.org/10.1007/s11069-017-2899-y>
- Bouchedda A, Bernard G, Gloaguen E (2017) Constrained electrical resistivity tomography Bayesian inversion using inverse Matern covariance matrix. *GEOPHYSICS* 82:E129–E141. <https://doi.org/10.1190/geo2015-0673.1>
- Cardarelli E, Di Filippo G (2009) Electrical resistivity and induced polarization tomography in identifying the plume of chlorinated hydrocarbons in sedimentary formation: A case study in Rho (Milan - Italy). *Waste Manag Res* 27:595–602. <https://doi.org/10.1177/0734242X09102524>
- Caterpillar Incorporation (2010) *Caterpillar Performance Handbook*. Caterpillar Inc 2264
- Chambers JE, Kuras O, Meldrum PI, et al (2006) Electrical resistivity tomography applied to geologic, hydrogeologic, and engineering investigations at a former waste-disposal site. *GEOPHYSICS* 71:B231–B239. <https://doi.org/10.1190/1.2360184>
- Chavez-Hernandez G, Tejero A, Alcantara MA, Chavez RE (2011) The “L-Array”, a 3D tool to characterize a fracture pattern in an urban zone. *Near Surf* 2011 - 17th Eur Meet Environ Eng Geophys 12–14
- Chávez RE, Cifuentes-Nava G, Esteban Hernández-Quintero J, et al (2014) Special 3D electric resistivity tomography (ERT) array applied to detect buried fractures on urban areas: San Antonio Tecómitl, Milpa Alta, México. *Geofísica Int* 53:425–434. [https://doi.org/10.1016/S0016-7169\(14\)70076-5](https://doi.org/10.1016/S0016-7169(14)70076-5)
- Cheng Q, Tao M, Chen X, Binley A (2019) Evaluation of electrical resistivity tomography (ERT) for mapping the soil–rock interface in karstic environments. *Environ Earth Sci* 78:1–14. <https://doi.org/10.1007/s12665-019-8440-8>
- Colombo D, Cogan M, Hallinan S, et al (2008a) Near-surface P-velocity modelling by integrated seismic, EM, and gravity data: examples from the Middle East. *First Break* 26:91–102. <https://doi.org/10.3997/1365-2397.26.10.28560>
- Colombo D, Keho T (2010) The non-seismic data and joint inversion strategy for the near surface solution in Saudi Arabia. In: *Society of Exploration Geophysicists International Exposition and 80th Annual Meeting 2010, SEG 2010*. pp 1934–1938
- Colombo D, Mantovani M, Hallinan S, Virgilio M (2008b) Sub-basalt depth imaging using simultaneous joint inversion of seismic and electromagnetic (MT) data: A CRB field study. In: *SEG Technical Program Expanded Abstracts*. pp 2674–2678
- Colombo D, Rovetta D, Al-Yousuf T, et al (2020) Multiple joint wavefield inversions: Theory and field data implementations. *Lead Edge* 39:411–421. <https://doi.org/10.1190/tle39060411.1>
- Cordero-Vázquez CY, Delgado-Rodríguez O, Peinado-Guevara HJ, et al

- (2021) Determination of soil properties from electrical measurements in agricultural plots, Villa De Arriaga, San Luis Potosí, Mexico. *Geofísica Int* 60:76–100
- Côrte G, Dramsch J, Amini H, MacBeth C (2020) Deep neural network application for 4D seismic inversion to changes in pressure and saturation: Optimizing the use of synthetic training datasets. *Geophys Prospect* 68:2164–2185. <https://doi.org/10.1111/1365-2478.12982>
- Crook N, Binley A, Knight R, et al (2008) Electrical resistivity imaging of the architecture of streambed sediments. *Water Resour Res* 46:0–13. <https://doi.org/10.1029/2008WR006968>
- Dahlin T (1996) 2D resistivity surveying for environmental and engineering applications. *First Break* 14:275–283. <https://doi.org/10.3997/1365-2397.1996014>
- Dahlin T, Leroux V, Nissen J (2002) Measuring techniques in induced polarisation imaging. *J Appl Geophys* 50:279–298. [https://doi.org/10.1016/S0926-9851\(02\)00148-9](https://doi.org/10.1016/S0926-9851(02)00148-9)
- Dahlin T, Loke MH (2018) Underwater ERT surveying in water with resistivity layering with example of application to site investigation for a rock tunnel in central Stockholm. *Near Surf Geophys* 16:230–237. <https://doi.org/10.3997/1873-0604.2018007>
- Dahlin T, Wisén R (2018) Combined Electric Resistivity Tomography and Seismic Refraction Tomography in Brackish Water in Saltsjön in Stockholm. In: 3rd Applied Shallow Marine Geophysics Conference. European Association of Geoscientists & Engineers, pp 1–5
- Daily W, Ramirez A, Binley A, LaBrecque D (2005) Electrical Resistance Tomography—Theory and Practice. In: *Near-Surface Geophysics*. Society of Exploration Geophysicists, pp 525–550
- Day-Lewis FD, White EA, Johnson CD, et al (2006) Continuous resistivity profiling to delineate submarine groundwater discharge—examples and limitations. *Lead Edge* 25:724–728. <https://doi.org/10.1190/1.2210056>
- DeGroot-Hedlin C, Constable S (1990) Occam's inversion to generate smooth, two-dimensional models from magnetotelluric data. *GEOPHYSICS* 55:1613–1624. <https://doi.org/10.1190/1.1442813>
- Delaplanché J, Hagemann RF, Bolland PGC (1963) An example of the use of synthetic seismograms. *GEOPHYSICS* 28:842–854. <https://doi.org/10.1190/1.1439282>
- Delforge D, Watlet A, Kaufmann O, et al (2021) Time-series clustering approaches for subsurface zonation and hydrofacies detection using a real time-lapse electrical resistivity dataset. *J Appl Geophys* 184. <https://doi.org/10.1016/j.jappgeo.2020.104203>
- Delgado-Gonzalez L, Forquet N, Choubert JM, et al (2023) Flow path monitoring by discontinuous time-lapse ERT: An application to survey relationships between secondary effluent infiltration and roots distribution. *J Environ Manage* 326. <https://doi.org/10.1016/j.jenvman.2022.116839>
- Di Giuseppe MG, Troiano A, Troise C, De Natale G (2014) K-Means clustering as tool for multivariate geophysical data analysis. An application to shallow fault zone imaging. *J Appl Geophys* 101:108–115. <https://doi.org/10.1016/j.jappgeo.2013.12.004>
- Dick MD, Bery AA, Okonna NN, et al (2024) A novel machine learning approach for interpolating seismic velocity and electrical resistivity models for early-stage soil-rock assessment. *Earth Sci Informatics* in press.
- Dimech A, Cheng L, Chouteau M, et al (2022) A Review on Applications of Time-Lapse Electrical Resistivity Tomography Over the Last 30 Years: Perspectives for Mining Waste Monitoring. *Surv Geophys* 43:1699–1759. <https://doi.org/10.1007/s10712-022-09731-2>
- Doetsch J, Linde N, Vogt T, et al (2012) Imaging and quantifying salt-tracer transport in a riparian groundwater system by means of 3D ERT monitoring. *GEOPHYSICS* 77:B207–B218. <https://doi.org/10.1190/geo2012-0046.1>
- Doetsch JA, Coscia I, Greenhalgh S, et al (2010) The borehole-fluid effect in electrical resistivity imaging. *GEOPHYSICS* 75:F107–F114. <https://doi.org/10.1190/1.3467824>
- Earle S (2019) *Physical Geology*, 2nd Editi. BCcampus
- Edwards LS (1977) A modified pseudosection for resistivity and IP. *GEOPHYSICS* 42:1020–1036. <https://doi.org/10.1190/1.1440762>
- Fang G, Li YE, Zhao Y, Martin ER (2020) Urban Near-Surface Seismic Monitoring Using Distributed Acoustic Sensing. *Geophys Res Lett* 47:1–9. <https://doi.org/10.1029/2019GL086115>
- Faruwa AR, Qian W, Akinsunmade A, et al (2021) Aeromagnetic and remote sensing characterization of structural elements influencing iron ore deposits and other mineralization in Kabba, southwestern Nigeria. *Adv Sp Res* 68:3302–3313. <https://doi.org/10.1016/j.asr.2021.06.024>
- Folch A, del Val L, Luquot L, et al (2020) Combining fiber optic DTS, cross-hole ERT and time-lapse induction logging to characterize and monitor a coastal aquifer. *J Hydrol* 588:125050. <https://doi.org/10.1016/j.jhydrol.2020.125050>
- Gallardo LA (2004) Joint two-dimensional DC resistivity and seismic travel time inversion with cross-gradients constraints. *J Geophys Res* 109:B03311. <https://doi.org/10.1029/2003JB002716>
- Gallardo LA, Meju MA (2003) Characterization of heterogeneous near-surface materials by joint 2D inversion of dc resistivity and seismic data. *Geophys Res Lett* 30. <https://doi.org/10.1029/2003GL017370>
- Gallardo LA, Meju MA (2007) Joint two-dimensional cross-gradient imaging of magnetotelluric and seismic traveltimes data for structural and lithological classification. *Geophys J Int* 169:1261–1272. <https://doi.org/10.1111/j.1365-246X.2007.03366.x>
- Gallardo LA, Meju MA (2011) Structure-coupled multiphysics imaging in geophysical sciences. *Rev Geophys* 49:RG1003. <https://doi.org/10.1029/2010RG000330>
- Gao Q, Hasan M, Shang Y, Qi S (2024) Geophysical estimation of 2D hydraulic conductivity for groundwater assessment in hard rock. *Acta Geophys*. <https://doi.org/10.1007/s11600-024-01310-w>
- Geomatrix Earth Science Ltd (2015) Marine Resistivity - Syscal Pro Deep Marine. In: Amasci Creat. Ltd. <https://www.geomatrix.co.uk/marine-products/electrical-resistivity/>. Accessed 28 Feb 2024
- Goto T, Kasaya T, Machiyama H, et al (2008) A marine deep-towed DC resistivity survey in a methane hydrate area, Japan Sea. *Explor Geophys* 39:52–59. <https://doi.org/10.1071/EG08003>
- Gourdol L, Clément R, Juilleret J, et al (2018) Large-scale ERT surveys for investigating shallow regolith properties and architecture. *Hydrol Earth Syst Sci Discuss* 1–39
- Grootes PM (2016) *Encyclopedia of Marine Geosciences*. Springer Netherlands, Dordrecht
- Guevara HJP, Barrientos JH, Rodríguez OD, et al (2017) Estimation of Hydrological Parameters from Geoelectrical Measurements. In: *Electrical Resistivity and Conductivity*. InTech
- Günther T, Martin T (2016) Spectral two-dimensional inversion of frequency-domain induced polarization data from a mining slag heap. *J Appl Geophys* 135:436–448. <https://doi.org/10.1016/j.jappgeo.2016.01.008>
- Gupta AK, Singh RK, Srivastava S (2019) Investigation of auriferous mineralisation over greenstone schist belt of Dhanjori Basin, Eastern India using 2D electrical resistivity tomography and induced polarisation surveys. *Explor Geophys* 50:364–375. <https://doi.org/10.1080/08123985.2019.1606204>
- Haberjarm GM (1972) The Effects of Anisotropy on Square Array Resistivity Measurements. *Geophys Prospect* 20:249–266. <https://doi.org/10.1111/j.1365-2478.1972.tb00631.x>
- Haberjarm GM, Watkins GE (1967) The Use of a Square Configuration in Resistivity Prospecting. *Geophys Prospect* 15:445–467. <https://doi.org/10.1111/j.1365-2478.1967.tb01798.x>
- Hasan M, Shang Y (2023) Investigating the groundwater resources of weathered bedrock using an integrated geophysical approach. *Environ Earth Sci* 82:213. <https://doi.org/10.1007/s12665-023-10892-5>
- Hasan M, Shang Y, Jin W, Akhter G (2021) Joint geophysical prospecting for groundwater exploration in weathered terrains of South Guangdong, China. *Environ Monit Assess* 193. <https://doi.org/10.1007/s10661-021-09521-0>
- Hasan M, Shang Y, Yi X, et al (2023) Determination of rock quality designation (RQD) using a novel geophysical approach: a case study. *Bull Eng Geol Environ* 82:86. <https://doi.org/10.1007/s10064-023-03113-7>
- Hassan K (1990) A summary of the Quaternary geology investigations in Seberang Prai, Pulau Pinang and Kuala Kurau. *Bull Geol Soc Malaysia* 26:47–53. <https://doi.org/10.7186/bgsm26199005>
- Hayashi K, Konishi C (2010) Joint Use of a Surface-Wave Method and a Resistivity Method for Safety Assessment of Levee Systems. In: *GeoFlorida 2010*. American Society of Civil Engineers, Reston, VA, pp 1340–1349
- Helene LPI, Moreira CA, Bovi RC (2020) Identification of leachate infiltration and its flow pathway in landfill by means of electrical resistivity tomography (ERT). *Environ Monit Assess* 192. <https://doi.org/10.1007/s10661-020-09521-0>

- <https://doi.org/10.1007/s10661-020-8206-5>
- Hermans T, Paepen M (2020) Combined Inversion of Land and Marine Electrical Resistivity Tomography for Submarine Groundwater Discharge and Saltwater Intrusion Characterization. *Geophys Res Lett* 47:1–9. <https://doi.org/10.1029/2019GL085877>
- HGI (2021) HGI 30 Years of Excellence - hydroGeophysics. In: HGIworld.com. <https://www.hgiworld.com/geophysics-methods/electrical-resistivity/marine-resistivity/>. Accessed 28 Feb 2024
- Hiskiawan P, Chen C-C, Ye Z-K (2023) Processing of electrical resistivity tomography data using convolutional neural network in ERT-NET architectures. *Arab J Geosci* 16:581. <https://doi.org/10.1007/s12517-023-11690-w>
- Hoek E, Brown ET (1997) Practical estimates of rock mass strength. *Int J Rock Mech Min Sci* 34:1165–1186. [https://doi.org/10.1016/S1365-1609\(97\)80069-X](https://doi.org/10.1016/S1365-1609(97)80069-X)
- Hojat A, Arosio D, Ivanov VI, et al (2020) Quantifying seasonal 3D effects for a permanent electrical resistivity tomography monitoring system along the embankment of an irrigation canal. *Near Surf Geophys* 18:427–443. <https://doi.org/10.1002/NSG.12110>
- Holmes J, Chambers J, Wilkinson P, et al (2022) Application of petrophysical relationships to electrical resistivity models for assessing the stability of a landslide in British Columbia, Canada. *Eng Geol* 301:106613. <https://doi.org/10.1016/j.enggeo.2022.106613>
- Husainy SN, Bery AA, Abir IA, et al (2023) Landslide susceptibility mapping of Penang Island, Malaysia, using remote sensing and multi-geophysical methods. *Earth Sci Res J* 27:93–107. <https://doi.org/10.15446/esrj.v27n2.107274>
- Jackson MD (2015) *Tools and Techniques: Self-Potential Methods*. In: *Treatise on Geophysics*. Elsevier, pp 261–293
- Jianliang W, Iqbal I, Sanxi P, et al (2022) Integrated Geophysical Survey in Defining Subsidence Features of Glauber's Salt Mine, Gansu Province in China. *Geotech Geol Eng* 40:325–334. <https://doi.org/10.1007/s10706-021-01877-x>
- Jones F (2007) *Introduction to induced polarization surveying*. UCB Earth Ocean Sci 1–17
- Karaoulis M, Tsourlos P, Kim J -H., Revil A (2014) 4D time-lapse ERT inversion: introducing combined time and space constraints. *Near Surf Geophys* 12:25–34. <https://doi.org/10.3997/1873-0604.2013004>
- Karsh H, Babacan AE, Akin Ö (2024) Subsurface characterization by active and passive source geophysical methods after the 06 February 2023 earthquakes in Turkey. *Nat Hazards*. <https://doi.org/10.1007/s11069-024-06422-6>
- Kearey P, Brooks M, Hill I (2002) *An introduction to geophysical exploration*, 3rd Editio. Oxford: Blackwell Science
- Kemna A, Binley A, Slater L (2004) Crosshole IP imaging for engineering and environmental applications. *GEOPHYSICS* 69:97–107. <https://doi.org/10.1190/1.1649379>
- Kim DY (1964) Synthetic velocity log. In: 33rd AIM International SEG. SEG, New Orleans
- Kröner A, Ekwueme BN, Pidgeon RT (2001) The Oldest Rocks in West Africa: SHRIMP Zircon Age for Early Archean Migmatitic Orthogneiss at Kaduna, Northern Nigeria. *J Geol* 109:399–406. <https://doi.org/10.1086/319979>
- Kumar P, Tiwari P, Biswas A, Acharya T (2020) Geophysical and hydrogeological investigation for the saline water invasion in the coastal aquifers of West Bengal, India: a critical insight in the coastal saline clay-sand sediment system. *Environ Monit Assess* 192. <https://doi.org/10.1007/s10661-020-08520-x>
- Kumar P, Tiwari P, Singh A, et al (2021) Electrical Resistivity and Induced Polarization signatures to delineate the near-surface aquifers contaminated with seawater invasion in Digha, West-Bengal, India. *Catena* 207. <https://doi.org/10.1016/j.catena.2021.105596>
- Kuras O, Wilkinson PB, Meldrum PI, et al (2016) Geoelectrical monitoring of simulated subsurface leakage to support high-hazard nuclear decommissioning at the Sellafield Site, UK. *Sci Total Environ* 566–567:350–359. <https://doi.org/10.1016/j.scitotenv.2016.04.212>
- LaBrecque D, Daily W (2008) Assessment of measurement errors for galvanic-resistivity electrodes of different composition. *Geophysics* 73:F55–F64. <https://doi.org/10.1190/1.2823457>
- Lailly P, Bednar J (1983) The seismic inverse problem as a sequence of before stack migrations. In: *Conference on inverse scattering: theory and application*, SIAM, Philadelphia. pp 206–220
- Lane JW, Haeni FP, Watson WM (1995) Use of a Square-Array Direct-Current Resistivity Method to Detect Fractures in Crystalline Bedrock in New Hampshire. *Groundwater* 33:476–485. <https://doi.org/10.1111/j.1745-6584.1995.tb00304.x>
- Latrach A, Malki ML, Morales M, et al (2023) A Critical Review of Physics-Informed Machine Learning Applications in Subsurface Energy Systems. *arXiv (Preprint)* 33. <https://doi.org/https://doi.org/10.48550/arXiv.2308.04457>
- Lenhare BD, Moreira CA (2020) Geophysical Prospecting Over a Meta-Ultramafic Sequence with Indicators of Gold Mineralization in Rio Grande do Sul State, Southernmost Brazil. *Pure Appl Geophys* 177:5367–5383. <https://doi.org/10.1007/s00024-020-02559-0>
- Li S, Liu B, Ren Y, et al (2020) Deep-Learning Inversion of Seismic Data. *IEEE Trans Geosci Remote Sens* 58:2135–2149. <https://doi.org/10.1109/TGRS.2019.2953473>
- Li Y, Oldenburg DW (2000) 3-D inversion of induced polarization data. *Geophysics* 65:1931–1945. <https://doi.org/10.1190/1.1444877>
- Liu B, Guo Q, Li S, et al (2020) Deep Learning Inversion of Electrical Resistivity Data. *IEEE Trans Geosci Remote Sens* 58:5715–5728. <https://doi.org/10.1109/TGRS.2020.2969040>
- Liu B, Guo Q, Tang Y, Jang P (2023a) Deep learning inversion method of tunnel resistivity synthetic data based on modelling data. *Near Surf Geophys*. <https://doi.org/10.1002/nsg.12253>
- Liu B, Pang Y, Jiang P, et al (2023b) Physics-Driven Deep Learning Inversion for Direct Current Resistivity Survey Data. *IEEE Trans Geosci Remote Sens* 61:1–11. <https://doi.org/10.1109/TGRS.2023.3263842>
- Liu B, Yang S, Ren Y, et al (2021) Deep-learning seismic full-waveform inversion for realistic structural models. *GEOPHYSICS* 86:R31–R44. <https://doi.org/10.1190/geo2019-0435.1>
- Loke MH (2002) Rapid 2D resistivity forward modelling using the finite-difference and finite-element methods
- Loke MH, Barker RD (1996) Practical techniques for 3D resistivity surveys and data inversion. *Geophys Prospect* 44:499–523. <https://doi.org/10.1111/j.1365-2478.1996.tb00162.x>
- Loke MH, Chambers JE, Rucker DF, et al (2013) Recent developments in the direct-current geoelectrical imaging method. *J Appl Geophys* 95:135–156. <https://doi.org/10.1016/j.jappgeo.2013.02.017>
- Loke MH, Dahlin T, Rucker DF (2014a) Smoothness-constrained time-lapse inversion of data from 3D resistivity surveys. *Near Surf Geophys* 12:5–24. <https://doi.org/10.3997/1873-0604.2013025>
- Loke MH, Kiflu H, Wilkinson PB, et al (2015a) Optimized arrays for 2D resistivity surveys with combined surface and buried arrays. *Near Surf Geophys* 13:505–518. <https://doi.org/10.3997/1873-0604.2015038>
- Loke MH, Wilkinson PB, Chambers JE, et al (2015b) Optimized arrays for 2-D resistivity survey lines with a large number of electrodes. *J Appl Geophys* 112:136–146. <https://doi.org/10.1016/j.jappgeo.2014.11.011>
- Loke MH, Wilkinson PB, Chambers JE (2010a) Parallel computation of optimized arrays for 2-D electrical imaging surveys. *Geophys J Int* 183:1302–1315. <https://doi.org/10.1111/j.1365-246X.2010.04796.x>
- Loke MH, Wilkinson PB, Chambers JE, et al (2022) The use of asymmetric time constraints in 4-D ERT inversion. *J Appl Geophys* 197:104536. <https://doi.org/10.1016/j.jappgeo.2022.104536>
- Loke MH, Wilkinson PB, Chambers JE (2010b) Fast computation of optimized electrode arrays for 2D resistivity surveys. *Comput Geosci* 36:1414–1426. <https://doi.org/10.1016/j.cageo.2010.03.016>
- Loke MH, Wilkinson PB, Tejero-Andrade A, Kruse S (2015c) Optimized Arrays for Resistivity Measurements Confined to the Perimeter of a Survey Area. In: *Near Surface Geoscience 2015 - 21st European Meeting of Environmental and Engineering Geophysics*. pp 646–650
- Loke MH, Wilkinson PB, Uhlemann SS, et al (2014b) Computation of optimized arrays for 3-D electrical imaging surveys. *Geophys J Int* 199:1751–1764. <https://doi.org/10.1093/gji/ggu357>
- Mao D, Revil A, Hort RD, et al (2015) Resistivity and self-potential tomography applied to groundwater remediation and contaminant plumes: Sandbox and field experiments. *J Hydrol* 530:1–14
- Marquis G, Hyndman RD (1992) Geophysical support for aqueous fluids in the deep crust: seismic and electrical. *Geophys J Int* 110:91–105. <https://doi.org/10.1111/j.1365-246X.1992.tb00716.x>
- Martinez J, Rey J, Sandoval S, et al (2019) Geophysical prospecting using ERT and IP techniques to locate Galena veins. *Remote Sens* 11:

- <https://doi.org/10.3390/rs11242923>
- Martinho E, Dionísio A (2014) Main geophysical techniques used for non-destructive evaluation in cultural built heritage: A review. *J Geophys Eng* 11:1. <https://doi.org/10.1088/1742-2132/11/5/053001>
- Martorana R, Capizzi P, Pirra C (2023) Unconventional Arrays for 3D Electrical Resistivity and Induced Polarization Tomography to Detect Leachate Concentration in a Waste Landfill. *Appl Sci* 13:7203. <https://doi.org/10.3390/app13127203>
- Matias MJS, Habberjam GM (1986) The effect of structure and anisotropy on resistivity measurements. *Geophysics* 51:964–971. <https://doi.org/10.1190/1.1442154>
- Maurya PK, Balbarini N, Møller I, et al (2018) Subsurface imaging of water electrical conductivity, hydraulic permeability and lithology at contaminated sites by induced polarization. *Geophys J Int* 213:770–785. <https://doi.org/10.1093/gji/ggy018>
- Meju MA, Gallardo LA, Mohamed AK (2003) Evidence for correlation of electrical resistivity and seismic velocity in heterogeneous near-surface materials. *Geophys Res Lett* 30: <https://doi.org/10.1029/2002GL016048>
- Merritt AJ (2014) 4D Geophysical Monitoring of Hydrogeological Precursors to Landslide Activation. University of Leeds, UK.
- Merritt AJ, Chambers JE, Murphy W, et al (2014) 3D ground model development for an active landslide in Lias mudrocks using geophysical, remote sensing and geotechnical methods. *Landslides* 11:537–550. <https://doi.org/10.1007/s10346-013-0409-1>
- Moorkamp M, Roberts AW, Jegen M, et al (2013) Verification of velocity-resistivity relationships derived from structural joint inversion with borehole data. *Geophys Res Lett* 40:3596–3601. <https://doi.org/10.1002/grl.50696>
- Morgan LA (2012) Geophysical Characteristics of Volcanogenic Massive Sulfide Deposits Volcanogenic Massive Sulfide Occurrence Model. *US Geol Surv Sci Invest Rep* 2010–5070 –C 113–131
- Muñoz G, Bauer K, Moeck I, et al (2010) Exploring the Groß Schönebeck (Germany) geothermal site using a statistical joint interpretation of magnetotelluric and seismic tomography models. *Geothermics* 39:35–45. <https://doi.org/10.1016/j.geothermics.2009.12.004>
- Nero C, Aning AA, Danuor SK, Noye RM (2016) Delineation of graves using electrical resistivity tomography. *J Appl Geophys* 126:138–147. <https://doi.org/10.1016/j.jappgeo.2016.01.012>
- Obaje NG (2009) *Geology and Mineral Resources of Nigeria*. Springer Berlin Heidelberg, Berlin, Heidelberg
- Ogunyele AC, Obaje SO, Akingboye AS, et al (2020a) Petrography and geochemistry of Neoproterozoic charnockite–granite association and metasedimentary rocks around Okpella, southwestern Nigeria. *Arab J Geosci* 13: <https://doi.org/10.1007/s12517-020-05785-x>
- Ogunyele AC, Oluwajana OA, Ehinola IQ, et al (2020b) Petrochemistry and petrogenesis of the Precambrian Basement Complex rocks around Akungba-Akoko, southwestern Nigeria. *Mater Geoenvironment* 66:173–183. <https://doi.org/10.2478/rmzmag-2019-0036>
- Okpoli CC, Akingboye AS (2019) Application of high-resolution gravity data for litho-structural and depth characterisation around Igabi area, Northwestern Nigeria. *NRIAG J Astron Geophys* 8:231–241. <https://doi.org/10.1080/20909977.2019.1689629>
- Oladapo M, Mohammed M, Adeoye O, Adetola B (2004) Geoelectrical investigation of the Ondo State Housing Corporation Estate Ijapo Akure, southwestern Nigeria. *J Min Geol* 40:41–48. <https://doi.org/10.4314/jmg.v40i1.18807>
- Olayinka AI (1992) Geophysical siting of boreholes in crystalline basement areas of Africa. *J African Earth Sci* 14:197–207. [https://doi.org/10.1016/0899-5362\(92\)90097-V](https://doi.org/10.1016/0899-5362(92)90097-V)
- Ong WS (1993) The geology and engineering geology of Pulau Pinang. Geological Survey of Malaysia, Map Report
- Opfer R (2003) Imaging Seismic Data With High Resolution Gravity Data. In: 8th Simposio Bolivariano - Exploracion Petrolera en las Cuencas Subandinas. European Association of Geoscientists & Engineers, pp 33–48
- Optim Incorporation (2006) User's Manual for SeisOpt@2D Software. 71
- Orlando L (2013) Some considerations on electrical resistivity imaging for characterization of waterbed sediments. *J Appl Geophys* 95:77–89. <https://doi.org/10.1016/j.jappgeo.2013.05.005>
- Oware EK, Irving J, Hermans T (2019) Basis-constrained Bayesian Markov-chain Monte Carlo difference inversion for geoelectrical monitoring of hydrogeologic processes. *GEOPHYSICS* 84:A37–A42. <https://doi.org/10.1190/geo2018-0643.1>
- Palis E, Lebourg T, Vidal M, et al (2017) Multiyear time-lapse ERT to study short- and long-term landslide hydrological dynamics. *Landslides* 14:1333–1343. <https://doi.org/10.1007/s10346-016-0791-6>
- Passaro S (2010) Marine electrical resistivity tomography for shipwreck detection in very shallow water: a case study from Agropoli (Salerno, southern Italy). *J Archaeol Sci* 37:1989–1998. <https://doi.org/10.1016/j.jas.2010.03.004>
- Perri MT, Barone I, Cassiani G, et al (2020) Borehole effect causing artefacts in cross-borehole electrical resistivity tomography: A hydraulic fracturing case study. *Near Surf Geophys* 18:445–462. <https://doi.org/10.1002/nsg.12111>
- Quigley TP (2006) Ground proving seismic refraction tomography (SRT) in laterally variable karstic limestone terrain. The University of Florida
- Raji WO, Addamah MA, Suleiman M (2023) Subsurface characterization in an ancient graveyard with potential applications to forensic investigations. *Bull Eng Geol Environ* 82:38. <https://doi.org/10.1007/s10064-022-03054-7>
- Revil A, Vaudelet P, Su Z, Chen R (2022) Induced Polarization as a Tool to Assess Mineral Deposits: A Review. *Minerals* 12:571. <https://doi.org/10.3390/min12050571>
- Rey J, Martínez J, Hidalgo MC, et al (2020) Assessment of Tailings Ponds by a Combination of Electrical (ERT and IP) and Hydrochemical Techniques (Linares, Southern Spain). *Mine Water Environ* 40:298–307. <https://doi.org/https://doi.org/10.1007/s10230-020-00709-3>
- Ronczka M, Hellman K, Günther T, et al (2017) Electric resistivity and seismic refraction tomography: A challenging joint underwater survey at Äspö Hard Rock Laboratory. *Solid Earth* 8:671–682
- Ronczka M, Wisén R, Dahlin T (2018) Geophysical pre-investigation for a Stockholm tunnel project: Joint inversion and interpretation of geoelectric and seismic refraction data in an urban environment. *Near Surf Geophys* 16:258–268. <https://doi.org/10.3997/1873-0604.2018009>
- Rosa DR, Santos JMC, Souza RM, et al (2020) Comparing different approaches of time-lapse seismic inversion. *J Geophys Eng* 17:929–939. <https://doi.org/10.1093/jge/gxaa053>
- Rucker DF, Tsai CH, Carroll KC, et al (2021a) Bedrock architecture, soil texture, and hyporheic zone characterization combining electrical resistivity and induced polarization imaging. *J Appl Geophys* 188:104306. <https://doi.org/10.1016/j.jappgeo.2021.104306>
- Rucker DF, Walker WK, Greenwood J (2021b) Three-dimensional Time-domain Induced Polarization of a Desert Aridisol for Septic Design. *J Environ Eng Geophys* 26:153–164. <https://doi.org/10.32389/JEEG21-005>
- Rudman AJ, Whaley HF, Blakely RF, Biogs ME (1975) Transformation of resistivity to pseudovelocity logs. *Am Assoc Pet Geol Bull* 59:1151–1165
- Salleh AN, Muztaza NM, Sa'ad R, et al (2021) Application of geophysical methods to evaluate soil dynamic properties in Penang Island, Malaysia. *J Asian Earth Sci* 207:104659. <https://doi.org/10.1016/j.jseae.2020.104659>
- Schlundwein V, Bonnemant C, Reichert C, et al (2003) Three-dimensional seismic refraction tomography of the crustal structure at the ION site on the Ninetyeast Ridge, Indian Ocean. *Geophys J Int* 152:171–184. <https://doi.org/10.1046/j.1365-246X.2003.01838.x>
- Schlumberger C (1920) Study of underground electrical prospecting. In: *Electr. Prospect.* <https://archive.org/details/studyofundergrou00schlrch/page/n37/mode/2up>. Accessed 8 May 2023
- Sehoolle L, Manzi MSD, Zhang SE, Bourdeau JE (2020) An innovative seismic and statistical approach to understand 3D magmatic structures and ore deposits in the western Bushveld Complex, South Africa. *Ore Geol Rev* 126: <https://doi.org/10.1016/j.oregeorev.2020.103784>
- Seigel HO (1959) Mathematical formulation and type curves for induced polarization. *GEOPHYSICS* 24:547–565. <https://doi.org/10.1190/1.1438625>
- Sendrós A, Himi M, Lovera R, et al (2020) Electrical resistivity tomography monitoring of two managed aquifer recharge ponds in the alluvial aquifer of the Llobregat River (Barcelona, Spain). *Near Surf Geophys* 18:353–368. <https://doi.org/10.1002/nsg.12113>
- Sinaga KP, Yang M-S (2020) Unsupervised K-Means Clustering Algorithm. *IEEE Access* 8:80716–80727.

- <https://doi.org/10.1109/ACCESS.2020.2988796>
- Singh KP (2005) Nonlinear estimation of aquifer parameters from surficial measurements. *Hydrol Earth Syst Sci* 2:917–938. <https://doi.org/10.5194/hessd-2-917-2005>
- Slater LD, Binley AM, Daily W, Johnson R (2000) Cross-hole electrical imaging of a controlled saline tracer injection. *J Appl Geophys* 44:85–102. [https://doi.org/10.1016/S0926-9851\(00\)00002-1](https://doi.org/10.1016/S0926-9851(00)00002-1)
- Slater LD, Glaser DR (2003) Controls on induced polarization in sandy unconsolidated sediments and application to aquifer characterization. *Geophysics* 68:1542–1558. <https://doi.org/10.1190/1.1620628>
- Slater LD, Lesmes D (2002) IP interpretation in environmental investigations. *Geophysics* 67:77–88. <https://doi.org/10.1190/1.1451353>
- Slater LD, Ntarlagiannis D, Day-Lewis FD, et al (2010) Use of induced polarization to characterize the hydrogeologic framework of the zone of surfacewater/groundwater exchange at the Hanford 300 area, WA. In: *Proceedings of the Symposium on the Application of Geophysics to Engineering and Environmental Problems*, SAGEEP. J and N Group, Ltd., pp 955–960
- Snyder DD, MacInnes SC, Raymond MJ, Zonge KL (2002) Continuous Resistivity Profiling in Shallow Marine and Fresh Water Environments. In: *Symposium on the Application of Geophysics to Engineering and Environmental Problems 2002*. Environment and Engineering Geophysical Society, pp GSL4–GSL4
- Storz, Storz, Jacobs (2000) Electrical resistivity tomography to investigate geological structures of the earth's upper crust. *Geophys Prospect* 48:455–471. <https://doi.org/10.1046/j.1365-2478.2000.00196.x>
- Sujitapan C, Kendall JM, Chambers JE, Yordkayhun S (2024) Landslide assessment through integrated geoelectrical and seismic methods: A case study in Thungsong site, southern Thailand. *Heliyon* 10:e24660. <https://doi.org/10.1016/j.heliyon.2024.e24660>
- Szalai S, Baracza MK, Kárpi M, et al (2022) Improving ERT Imaging of Small-Size 2D Targets Using Different Strategies. *Pure Appl Geophys*. <https://doi.org/10.1007/s00024-022-03204-8>
- Szalai S, Szokoli K, Prácer E, et al (2020) An alternative way in electrical resistivity prospecting: The quasi-null arrays. *Geophys J Int* 220:1463–1480. <https://doi.org/10.1093/gji/ggz518>
- Tarantola A (1984) Inversion of seismic reflection data in the acoustic approximation. *GEOPHYSICS* 49:1259–1266. <https://doi.org/10.1190/1.1441754>
- Tejero-Andrade A, Cifuentes G, Chávez RE, et al (2015) L - and CORNER - arrays for 3D electric resistivity tomography: an alternative for geophysical surveys in urban zones. *Near Surf Geophys* 13:355–368. <https://doi.org/10.3997/1873-0604.2015015>
- Telford WM, Geldart LP, Sheriff RE (1990) *Applied Geophysics*, 2nd Edition
- Udosen NI, George NJ (2018) Characterization of electrical anisotropy in North Yorkshire, England using square arrays and electrical resistivity tomography. *Geomech Geophys Geo-Energy Geo-Resources* 4:215–233. <https://doi.org/10.1007/s40948-018-0087-5>
- Virieux J, Operto S (2009) An overview of full-waveform inversion in exploration geophysics. *GEOPHYSICS* 74:WCC1–WCC26. <https://doi.org/10.1190/1.3238367>
- Wang S, Kalscheuer T, Bastani M, et al (2018) Joint inversion of lake-floor electrical resistivity tomography and boat-towed radio-magnetotelluric data illustrated on synthetic data and an application from the Äspö Hard Rock Laboratory site, Sweden. *Geophys J Int* 213:511–533. <https://doi.org/10.1093/gji/ggx414>
- Weatherby BB, Faust LY (1935) Influence of Geological Factors on Longitudinal Seismic Velocities. *Am Assoc Pet Geol Bull* 19:1–8. <https://doi.org/10.1306/3D932CA4-16B1-11D7-8645000102C1865D>
- White DJ (1989) Two-Dimensional Seismic Refraction Tomography. *Geophys J Int* 97:223–245. <https://doi.org/10.1111/j.1365-246X.1989.tb00498.x>
- Wilkinson PB, Loke MH, Meldrum PI, et al (2012) Practical aspects of applied optimized survey design for electrical resistivity tomography. *Geophys J Int* 189:428–440. <https://doi.org/10.1111/j.1365-246X.2012.05372.x>
- Wilkinson PB, Meldrum PI, Chambers JE, et al (2006) Improved strategies for the automatic selection of optimized sets of electrical resistivity tomography measurement configurations. *Geophys J Int* 167:1119–1126. <https://doi.org/10.1111/j.1365-246X.2006.03196.x>
- Wilkinson PB, Uhlemann S, Chambers JE, et al (2014) Development and testing of displacement inversion to track electrode movements on 3-D electrical resistivity tomography monitoring grids. *Geophys J Int* 200:1566–1581. <https://doi.org/10.1093/gji/ggu483>
- Woakes M, Rahaman MA, Ajibade AC (1987) Some metallogenetic features of the Nigerian basement. *J African Earth Sci* 6:655–664. [https://doi.org/10.1016/0899-5362\(87\)90004-2](https://doi.org/10.1016/0899-5362(87)90004-2)
- Wong J (1995) Crosshole seismic tomography across a masonry dam. In: Nazarian S, Olson LD (eds) *Proceedings of the SPIE*, pp 58–66
- Xixi L, Zou C, Peng C, Wu C (2023) Uncertainty Quantification in Intelligent-Based Electrical Resistivity Tomography Image Reconstruction With Monte Carlo Dropout Strategy. *IEEE Trans Geosci Remote Sens* 61:1–16. <https://doi.org/10.1109/TGRS.2023.3262835>
- Yang F, Ma J (2019) Deep-learning inversion: a next generation seismic velocity-model building method
- Yang Q, Tan M, Zhang F, Bai Z (2021) Wireline Logs Constraint Borehole-to-Surface Resistivity Inversion Method and Water Injection Monitoring Analysis. *Pure Appl Geophys* 178:939–957. <https://doi.org/10.1007/s00024-021-02674-6>
- Yang Y, Wang Z, Chang T, et al (2020) Seismic Observation and Analysis Based on Three-Component Fiber Optic Seismometer. *IEEE Access* 8:1374–1382. <https://doi.org/10.1109/ACCESS.2019.2961963>
- Zakaria MT, Mohd Muztaza N, Zabidi H, et al (2022) Integrated analysis of geophysical approaches for slope failure characterisation. *Environ Earth Sci* 81:299. <https://doi.org/10.1007/s12665-022-10410-z>
- Zakaria MT, Muztaza NM, Zabidi H, et al (2021) 2-D Cross-Plot Model Analysis Using Integrated Geophysical Methods for Landslides Assessment. *Appl Sci* 11:11. <https://doi.org/https://doi.org/10.3390/app11020747>
- Zangrando AFJ (2018) Shell Middens and Coastal Archaeology in Southern South America. In: *Encyclopedia of Global Archaeology*. Springer International Publishing, pp 1–15
- Zeng Z, Kong L, Wang M, Sayem HM (2018) Assessment of engineering behaviour of an intensely weathered swelling mudstone under full range of seasonal variation and the relationships among measured parameters. *Can Geotech J* 55:1837–1849. <https://doi.org/10.1139/cgj-2017-0582>
- Zhang Y, Li YE, Ku T (2021) Soil/rock interface profiling using a new passive seismic survey: Autocorrelation seismic interferometry. *Tunn Undergr Sp Technol* 115:104045. <https://doi.org/10.1016/j.tust.2021.104045>
- Zhou B (2019) Electrical Resistivity Tomography: A Subsurface-Imaging Technique. In: *Applied Geophysics with Case Studies on Environmental, Exploration and Engineering Geophysics*. IntechOpen
- Zhou B, Bouzidi Y, Ullah S, Asim M (2020) A full-range gradient survey for 2D electrical resistivity tomography. *Near Surf Geophys* 18:609–626. <https://doi.org/10.1002/nsg.12125>
- Zhou B, Greenhalgh SA (2000) Cross-hole resistivity tomography using different electrode configurations. *Geophys Prospect* 48:887–912. <https://doi.org/10.1046/j.1365-2478.2000.00220.x>